



Department of Applied Physics and Science Education

# Simulating Positive Streamer Discharges in Air

*Branching and Model Validation*

Zhen Wang



# Simulating Positive Streamer Discharges in Air

*Branching and Model Validation*

PROEFSCHRIFT

ter verkrijging van de graad van doctor aan de Technische Universiteit  
Eindhoven, op gezag van de rector magnificus prof.dr. S.K. Lenaerts, voor  
een commissie aangewezen door het College voor Promoties, in het  
openbaar te verdedigen op donderdag 21 december 2023 om 13:30 uur

door

Zhen Wang

geboren te Shandong, China

Dit proefschrift is goedgekeurd door de promotoren en de samenstelling van de promotiecommissie is als volgt:

<b>Voorzitter</b>	prof.dr. C. Storm	
<b>Promotor</b>	prof.dr. U.M. Ebert	
	prof.dr. A. Sun	Xi'an Jiaotong University
<b>Copromotoren</b>	dr. H.J. Teunissen	Centrum Wiskunde en Informatica
<b>Leden</b>	prof.dr. O. Scholten	Rijksuniversiteit Groningen
	dr. S. Nijdam	
	prof.dr. X. Yang	Xi'an Jiaotong University
	prof.dr. G. Zhang	Xi'an Jiaotong University

*Het onderzoek of ontwerp dat in dit proefschrift wordt beschreven is uitgevoerd in overeenstemming met de TU/e Gedragscode Wetenschapsbeoefening.*



Centrum Wiskunde & Informatica



西安交通大学  
XI'AN JIAOTONG UNIVERSITY

The research was conducted under a double doctoral degree program between the Department of Applied Physics at Eindhoven University of Technology and the School of Electrical Engineering at Xi'an Jiaotong University. The work was carried out at Centrum Wiskunde & Informatica (CWI) in Amsterdam, and funded by NWO-I and the China Scholarship Council (CSC) (Grant No. 202006280465).

Cover Design: Yuying Zhang

Printing: Ipskamp Printing B.V.

A catalogue record is available from the Eindhoven University of Technology Library.



# Contents

<b>1</b>	<b>Introduction</b>	<b>1</b>
1.1	An overview of streamer discharges . . . . .	3
1.1.1	Introduction of streamer discharges . . . . .	3
1.1.2	Particle motion and collisions . . . . .	4
1.1.3	Streamer inception: from avalanche to streamer . . .	6
1.1.4	Streamer polarity and propagation . . . . .	7
1.1.5	Townsend scaling: similarity law between streamer discharges . . . . .	8
1.1.6	Streamer discharges in an external magnetic field . .	9
1.2	Streamer discharge modeling . . . . .	10
1.2.1	Particle model . . . . .	11
1.2.2	Fluid model . . . . .	12
1.2.3	Challenges in streamer modeling . . . . .	13
1.2.4	Framework . . . . .	14
1.2.5	Photoionization and its modeling . . . . .	15
1.2.6	Input data for streamer modeling . . . . .	18
1.3	Research topics and structure of the thesis . . . . .	20
<b>2</b>	<b>Particle and fluid model comparison</b>	<b>23</b>
2.1	Introduction . . . . .	25
2.2	Model description . . . . .	27
2.2.1	Particle (PIC-MCC) model . . . . .	28
2.2.2	Fluid model . . . . .	31
2.2.3	Computational domain and initial conditions . . . .	33
2.2.4	Photoionization . . . . .	35
2.2.5	Afivo AMR framework . . . . .	36
2.3	Results . . . . .	36

2.3.1	Axisymmetric and 3D results . . . . .	36
2.3.2	Fluid model transport and reaction data . . . . .	43
2.3.3	Mesh refinement and numerical convergence . . . . .	47
2.3.4	Stochastic fluctuations . . . . .	49
2.3.5	Results at different voltages . . . . .	51
2.4	Conclusions . . . . .	53
<b>3</b>	<b>2D Cartesian and 2D axisymmetric model comparison</b>	<b>57</b>
3.1	Introduction . . . . .	59
3.2	Model description . . . . .	60
3.2.1	Simulation conditions and computational domain . . . . .	61
3.2.2	Input data . . . . .	62
3.2.3	Computation of streamer radius . . . . .	64
3.3	Results . . . . .	64
3.3.1	Comparison under the same applied voltage . . . . .	64
3.3.2	Effect of electrode geometry on inception voltage . . . . .	65
3.3.3	comparison around streamer inception voltage . . . . .	65
3.3.4	Relation between streamer properties . . . . .	68
3.3.5	Discussion on streamer branching in 2D Cartesian model . . . . .	72
3.4	Conclusions . . . . .	75
<b>4</b>	<b>Quantitative modeling of branching streamer</b>	<b>77</b>
4.1	Introduction . . . . .	79
4.2	Photoionization and branching . . . . .	80
4.3	Set-up of experiments and simulations . . . . .	81
4.4	Results . . . . .	86
4.5	Conclusions . . . . .	89
<b>5</b>	<b>Positive streamers in a strong external magnetic field</b>	<b>91</b>
5.1	Introduction . . . . .	93
5.1.1	Computational domain and simulation conditions . . . . .	97
5.1.2	Effect of magnetic field on electron drift and ionization . . . . .	98
5.2	Results & Discussion . . . . .	101
5.2.1	3D simulations . . . . .	101
5.2.2	Branching in a perpendicular field . . . . .	104
5.2.3	Effect of magnetic field on streamer radius . . . . .	105



5.2.4	Bending in $-E \times B$ direction . . . . .	106
5.2.5	Comparison with experimental work . . . . .	107
5.3	Conclusions . . . . .	107
<b>6</b>	<b>Conclusions and outlook</b>	<b>109</b>
6.1	Summary of findings . . . . .	110
6.2	Outlook . . . . .	112
<b>A</b>	<b>Computational cost</b>	<b>115</b>
<b>B</b>	<b>Simulation set-up for branching streamers in air</b>	<b>119</b>
B.1	Photoionization and initial electron density . . . . .	121
B.2	Ionization density due to previous pulses . . . . .	122
B.3	Pulse rise time . . . . .	123
B.4	Time evolution . . . . .	124
B.5	Radii before and after branching . . . . .	125
	<b>Bibliography</b>	<b>127</b>
	<b>Acknowledgement</b>	<b>145</b>
	<b>Curriculum Vitae</b>	<b>147</b>



# Chapter 1

## Introduction

In this chapter, we briefly introduce streamer phenomena, along with computational models of streamer discharges. Research topics and the structure of this thesis are presented in the end.



## 1.1 An overview of streamer discharges

### 1.1.1 Introduction of streamer discharges

Streamer discharges are elongated conducting channels that typically grow with a velocity between  $10^5$  and  $10^7$  m/s [1, 2, 3, 4, 5, 6, 7, 8]. They appear when an insulating medium is locally exposed to a field above its breakdown value, and they can form complex tree-like structures [9]. Streamer discharges can be observed in both natural and laboratory environments: sprite discharges above active thunderstorms are large-scale streamer discharges in our atmosphere [10, 11, 12], and streamers are used in for example corona reactors or plasma jets for technical purposes [13, 14]. Figure 1.1 shows two examples of positive streamer discharges. Furthermore, streamers are the precursors to sparks and lightning leaders [15].

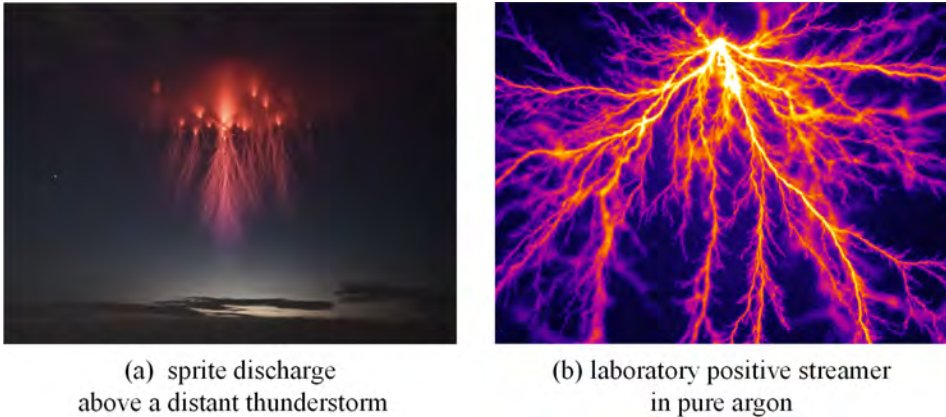


Figure 1.1: Illustration of streamers in natural and laboratory environments. (a) Red sprites above a thunderstorm. Figure taken from [16]. (b) Positive streamer discharge in pure argon at room temperature and atmospheric pressure (in false colors). Figure taken from [3].

The key mechanism in a streamer is the motion of electrons in the local electric field and the collisions between electrons and neutral gas molecules. Electric field enhancement around streamer tips causes streamers to rapidly grow through electron impact ionization. Due to this field enhancement, streamers can propagate into regions where the background field is initially

below the breakdown threshold. Streamers frequently split into separate channels, which is referred to as streamer branching. Streamers in air usually follow background electric field lines, although deviations can occur due to processes such as branching.

In ambient air, electron densities in streamer channels can reach magnitudes of  $10^{21} \text{ m}^{-3}$ . Electrons at tips of positive streamers can have energies of up to tens of eVs, and those electrons can trigger chemical reactions with a high activation energy. In air, OH, O and N radicals as well as excited species and ions like  $\text{N}_2^+$ ,  $\text{O}_2^+$ ,  $\text{O}_2^-$ ,  $\text{O}^-$ ,  $\text{O}^+$ ,  $\text{N}_4^+$  and  $\text{O}_4^+$  can be generated through streamer discharges, and these species can trigger further chains of reactions with the surrounding gas, or with solid and liquid surfaces. Based to these properties, diverse industrial applications of streamer plasma have been developed, such as gas purification or ozone production [17], the treatment of liquids [18], industrial surface treatment [19], plasma medicine [20], and plasma assisted combustion [21].

### 1.1.2 Particle motion and collisions

When that an insulating gas, such as air, is exposed to a high electric field, free electrons gain kinetic energy and collide with other particles. In this thesis we study plasmas with ionization degrees below  $10^{-4}$ , so these electrons predominantly collide with neutral particles, namely gas molecules. Ions also gain energy from the electric field, but at a much slower rate due to their larger mass. They lose more energy than electrons in elastic collisions with neutrals, because the colliding masses are similar. For this reason, we do not consider the motion of ions in this thesis.

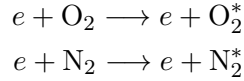
In air, the most important electron-neutral collisions are:

- Elastic collisions,



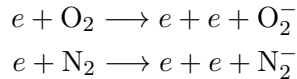
in which the internal energies of the colliding particles do not change, while an amount of energy proportional to  $m/M$  can be exchanged, where  $m$  is the electron mass and  $M$  the mass of an oxygen/nitrogen molecule.

- Excitations,



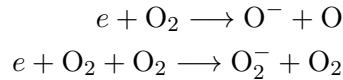
in which some of the electron's kinetic energy is transferred to the internal energy of the molecule.

- Electron impact ionization,



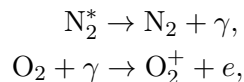
in which more free electrons are generated. This type of collisions only happens if the electron carries enough energy to liberate another electron from the neutral. This binding energy depends on the molecule type, and it is 12.07 eV for  $\text{O}_2$  [22] and 15.58 eV for  $\text{N}_2$  [23].

- Attachment



in which the electron sticks to the neutral to form a negative ion. The first reaction is dissociative electron attachment and the second reaction is three-body attachment. In ambient air and a low background field, three-body attachment occurs more frequently [24, 25], since dissociative attachment has a threshold energy for electrons of 4.8 eV [22].

- Photoionization



in which an excited  $\text{N}_2$  molecule decays via the emission of a UV-photon, the photon can then ionize an  $\text{O}_2$  molecule. The required wavelength of the photons is between 98 and 102.5 nm. Photoionization is further discussed in section 1.2.5.

Another relevant process is the recombination of charged particles [26]. However, on the short time scales and low degrees of ionization considered in this thesis, this process does not play an important role.

### 1.1.3 Streamer inception: from avalanche to streamer

When a gas is exposed to a high background electric field, an initial free electron can initiate an electron avalanche as illustrated in figure 1.2. Such a free electron could be present due to e.g. cosmic radiation or background ionization. The electron is accelerated by the electric field, until it collides with a neutral after a certain distance. If the electron energy suffices, a new free electron can be liberated from the neutral. Subsequently, both electrons continue to move and generate additional free electrons. In such way, the number of electrons increases exponentially, which can be described as

$$N_e = e^{\bar{\alpha}d}, \quad (1.1)$$

where  $N_e$  is the number of electrons in the avalanche which starts from a single electron,  $d$  is the distance traveled, and  $\bar{\alpha} = \alpha - \eta$  is the effective Townsend ionization coefficient. Here  $\alpha$  denotes how many ionizations a single electron produces per unit length. Since an electron can only attach once,  $\eta dx$  could be interpreted as the probability that attachment occurs over a small length  $dx$  [27].

An avalanche can only form when  $\bar{\alpha} > 0$ , which indicates that ionization happens more frequently than attachment, so that the number of free electrons increases. The critical or breakdown field  $E_c$  is defined as the minimum value when  $\bar{\alpha} > 0$ . For atmospheric air the breakdown field is about 30 kV/cm.

Avalanches do not grow indefinitely, as space charge effects that modify the electric field cannot be ignored when the avalanche grows to a certain size. The well-known Raether-Meek criterion is an empirical rule in ambient air to define when space charge effects become significant, namely when  $\bar{\alpha}d \approx 18$  to 21, or when  $N_e \approx 10^8$  to  $10^9$ . At this point, avalanches become streamers.



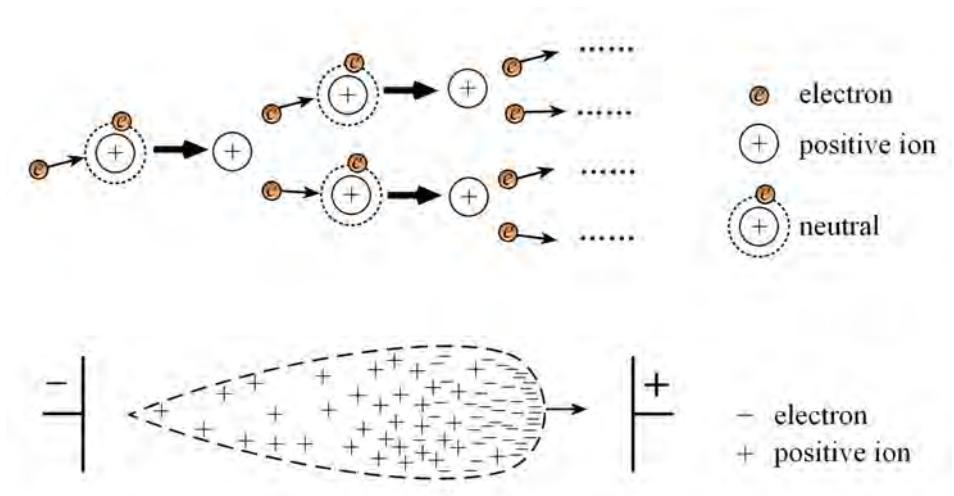


Figure 1.2: Formation of an electron avalanche. The top panel shows the increase of free electrons, and the bottom panel shows an example of an avalanche.

### 1.1.4 Streamer polarity and propagation

Streamers can be classified as positive or negative, based on the polarity of their space charge layers. A negative streamer carries a negative charge surplus at its head, and it propagates in the direction of electron drift. Conversely, a positive streamer has a surplus of positive charge, and it propagates in the opposite direction of electron drift.

In air, positive streamers initiate more easily than negative streamers, and positive streamers also propagate faster and further under the same initial conditions. Their charge layers are formed by an excess of positive ions, and these ions hardly move. Therefore electric field enhancement is better maintained ahead of positive streamers.

A positive streamer grows due to the ionization of approaching electron avalanches. Free electrons are therefore required in the region ahead of the streamer tip. In atmospheric air, the source of free electrons is mainly the photoionization of oxygen molecules [28], which is discussed in more detail in section 1.2.5. For negative streamers, the electrons in the space charge layer drift outward, so they do not require a non-local source of free

electrons to propagate.

### 1.1.5 Townsend scaling: similarity law between streamer discharges

As mentioned above, electrons travel and collide mostly with neutrals in a gas environment. The electron mean free path  $\ell_{\text{MFP}}$  is therefore defined as the average distance the electron travels between collisions, it can be expressed as

$$\ell_{\text{MFP}} = 1/N\sigma, \quad (1.2)$$

where  $N$  is the gas number density and  $\sigma$  is the effective cross-section for collisions. When an electron travels a distance of  $\ell_{\text{MFP}}$  parallel to the electric field, it gains an energy of  $eE \cdot \ell_{\text{MFP}}$ , where  $e$  is the elementary charge. When  $E \cdot \ell_{\text{MFP}}$  stays the same, electrons under different condition can therefore gain the same energy when traveling a mean free path. Since streamer dynamics are dominated by electron acceleration in electric fields together with electron-molecule collisions, the same dynamics can then be observed. Because  $\ell_{\text{MFP}}$  is proportional to  $1/N$ , this motivates the introductions of the reduced electric field  $E/N$  and its unit Townsend (Td) as

$$1\text{Td} = 10^{-21}\text{V} \cdot \text{m}^2. \quad (1.3)$$

For a given  $E/N$ , other properties of streamer discharges scale as [29]:

- $L \propto 1/N$ , as  $\ell_{\text{MFP}}$  set the scale for other length parameters  $L$ ,
- $\rho \propto N^2$ , where  $\rho$  stands for charge density, electron density and ion density.
- $t \propto 1/N$ , where  $t$  stands for typical time scales, such as the time between ionizing collisions.

Since characteristic electron velocities are determined by the balance of the kinetic electron energy and the ionization energy of the molecule, they do not vary with  $N$ .

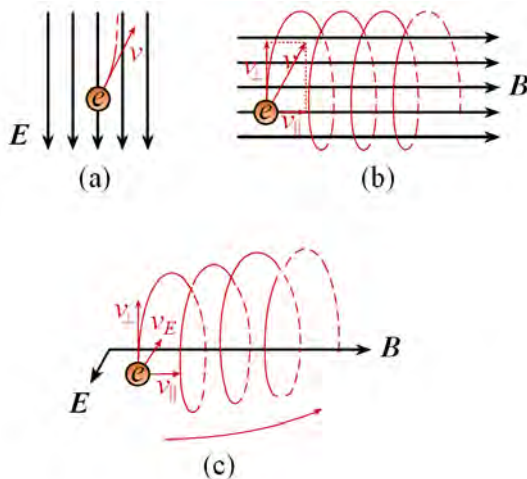


Figure 1.3: Illustrations for electron motion in (a) an electric field  $\mathbf{E}$ , (b) a magnetic field  $\mathbf{B}$  and (c) both an electric field  $\mathbf{E}$  and a magnetic field  $\mathbf{B}$ , aligned perpendicularly. Here  $v$  denotes the electron velocity,  $v_{\parallel}$  is the drift velocity in the direction of  $\mathbf{B}$ ,  $v_{\perp}$  is the velocity of electron cyclotron motion.  $v_E$  is the electron velocity in the direction of  $\mathbf{E}$ .

### 1.1.6 Streamer discharges in an external magnetic field

In this thesis, streamer discharges in external magnetic fields are also studied. An electron  $e$  moving with a velocity  $\mathbf{v}$  in an electric field  $\mathbf{E}$  and a magnetic field  $\mathbf{B}$  experiences a Lorentz force of

$$\mathbf{F} = e(\mathbf{E} + \mathbf{v} \times \mathbf{B}), \quad (1.4)$$

so its motion depends on both  $\mathbf{E}$  and  $\mathbf{B}$ . Figure 1.3 shows trajectories of a single electron with velocity  $\mathbf{v}$  in different kinds of fields, with collisions being ignored. In a pure electric field, the electron experiences an acceleration of  $\mathbf{a} = -e\mathbf{E}/m$ , where  $e$  is the elementary charge and  $m$  is the electron mass. In a pure magnetic field, electron motion can be separated in two components: a drift velocity  $v_{\parallel}$  parallel to  $\mathbf{B}$  and a gyration perpendicular  $\mathbf{B}$  with a cyclotron frequency  $\omega_{ce} = eB/m$  and a radius  $r_c = v_{\perp}/\omega_{ce}$ , where  $v_{\perp}$  is the magnitude of the electron velocity perpendicular to  $\mathbf{B}$ . When a

electron travels in a field of both  $\mathbf{E}$  and  $\mathbf{B}$ , its motion can be separated in three components:

- Acceleration by the electric field component parallel to  $\mathbf{B}$ .
- Drift in the  $\mathbf{E} \times \mathbf{B}$  direction, with a velocity  $v_{\times} = (\mathbf{E} \times \mathbf{B})/B^2$ .
- Cyclotron motion as discussed above, but the center of gyration and the radius vary due to the effect of the electric field.

In figure 1.3(c), we present a case where  $\mathbf{E}$  is perpendicular to  $\mathbf{B}$ .

For streamer discharge modeling, the electron collisions need to be further added to the electron motion. In this thesis, we used a 3D particle model to study the propagation of positive streamers in strong external magnetic fields of up to 40 T in ambient air. An advantage of using a particle model is that magnetic fields can relatively easily be included in the particle mover, see chapter 5. To include a magnetic field in a fluid model is also complicated, since both the computation of transport data and the integration of such data into the model are non-trivial [30, 31].

There are a few studies of streamers in external magnetic fields, using both experimental methods [32, 33, 34] and simulations [35, 36]. In experiments, obtaining a strong enough magnetic field in a sufficiently large volume is quite challenging, and interpreting the 3D structures of streamer morphologies from 2D planar images is difficult.

## 1.2 Streamer discharge modeling

Numerical simulations can be a powerful tool to study the physics of streamer discharges. In simulations, the electric field and all species densities are known, both in time and in space. Furthermore, physical mechanisms can be turned off or artificially increased, the discharge conditions can easily be modified, and simulations can be performed in simplified geometries. In this thesis, two commonly-used streamer discharge models are used and compared in detail, namely fluid models and particle models, which are introduced below.

### 1.2.1 Particle model

From a microscopic perspective, the physics of a streamer discharge is determined by the dynamics of particles: electrons, ions, neutral gas molecules (or atoms) and photons. The electrons and ions interact electrostatically through the collectively generated electric field. As mentioned in section 1.1.2, the collisions between electrons and gas neutrals are the dominant collisions in streamer discharges, and the motion of ions and neutrals is ignored in this thesis. Based on this understanding, streamer discharges can be simulated with particle-in-cell (PIC) codes coupled with a Monte Carlo collision (MCC) scheme. In a PIC code for streamer discharges, electrons are therefore described as particles, while ions are tracked as densities, and neutral gas molecules are included as a background that electrons stochastically collide with. An example of particle-in-cell simulation of discharge inception is shown in figure 1.4.

The stochastic collisions between electrons and neutral species can be divided in four major categories: elastic, excitation, electron-impact ionization and electron attachment [38]. Collision probabilities depend on the energy of electrons. These probability data, known as cross-sections, serve as input data in the particle model and are discussed further in section 1.2.6. The collisions between electrons and neutrals are handled with the null-collision method, which is a Monte Carlo procedure in which random numbers are used to determine the collision time. It is assumed that electrons scatter isotropically after a collision.

In particle models, the positions and velocities of electrons evolve throughout the simulation, and the electric field is updated every time step after the particles have moved. To compute the electric field, electron and ion densities are first mapped to a charge density  $\rho$  on a numerical grid. The electric potential  $\phi$  can then be computed by solving Poisson's equation

$$\nabla \cdot (\varepsilon \nabla \phi) = -\rho \quad (1.5)$$

where  $\varepsilon$  is the dielectric permittivity. Afterwards, the electric field can be computed as  $\mathbf{E} = -\nabla \phi$ .

In a typical discharge, the number of free electrons is so large that they cannot all be simulated individually. Instead, so-called *super-particles* are employed that represent multiple physical electrons, see section 2.2.1.

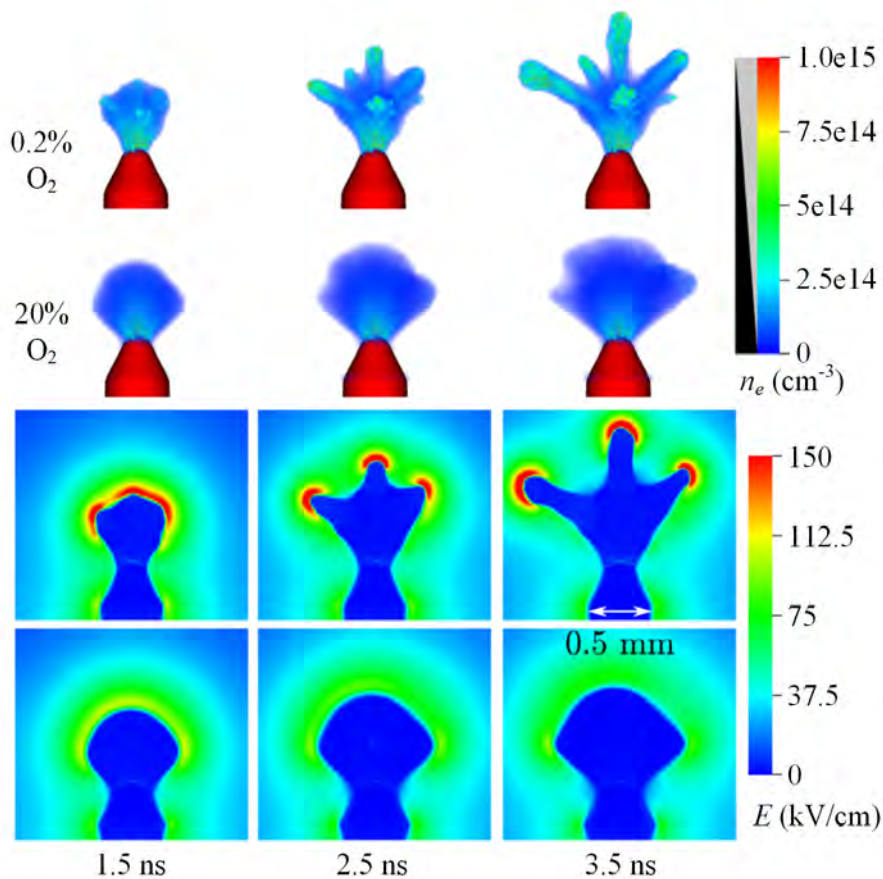


Figure 1.4: Example of particle-in-cell simulation where the discharge inception around a needle electrode is presented. The figure is adapted from [37].

## 1.2.2 Fluid model

Fluid models in general can be derived from the Boltzmann equation. They employ a continuum description of a discharge, which means that they describe the evolution of one or more densities in time [39]. A classic drift-diffusion-reaction fluid model with the local field approximation is used in

this thesis, as implemented in [40]. The electron density  $n_e$  evolves in time as

$$\partial_t n_e = \nabla \cdot (n_e \mu_e \mathbf{E} + D_e \nabla n_e) + S_R + S_{ph} \quad (1.6)$$

where  $\mu_e$  and  $D_e$  indicate the electron mobility and the diffusion coefficient,  $S_{ph}$  is the non-local photoionization source term and  $S_R$  is a source term due to electron impact ionization  $\alpha$  and attachment  $\eta$

$$S_R = (\alpha - \eta) \mu_e E n_e, \quad (1.7)$$

where  $E = |\mathbf{E}|$ . Additional terms can be included in  $S_R$  to account for e.g. electron detachment and recombination. Since ion motion is not taken into account in this thesis, ion densities evolve in time as

$$\partial_t n_j = S_j, \quad (1.8)$$

where  $S_j$  corresponds to the production and loss of the ion species due to for example ionization, attachment or ion conversion reactions.

Transport coefficients ( $\mu_e$  and  $D_e$ ) and reaction rates are often determined using the local field approximation, see section 1.2.6. An example of a simulation of a positive single streamer discharge in artificial air using the classic fluid model is shown in figure 1.5.

### 1.2.3 Challenges in streamer modeling

Streamer discharges are multiscale phenomena, both in space and in time, as illustrated in figure 1.5 and figure 1.4. Simulating their non-linear evolution is therefore computationally challenging. In atmospheric air, the smallest time scales that have to be resolved are on the order of  $10^{-13}$  s to  $10^{-11}$  s, based on following requirements:

- The maximal collision rate of electrons is around  $10^{13}$  Hz, which is relevant for particle simulations.
- Electrons should move less than one numerical grid spacing  $\Delta x$  per time step  $\Delta t$ . For typical values of  $\Delta x \sim \mu\text{m}$  and electron velocities  $v \sim 10^6$  m/s, this results in a time step  $\Delta t \sim 10^{-12}$  s.
- The time scale for electric screening (the Maxwell time) can be on the order of  $10^{-12}$  s or smaller. This time is defined as  $\tau_{\text{Maxwell}} = \varepsilon_0 / \sigma$ , where  $\varepsilon_0$  is the dielectric permittivity and  $\sigma$  the plasma conductivity.

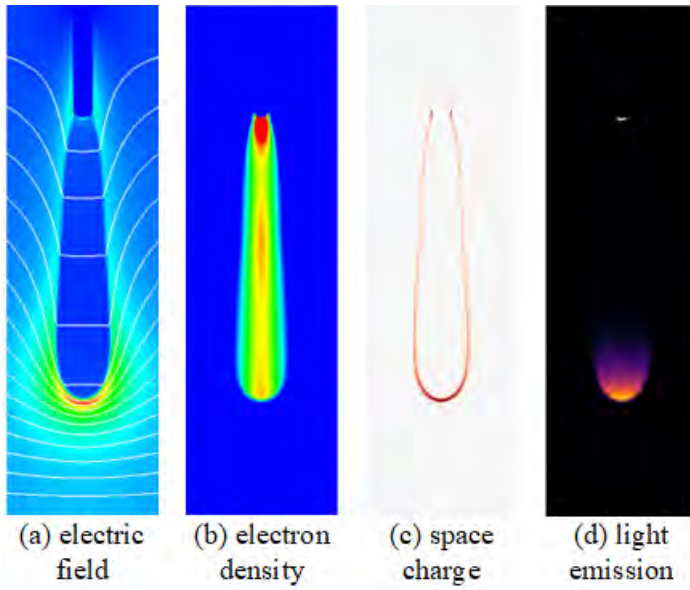


Figure 1.5: Simulation example showing a cross section of a single positive streamer propagating downwards.

Furthermore, simulations need to be performed with a high spatial resolution. In atmospheric air, space charge layers can have a thickness on the order of  $10\ \mu\text{m}$  or less. Furthermore, there are steep density gradients with characteristic widths  $n/\partial_x n \sim 1/\alpha$ , which can be on the order of several  $\mu\text{m}$ . To properly resolve these length scales as well as the strong electric field enhancement resulting from the charge layers, a grid spacing of a few  $\mu\text{m}$  is required.

Since a typical streamer discharge in atmospheric air develops on time scales of hundreds of nanoseconds and on spatial scales of centimeters or more, it is usually not feasible to simulate streamer discharges in 3D on a uniform grid.

### 1.2.4 Framework

The use of efficient computational methods is crucial for streamer simulations. Of particular importance is the type of numerical grid, which signif-

---



icantly impacts the overall performance. In fluid simulations, all quantities are defined on numerical grids, and in particle simulations, the grid is used to keep track of particle densities and to compute electric fields.

Due to the multi-scale nature of streamers, it is possible to use different resolutions in different parts of a computational domain. For example, near space charge layers, where the density of electrons changes rapidly and the electric field gradient is sharp, the mesh spacing is usually required to be a few micrometers, whereas the mesh spacing inside the streamer channel or far from it can be much larger. For the simulations in this thesis, we therefore make use of adaptive mesh refinement in both the fluid model and the particle model. The refinement is of the quadtree/octree type, provided by the Afivo framework [41].

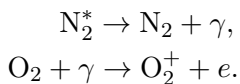
The refinement criterion depends on the local electric field:

$$\Delta x < c_0/\alpha(E), \quad (1.9)$$

where  $\alpha(E)$  is the effective ionization coefficient which depends on the local electric field. The reason for using this criterion is that  $1/\alpha$  is a typical length scale for ionization, so that the space charge layers of a discharge will have a width of a few times  $1/\alpha$ . The factor  $c_0$  decides the degree of refinement. In this thesis, we typically use  $c_0 = 1$ .

## 1.2.5 Photoionization and its modeling

Photoionization is defined as the process when neutrals are ionized by UV photons emitted from excited atoms or molecules. For streamer discharges in air, photo-ionization usually serves as a significant source of non-local free electrons, which is particularly important for positive streamers, as they advance against the electron drift velocity [42, 28]. Photoionization in air occurs in the following process: First, an energetic electron excites a nitrogen molecule to one of the  $b^1\Pi$ ,  $b'^1\Sigma_u^+$ ,  $c^1\Pi_u$  and  $c'^1\Sigma_u^+$  states. The excited nitrogen molecule emits a UV photon, of which the wavelength is in the range in 98-102.5 nm. Finally, oxygen molecules can be ionized at some distance by absorbing the emitted photons:



The distance which the emitted photo  $\gamma$  travels is defined as the absorption distance, which depends on the gas mixture and density.

Zheleznyak's model is the typical model used to describe photoionization in air. In this model, the mean absorption distance of emitted photons is about 0.45 mm for air at 1 bar and room temperature, as described by the absorption function  $f(r)$

$$f(r) = \frac{\exp(-\chi_{\min} p_{\text{O}_2} r) - \exp(-\chi_{\max} p_{\text{O}_2} r)}{r \ln(\chi_{\max}/\chi_{\min})}, \quad (1.10)$$

where  $\chi_{\max} \approx 1.5 \times 10^2$  /(mm bar),  $\chi_{\min} \approx 2.6$  /(mm bar), and  $p_{\text{O}_2}$  is the partial pressure of oxygen. Assuming that ionizing photons do not scatter and that their direction is isotropically distributed, the source term of photoionization  $S_{ph}$  in equation (1.6) is then computed as

$$S_{ph}(\mathbf{r}) = \int \frac{I(r') f(|\mathbf{r} - \mathbf{r}'|)}{4\pi |\mathbf{r} - \mathbf{r}'|^2} d^3r'. \quad (1.11)$$

Here  $I(\mathbf{r})$  is the source of ionizing photons, which is proportional to the electron impact ionization source term  $S_i$ :

$$I(\mathbf{r}) = \frac{p_q}{p + p_q} \xi S_i, \quad (1.12)$$

where  $p$  is the gas pressure,  $p_q = 40$  mbar is a quenching pressure and  $\xi$  is a proportionality factor, which depends on the local electric field. For simplicity, we fix it at  $\xi = 0.075$  in our simulations.

Zheleznyak's photoionization model can be implemented as a continuum method or as a Monte Carlo procedure. Both approaches are briefly introduced below. We typically use a continuum method in a fluid model, and a Monte Carlo approach in a particle model.

### **Continuum (Helmholtz) approach**

With a continuum method, the photo-ionization rate (ionizations per unit volume per unit time) is computed from the photon production rate (photons produced per unit volume per unit time). Directly evaluating the integral in equation (1.11) is computationally very costly, which is why the

so-called Helmholtz approximation [43, 44] is typically used. The idea is to approximate the absorption function as

$$f(r) \approx r \sum_{i=1}^N c_i e^{-\lambda_i r} \quad (1.13)$$

where  $c_i$  and  $\lambda_i$  are fitted coefficients. Equation (1.11) then transforms into  $N$  Helmholtz equations that can be solved more efficiently using fast elliptic solvers. We use Bourdon's three-term expansion, as described in [43] and appendix A of [45].

### Discrete (Monte-Carlo) approach

With a Monte Carlo approach photoionization is modeled as a stochastic process with discrete photons [46]. The main computational steps are summarized below, for further details see [46] and Chapter 11 of [27].

In a particle model, there is a certain probability of generating an ionizing photon after an electron-impact ionization, as described by equation (1.12). For each ionizing photon, the absorption length is then sampled from equation (1.10), and a direction is sampled isotropically. An electron-ion pair is then generated at the location of absorption.

In a fluid model, the number of emitted photons in each grid cell is sampled from a Poisson distribution with the mean given by  $I(\mathbf{r})\Delta t\Delta V$ , where  $\Delta t$  is the time step and  $\Delta V$  is the volume of the cell. The photons are then absorbed on a numerical grid, thereby defining the photoionization source term  $S_{ph}$  in equation (1.6).

When using discrete physical photons in a fluid model, the level of noise is still somewhat underestimated, since we use a fluid approximation for electrons and ions. This means that the electrons generated in photoionization events do not behave as discrete particles but as transported 'patches' with augmented electron density, with the size of the patch depending on the grid resolution.

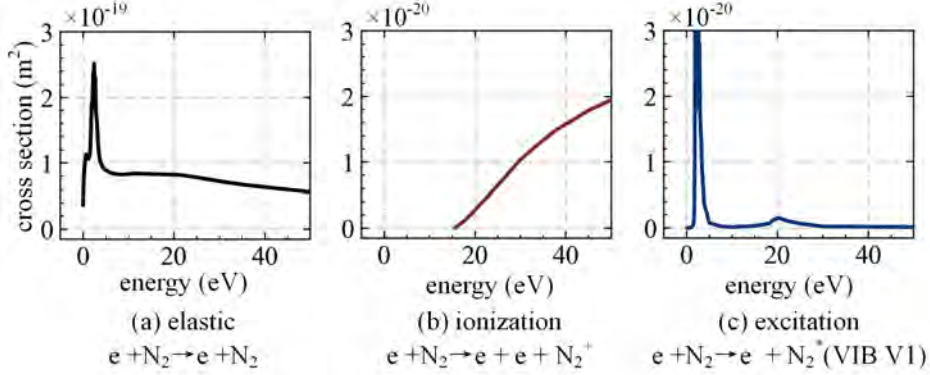


Figure 1.6: Illustration of elastic, ionization and excitation cross sections for  $\text{N}_2$ . The figure was generated using Biagi' database [47], obtained from [lxcat.net](http://lxcat.net). The database contains more excitation cross sections than the one shown here.

## 1.2.6 Input data for streamer modeling

### Cross sections

As illustrated in figure 1.2, electrons are accelerated by the electric field, and collide with a neutral under a certain probability. The probability of a collision  $i$  per unit time is given by the collision rate  $\mu_i$ , which is defined as

$$\mu_i = Nv\sigma_i, \quad (1.14)$$

where  $N$  is the number density of the neutral species,  $v$  is the electron velocity and  $\sigma_i$  is the energy-dependent cross section for the collision  $i$ . Cross sections are therefore required in particle simulations as input data, and they are often obtained from the online database [lxcat.net](http://lxcat.net). We present an illustration of cross section data for  $\text{N}_2$  in figure 1.6.

### Transport and reaction coefficients

In equations (1.6)–(1.8), the electron mobility  $\mu_e$ , the diffusion coefficient  $D_e$  and the coefficients  $\alpha$  and  $\eta$  are required to update electron densities and ion densities during fluid simulations. In a fluid model with the local

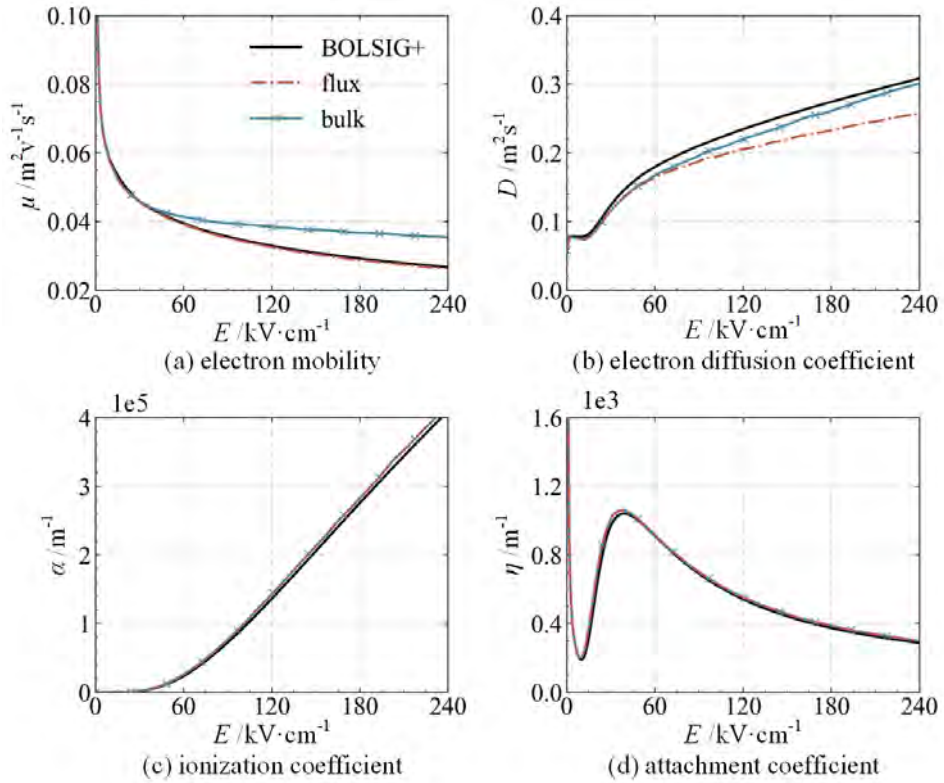


Figure 1.7: Illustration of electron transport data. (a) electron mobility, (b) electron diffusion coefficient, (c) ionization coefficient and (d) attachment coefficient. The coefficients were computed for 80%  $\text{N}_2$  and 20%  $\text{O}_2$  at 1 bar and 300 K, using Phelps’s cross sections. The data labeled “bulk” and “flux” was computed with a Monte Carlo swarm code, and “BOLSIG+” stands for the data computed with BOLSIG+ using the temporal growth option.

field approximation, these coefficients are tabulated versus the electric field strength. Such tables with reaction and transport data can be computed from electron-neutral cross sections using two approaches, briefly described below.

The first is BOLSIG+, which is a widely used Boltzmann solver [48, 49].

BOLSIG+ uses a two-term expansion, i.e, a first order expansion about an isotropic velocity distribution, which can be sufficient depending on the gas and the required accuracy [50]. However, when the electron velocity distribution is strongly anisotropic, for example in high electric fields, the use of the two term approximation can introduce errors [51]. Furthermore, it is possible to use either a spatial or temporal growth model in a Boltzman solver, which lead to different transport coefficients [48].

The other method is a Monte Carlo swarm code [gitlab.com/MD-CWI-NL/particle\\_swarm](https://gitlab.com/MD-CWI-NL/particle_swarm), similar to e.g. [52, 53]. The basic idea of this approach is to trace electrons in a uniform field, considering non-conservative collisions such as ionization and attachment. From there the transport and reactions coefficients can be obtained.

With the Monte Carlo method, an option can be used to decide whether to get *flux* or *bulk* coefficients [54, 55]. Flux data describe the average properties of individual electrons, whereas bulk data describe average properties of a group of electrons. For example, the bulk drift velocity then describes the average velocity of the center of mass of this group, whereas the flux drift velocity describes the average velocity of individual electrons. These two definitions differ when the probability of non-conservative collisions is not uniform in space, which causes motion of the center of mass. Figure 1.7 shows examples of transport data computed with these methods and both the flux and the bulk coefficients from the swarm code are presented.

### 1.3 Research topics and structure of the thesis

In this thesis, we study positive streamer discharges in air using simulations, with a focus on streamer dynamics and its branching phenomenon. Positive streamer discharges in strong external magnetic fields are discussed at the end. All simulations are performed at 300 K and 1 bar. In more detail, the thesis is structured as follows.

In chapter 2, we initially compare the fluid model and the particle model under the same AMR framework, and streamer properties including the channel conductivity, the maximal electric field, the streamer velocity, the streamer radii are discussed in detail. The influence of different transport data on fluid simulations is further studied, considering computational methods and bulk/flux types. We also look at the source of stochastic fluc-

tuations in the axisymmetric simulations, followed by the discussion on the model agreement under higher voltages.

In chapter 3, we compare 2D Cartesian and axisymmetric simulations of positive streamers in air, using a drift-diffusion-reaction fluid model with the local field approximation. Such 2D Cartesian simulations are sometimes used when full 3D simulations are computationally too expensive. We compare inception voltages and streamer properties, such as radius, velocity and maximal electric field, as well as the branching behavior of streamers in the two types of models.

In chapter 4, stochastic photoionization is employed in the fluid model to simulate positive streamer branching in atmospheric air. We perform a quantitative comparison between simulation results and the designated experiment results, considering the branching probability, the streamer morphology, and the streamer gap-bridging time. A validation of Zheleznyak's photoionization model is further presented by varying the photoionization coefficient  $\xi$ .

In chapter 5, we study how a strong external magnetic field of up to 40 T affects the propagation of positive streamers in air, and the cases when the magnetic field is perpendicular or parallel to the background electric field are investigated. The electron transport data in electric and magnetic fields crossed at arbitrary angle are calculated to explain the results.

Chapter 6 contains a summary of our key results, along with insights on the future possibilities to advance our comprehension of streamer discharges.





## Chapter 2

# A comparison of particle and fluid models for positive streamer discharges in air

Both fluid and particle models are commonly used to simulate streamer discharges. In this chapter, we quantitatively study the agreement between these approaches for axisymmetric and 3D simulations of positive streamers in air. We use a drift-diffusion-reaction fluid model with the local field approximation and a PIC-MCC (particle-in-cell, Monte Carlo collision) particle model. The simulations are performed at 300 K and 1 bar in a 10 mm plate-plate gap with a 2 mm needle electrode. Applied voltages between 11.7 and 15.6 kV are used, which correspond to background fields of about 15 to 20 kV/cm. Streamer properties like maximal electric field, head position and velocity are compared as a function of time or space.

Our results show good agreement between the particle and fluid simulations, in contrast to some earlier comparisons that were carried out in 1D or for negative streamers. To quantify discrepancies between the models, we mainly look at streamer velocities as a function of streamer length. For the test cases considered here, the mean deviation in streamer velocity between the particle and fluid simulations is less than 4%. We study the effect of different types of transport data for the fluid model, and find that flux coefficients lead to good agreement whereas bulk coefficients do not. Furthermore, we find that with a two-term Boltzmann solver, data should be computed using a temporal growth model for the best agree-

ment. The numerical convergence of the particle and fluid models is also studied. In fluid simulations the streamer velocity increases somewhat using finer grids, whereas the particle simulations are less sensitive to the grid. Photoionization is the dominant source of stochastic fluctuations in our simulations. When the same stochastic photoionization model is used, particle and fluid simulations exhibit similar fluctuations.

This chapter is published as:

Z. Wang, A. Sun, and J. Teunissen. A comparison of particle and fluid models for positive streamer discharges in air. *Plasma Sources Science and Technology*, 31(1):015012, 2022.

## 2.1 Introduction

Streamer discharges are elongated conducting channels that typically appear when an insulating medium is locally exposed to a field above its breakdown value [9]. Electric field enhancement around their tips causes streamers to rapidly grow through electron impact ionization. Due to this field enhancement, they can propagate into regions in which the background field was initially below breakdown. Streamers occur in nature as sprites [29, 57] and they are used in diverse applications such as the production of radicals [58], pollution control [17], the treatment of liquids [18], plasma medicine [20], and plasma combustion [21].

Over the last decades, numerical simulations have become a powerful tool to study streamer physics and to explain experimental results. Two types of models have commonly been used: particle models (e.g., [59, 37, 60, 61, 62]) and fluid models (e.g., [63, 40, 64, 65, 66, 67, 68]).

Particle models track the evolution of a large number of electrons, represented as (super-)particles, and other relevant species. They can be used to study stochastic phenomena such as electron runaway or discharge inception. Another advantage of such models is that no assumptions on the EVDF (electron velocity distribution function) need to be made. In fluid models all relevant species are approximated by densities, which can greatly reduce computational costs. These densities evolve due to fluxes and source terms, which are computed by making certain assumptions about the EVDF. Common is the local field approximation, in which it is assumed that electrons are instantaneously relaxed to the local electric field. Higher-order fluid models can also be used [55, 69]. In principle, it would even be possible to solve the underlying spatio-temporal Boltzmann equation [70, 71], but this is at present computationally infeasible for multi-dimensional streamer simulations.

Both particle models and fluid models with the local field approximation have frequently been used to study positive streamer discharges. Although it is well known that the local field approximation can lead to errors [72, 73], it is not clear how significant these errors are for the modeling of positive streamers. The first goal of this chapter is therefore to study the agreement between particle and fluid simulations of positive streamers in air, using both axisymmetric and 3D simulations. We use a standard particle model of

---

the PIC-MCC (particle-in-cell, Monte Carlo collision) type and a standard drift-diffusion reactions fluid model with the local field approximation.

When comparing models, it is important to have consistent input data computed from the same electron-neutral cross sections. However, transport coefficients for a fluid model can be computed with different types of Boltzmann solvers, and both so-called *flux* and *bulk* coefficients can be computed. Bulk coefficients describe the dynamics of a group of electrons, whereas flux coefficients characterize the properties of individual electrons [54, 55]. Although the use of flux coefficients is generally recommended for plasma modeling [74, 55], it is not fully clear how the use of bulk data affects simulations of positive streamers [75]. Furthermore, with a two-term Boltzmann solver it is possible to use either a spatial or temporal growth model, which lead to different transport coefficients [48]. The second goal of this chapter is therefore to determine the most suitable type of transport data for use in fluid simulations of positive streamers.

**Past work** Below, we briefly discuss some of the past work on the comparison of particle and fluid models for streamer discharges. In [75], four models were compared by simulating a short negative streamer in 3D: a particle model, the ‘classical’ fluid model with the local field approximation, an extended fluid model, and a hybrid particle-fluid model. These simulations were carried out in a 1.2 mm gap using a background electric field well above breakdown, without taking photoionization into account. The classical fluid model here deviated from the other models in terms of streamer velocity and shape, but this was probably due to an implementation flaw that was later found. In [76] three plasma fluid models of different order were compared against particle simulations for planar ionization waves, which can be thought of as “1D” negative streamers. The classical fluid model was found to give rather reasonable results, somewhat in contrast with the conclusions of [73]. Finally, in [45] six streamer codes from different groups were benchmarked against each other, aiming towards model verification. All codes implemented the classical fluid model, and three test cases with positive streamers were considered. Good agreement was found on sufficiently fine grids, and with corresponding small time steps.

Particle and fluid models have also been compared for other types of discharges. In [77] particle, fluid and hybrid models were benchmarked against each other and against experimental data. This review paper fo-

cused on applications related to plasma display panels, capacitively coupled plasmas and inductively coupled plasmas. The authors conclude that “*Excellent agreement can be found in these systems when the correct model is used for the simulation. Choosing the right model requires an understanding of the capabilities and limitations of the models and of the main physics governing a particular discharge.*”. Furthermore, in [78], particle and fluid models were compared for capacitively and inductively coupled argon-oxygen plasmas, in [79] they were compared for atmospheric pressure helium microdischarges, and in [80] they were extensively compared for low-pressure ccrf discharges.

In contrast to the above work, we here compare multidimensional particle and fluid simulations of positive streamers in air, propagating in background fields below breakdown, including photoionization. The chapter is organized as follows. In section 2.2, the particle and fluid models are described as well as the simulation conditions. In section 2.3.1, we first compare axisymmetric and 3D particle and fluid simulations of positive streamers in air, after which the influence of transport data is studied with axisymmetric fluid simulations in section 2.3.2. We then investigate the numerical convergence of both types of models in section 2.3.3, and we determine the dominant source of stochastic fluctuations in the particle simulations in section 2.3.4. Finally, in section 2.3.5, the models are again compared for different applied voltages.

## 2.2 Model description

The particle and fluid models are briefly introduced below, after which the simulation conditions, photoionization and the adaptive mesh are described. We use both axisymmetric and 3D models. For brevity, axisymmetric models will sometimes be referred to as “2D”.

Due to the short time scales considered in this chapter, ions are assumed to be immobile in both the particle and fluid models. Information about the computational cost of simulations is given in Appendix A.

### 2.2.1 Particle (PIC-MCC) model

We use a PIC-MCC (particle-in-cell, Monte-Carlo Collision) model that combines the particle model described in [37] with the Afivo AMR (adaptive mesh refinement) framework described in [41]. Electrons are tracked as particles, ions as densities, and neutrals as a background that electrons stochastically collide with. Below, we briefly introduce the model's main components.

#### Particle mover and collisions

The coordinates  $\mathbf{x}$  and velocities  $\mathbf{v}$  of simulated electrons are advanced with the ‘velocity Verlet’ scheme described in [37]:

$$\mathbf{x}(t + \Delta t) = \mathbf{x}(t) + \Delta t \mathbf{v}(t) + \frac{1}{2} \Delta t^2 \mathbf{a}(t), \quad (2.1)$$

$$\mathbf{v}(t + \Delta t) = \mathbf{v}(t) + \frac{1}{2} [\mathbf{a}(t) + \mathbf{a}(t + \Delta t)], \quad (2.2)$$

where  $\mathbf{a} = -(e/m_e)\mathbf{E}$  is the acceleration due to the electric field  $\mathbf{E}$ , and  $e$  is the elementary charge and  $m_e$  the electron mass.

In axisymmetric simulations particles are evolved as in a 3D Cartesian geometry. However, their acceleration, which is due to an axisymmetric field, is projected onto a radial and axial components before it is used. The acceleration in equation (2.1) is then given by  $\mathbf{a} = (a_r x/r, a_r y/r, a_z)$ , where  $x$  and  $y$  denote the two (3D) particle coordinates corresponding to the radial direction and  $r = \sqrt{x^2 + y^2}$ . In equation (2.2), the radial velocity is updated as

$$\mathbf{v}_{x,y}(t + \Delta t) = \mathbf{v}_{x,y}(t) + \frac{1}{2} \hat{r} [a_r(t) + a_r(t + \Delta t)],$$

where  $\hat{r} = (x, y)/r$ .

Electron-neutral collisions are handled with the null-collision method [81, 37], using collision rates calculated from cross section input data.

#### Super-particles

Due to the large number of electrons in a streamer discharge, it is generally not feasible to simulate all electrons individually. Instead, so-called “super-particles” are used, whose weights  $w_i$  determine how many physical

particles they represent [82]. The procedure followed here is similar to that in [37]. A parameter  $N_{ppc}$  controls the ‘desired’ number of particles per grid cell. We use  $N_{ppc} = 75$ , except for section 2.3.4, in which it is varied. The desired particle weights  $\omega$  are then determined as

$$\omega = n_e \times \Delta V / N_{ppc} \quad (2.3)$$

where  $n_e$  is the electron density in a cell and  $\Delta V$  the cell volume. Furthermore, the minimum particle weight is  $\omega_{\min} = 1$ .

Particle weights are updated when the number of simulation particles has grown by a factor of 1.25, after the AMR mesh has changed, or after 10 time steps in axisymmetric simulations (see below). The particles in a cell for which  $w_i < (2/3) \times \omega$  are merged, by combining two such particles that are close in energy into one with the sum of the original weights. The coordinates and velocity of the merged particle are randomly selected from one of the original particles, see [83]. Particles are split when  $w_i > (3/2) \times \omega$ . Their weight is then halved after which identical copies of these particles are added, which will soon deviate from them due to the random collisions.

In axisymmetric simulations particle weights are updated every ten time steps to reduce fluctuations near the axis. Figure 2.1 illustrates an axisymmetric mesh in which cell volumes depend on the radial coordinate as  $\Delta V = 2\pi r \Delta r \Delta z$ . Cells with small volumes contain fewer physical electrons, and because the minimal super-particle weight is one, stochastic fluctuations in such cells are larger. Furthermore, super-particle weights given by equation (2.3) are proportional to the cell volume. Particles with high weights can therefore cause significant fluctuations when they move towards the axis. We update the particle weights more frequently in axisymmetric simulations to limit these fluctuations.

### Mapping particles to the grid

Particles are mapped to grid densities using a standard bilinear or trilinear weighting scheme, as in [37]. Near refinement boundaries, the mapping is locally changed to the ‘nearest grid point’ (NGP) scheme, to ensure that particle densities are conserved. In axisymmetric coordinates the mapping is also done using bilinear weighting, but the radial variation in cell volumes is taken into account. The interpolation of the electric field from

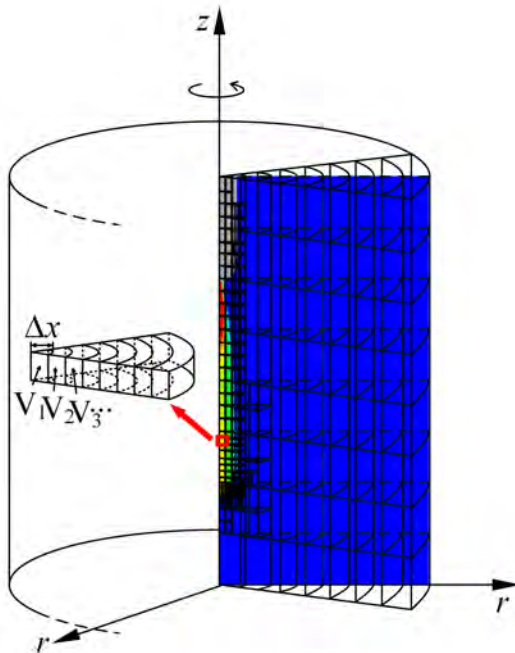


Figure 2.1: Illustration of the adaptive mesh in an axisymmetric streamer simulation, also showing the electron density. The grid is coarser than in an actual simulation. The enlarged view illustrates the relation between cell volumes and radius.

the grid to particles is done using standard bilinear (2D) or trilinear (3D) interpolation. Note that there are more advanced weighting schemes for handling axisymmetric coordinates systems [84], but these approaches are challenging to combine with the cell-centered AMR used in our models.

### Temporal discretization

We use the following CFL-like condition

$$\Delta t_{\text{cfl}} \tilde{v}_{\text{max}} \leq 0.5 \times \Delta x_{\text{min}}, \quad (2.4)$$

where  $\Delta x_{\text{min}}$  indicates the minimum grid spacing, and  $\tilde{v}_{\text{max}}$  is an estimate of the particle velocity at the 90%-quantile. This prevents a few fast particles



from affecting  $\Delta t_{\text{cff}}$ .

Another time step constraint is the Maxwell time, also known as the dielectric relaxation time, which is a typical time scale for electric screening:

$$\Delta t_{\text{drt}} = \varepsilon_0 / (en_{e,\text{max}} \mu_e), \quad (2.5)$$

where  $\varepsilon_0$  is the dielectric permittivity,  $n_{e,\text{max}}$  is the maximal electron density, and  $\mu_e$  the electron mobility, as determined in the local field approximation (see section 2.2.2).

The actual time step is then the minimum of  $\Delta t_{\text{cff}}$  and  $\Delta t_{\text{drt}}$ , and it is furthermore adjusted such that the number of electrons does not grow by more than 20% between time steps.

## Input data

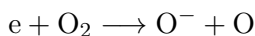
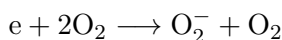
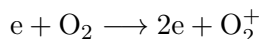
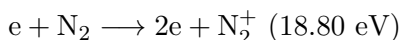
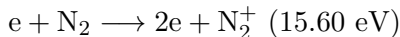
We use Phelps' cross sections for  $\text{N}_2$  and  $\text{O}_2$  [85]. These cross sections contain a so-called *effective* momentum transfer cross sections, which account for the combined effect of elastic and inelastic processes [86]. To use them in particle simulations, we convert them to elastic cross sections by subtracting the sum of the inelastic cross sections. This is an approximate procedure, but the resulting cross sections are suitable for a model comparison.

### 2.2.2 Fluid model

We use a drift-diffusion-reaction fluid model with the local field approximation, as implemented in [40]. The electron density  $n_e$  evolves in time as

$$\partial_t n_e = \nabla \cdot (n_e \mu_e \mathbf{E} + D_e \nabla n_e) + S_R + S_{ph} \quad (2.6)$$

where  $\mu_e$  and  $D_e$  indicate the electron mobility and the diffusion coefficient,  $S_{ph}$  is the non-local photoionization source term (see section 2.2.4), and  $S_R$  is a source term due to the following ionization and attachment reactions:



Ion densities also change due to the above reactions. Transport coefficients and reaction rates are determined using the local field approximation, see section 2.2.2.

## Time integration

Advective electron fluxes are computed using the Koren flux limiter [87] and diffusive fluxes using central differences, see [40] for details. Time integration is performed with Heun’s method, a second order accurate explicit Runge-Kutta scheme. Time steps are limited according to the following restrictions:

$$\begin{aligned} \Delta t_{\text{cfl}} \left( \frac{2N_{\text{dim}}}{\Delta x^2} + \sum \frac{v_i}{\Delta x} \right) &\leq 0.5, \\ \Delta t_{\text{drt}} (en_e \mu_e / \varepsilon_0) &\leq 1, \\ \Delta t &= 0.9 \times \min(\Delta t_{\text{drt}}, \Delta t_{\text{cfl}}), \end{aligned}$$

where  $\Delta t_{\text{cfl}}$  corresponds to a CFL condition (including diffusion),  $\Delta t_{\text{drt}}$  corresponds to the dielectric relaxation time (as in equation (2.5)),  $N_{\text{dim}}$  is the dimensionality of the simulation,  $\Delta t$  is the actual time step used, and  $\Delta x$  stands for the grid spacing, which is here equal in all directions.

## Input data

The fluid model requires tables of transport and reaction data versus electric field strength as input. We use two methods to compute such data from the cross sections that were also used for the PIC model, see section 2.2.1. The first is BOLSIG+, which is a widely used two-term Boltzmann solver [48, 49]. When the electron velocity distribution is strongly anisotropic, for example in high electric fields, the use of the two term approximation can introduce errors [51]. The second method we use is a Monte Carlo swarm code [gitlab.com/MD-CWI-NL/particle\\_swarm](https://gitlab.com/MD-CWI-NL/particle_swarm), similar to e.g. [52, 53]. The basic idea of this approach is to trace electrons in a uniform field, from which transport and reactions coefficients can be obtained.

With the Monte Carlo method we compute both so-called *flux* and *bulk* coefficients [54, 55]. Flux data describes the average properties of individual

electrons, whereas bulk data describes average properties of a group of electrons, taking non-conservative collisions such as ionization and attachment into account. Consider for example a group of electrons, which changes in size due to non-conservative collisions. The bulk drift velocity then describes the average velocity of the center of mass of this group, whereas the flux drift velocity describes the average velocity of individual electrons. These two definitions differ when the probability of non-conservative collisions is not uniform in space, which causes motion of the center of mass.

One of the main differences between bulk and flux data is that in high fields the bulk mobility is higher than the flux mobility, as shown in figure 2.7. Unless mentioned otherwise, the fluid simulations presented in this chapter use Monte Carlo flux data.

### 2.2.3 Computational domain and initial conditions

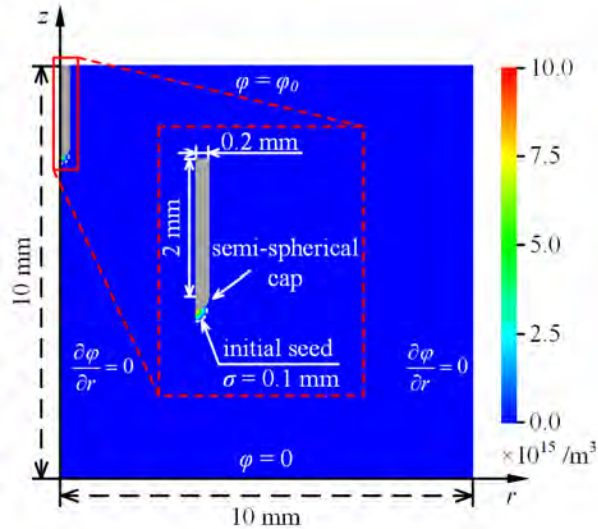


Figure 2.2: Schematic view of the axisymmetric computational domain used for both particle and fluid models, showing the initial electron density and the electrode. 3D simulations are performed in a similarly sized domain, measuring  $20 \text{ mm} \times 20 \text{ mm} \times 10 \text{ mm}$ .

Simulations are performed in artificial air, containing 80% N<sub>2</sub> and 20% O<sub>2</sub>, at  $p = 1$  bar and  $T = 300$  K. We will give electric fields in units of kV/cm. With a gas number density of  $N = 2.414 \times 10^{25} \text{ m}^{-3}$ , assuming the ideal gas law, 1 kV/cm corresponds to about 4.14 Td (Townsend).

The computational domain used for the comparison of cylindrical models is shown in figure 2.2. It measures 10 mm in both the axial and radial directions. For the 3D Cartesian simulations, a similar domain of 20 mm  $\times$  20 mm  $\times$  10 mm is used. A rod-shaped electrode with a semi-spherical cap is placed at center of the domain. This electrode is 2.0 mm long and has a radius of 0.2 mm.

For the electric potential, Dirichlet boundary conditions are applied to the lower and upper domain boundaries, and a homogeneous Neumann boundary condition is applied on the other boundaries. In terms of electrostatics the axisymmetric and 3D simulations are not fully equivalent, because of the different geometry in which these boundary conditions are applied.

For the electron density homogeneous Neumann conditions are applied on all domain boundaries, except for the rod electrode. The electrode absorbs electrons but does not emit them. Since a positive voltage is applied on this electrode, secondary electron emission was not taken into account.

There is initially no background ionization besides an electrically neutral plasma seed that is placed at the tip of the electrode. This seeds helps to start discharges in almost the same way in particle and fluid models. The electron and positive ion densities are given by a Gaussian distribution:

$$n_i(\mathbf{r}) = n_e(\mathbf{r}) = 10^{16} \text{ m}^{-3} \exp \left[ -\frac{(\mathbf{r} - \mathbf{r}_0)^2}{(0.1 \text{ mm})^2} \right], \quad (2.7)$$

where  $\mathbf{r}_0$  is the location of the tip of the electrode, which is at  $z \approx 7.8$  mm.

In particle simulations, these initial densities are converted to  $N = [n_e \Delta V]$  simulation particles per cell, each with a weight of one. A uniform  $[0, 1)$  random number is compared to the remainder to determine whether to add one more particle. The goal of this sampling is to reduce stochastic fluctuations in the initial conditions. The initial particles are spread uniformly within each grid cell, and they initially have zero kinetic energy.

---

## 2.2.4 Photoionization

For streamers in air, photoionization is typically the main source of free electrons. The process results from the interaction between an oxygen molecule and an UV photon emitted from an excited nitrogen molecule. We use Zheleznyak's model for photoionization in air [28] and compute photoionization as in [65]. Assuming that ionizing photons do not scatter and their direction is isotropically distributed, the photoionization source term in equation (2.6) is given by:

$$S_{\text{ph}}(\mathbf{r}) = \int \frac{I(r')f(|\mathbf{r} - \mathbf{r}'|)}{4\pi |\mathbf{r} - \mathbf{r}'|^2} d^3r', \quad (2.8)$$

where  $f(r)$  is the photon absorption function and  $I(\mathbf{r})$  is the source of ionizing photons, which is proportional to the electron impact ionization source term  $S_i$ :

$$I(\mathbf{r}) = \frac{p_q}{p + p_q} \xi S_i, \quad (2.9)$$

where  $p$  is the gas pressure,  $p_q = 40$  mbar is a quenching pressure. For simplicity, we use a constant proportionality factor  $\xi = 0.075$ , except for section 2.3.4, in which  $\xi$  is varied.

We solve equation (2.8) in two ways in this chapter. For fluid simulations, we use the so-called Helmholtz expansion [43, 44]. By approximating the absorption function, the integral in equation (2.8) can be turned into multiple Helmholtz equations that can be solved by fast elliptic solvers. We use Bourdon's three-term expansion, as described in [43] and appendix A of [45].

For particle simulations, we use a discrete Monte Carlo photoionization model as described in [46, 65]. With this model stochastic effects due to discrete single photons are simulated. The basic idea is to stochastically sample the generated photons, their directions, and their travel distances. We also use this approach for the fluid simulations in section 2.3.4, see [65] and chapter 11 of [27] for details.

These two approaches for photoionization differ not only in terms of stochastic effects. Because of the way the absorption function is approximated in the Helmholtz approach, the number of ionizing photons produced and their absorption profile will also be somewhat different. However, such

small differences in photoionization usually have only a minor effect on discharge development, as confirmed by our results in section 2.3.

### 2.2.5 Afivo AMR framework

The open-source Afivo framework [41] is used in both particle and fluid models to provide adaptive mesh refinement (AMR) and a parallel multi-grid solver. Adaptive mesh refinement (AMR) is used for computational efficiency, based on the following criteria [40]:

- refine if  $\alpha(E)\Delta x > c_0$ ,
- de-refine if  $\alpha(E)\Delta x < 0.125c_0$ , but only if  $\Delta x$  is smaller than  $10\ \mu\text{m}$ .

Here  $\Delta x$  is the grid spacing, which is equal in all directions,  $\alpha(E)$  is the field-dependent ionization coefficient, and  $c_0$  is a constant. Furthermore, the grid spacing is bound by  $\Delta x \leq 0.4\ \text{mm}$ . For 3D particle simulations we use  $c_0 = 1.0$  and for all other simulations  $c_0 = 0.8$ . Slightly less refinement is used for the 3D particle simulations because of their large computational cost, see Appendix A. With these values for  $c_0$  numerical convergence errors are reasonably small, as discussed in section 2.3.3.

The geometric multigrid solver in Afivo [41] is used to efficiently solve Poisson's equation  $\nabla^2\phi = \rho/\varepsilon_0$ , where  $\phi$  is the electric potential,  $\varepsilon_0$  the permittivity of vacuum and  $\rho$  the space charge density. Electrostatic fields are then computed as  $\mathbf{E} = -\nabla\phi$ . The same type of multigrid solver is also used to solve the Helmholtz equations for photoionization. To include a needle electrode, we set the applied potential as a boundary condition at the electrode surface. This was implemented by modifying the multigrid methods using a level-set function.

## 2.3 Results

### 2.3.1 Axisymmetric and 3D results

In this section, we compare axisymmetric and 3D particle and fluid models, using the computational configuration and initial condition described in section 2.2.3. A voltage of  $\phi = 11.70\ \text{kV}$  is applied, which results in a

background field of around 15 kV/cm; about half the breakdown field of air.

Photoionization in the fluid model is here computed with the Helmholtz approximation, whereas the particle model uses a Monte Carlo scheme with discrete photons. To account for stochastic fluctuations, ten runs of the 2D cylindrical and 3D particle models are performed, of which five are shown. For the fluid simulations flux transport data from Monte Carlo swarms is used, see section 2.2.2.

Figure 2.3 shows the electron densities and electric fields for the different models at  $t = 10$  ns. The electric field and electron density profiles are similar for all cases, and the streamer head positions are in good agreement, with deviations in streamer length below 5%. Streamer head positions in all models at  $t = 3, 6, 9$  ns are given in table 2.1.

Model	Data	$z$ (3 ns)	$z$ (6 ns)	$z$ (9 ns)
PIC-2D	-	6.45	4.74	2.41
PIC-3D	-	6.45	4.71	2.39
fluid-2D	<b>flux</b>	6.40	4.64	2.31
fluid-3D	<b>flux</b>	6.42	4.66	2.35
fluid-2D	<b>B+ temp.</b>	6.42	4.71	2.47
fluid-2D	<b>B+ spat.</b>	6.72	5.46	3.87
fluid-2D	<b>bulk-a</b>	6.19	4.13	1.34
fluid-2D	<b>bulk-b</b>	6.54	5.04	3.12

Table 2.1: Streamer head position ( $z$ , in mm) at 3, 6 and 9 ns in different simulations, using an applied voltage of 11.7 kV. The bottom part of the table gives results for different types of transport data, see section 2.3.2. Here “**B+ (temp.)**” and “**B+ (spat.)**” respectively refer to flux data computed with BOLSIG+ using temporal growth and spatial growth models, and “**bulk-a**” and “**bulk-b**” refer to two types of bulk coefficients.

With the axisymmetric particle model stochastic fluctuations are visible in the streamer radius and the electron densities. As discussed in section 2.3.4, this is mainly due to the stochastic photoionization used in the particle simulations. Streamers appear to propagate somewhat slower due to these fluctuations. In 3D similar fluctuations are present, but the stream-

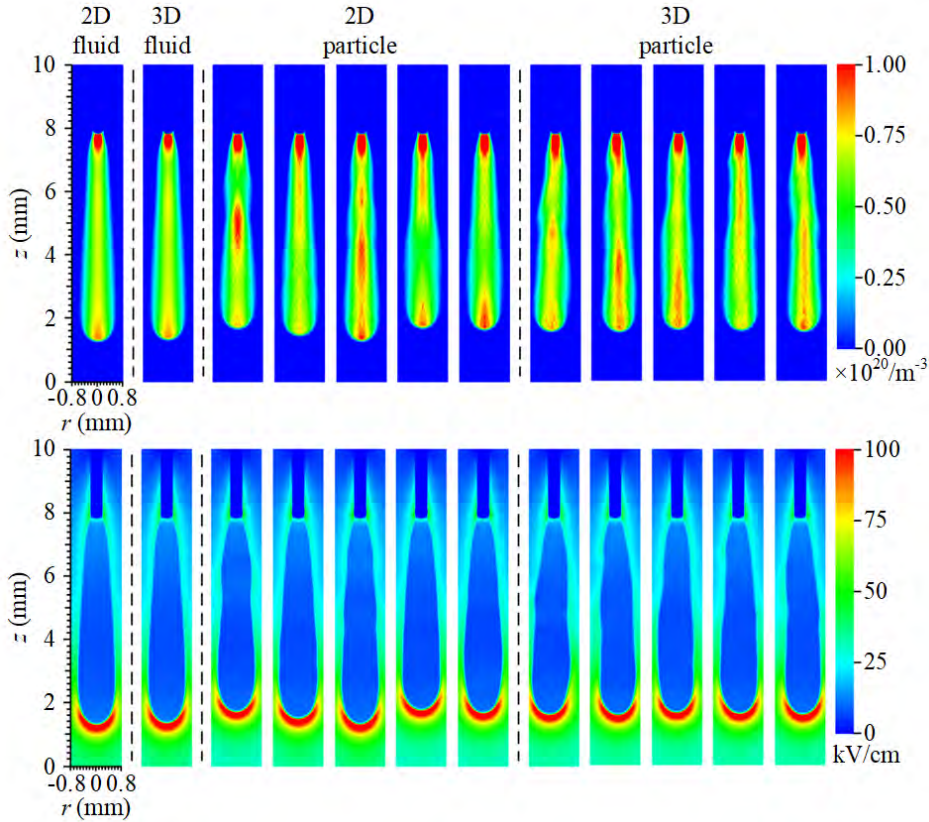


Figure 2.3: The electron densities and electric fields at  $t = 10$  ns for fluid and particle models at an applied voltage of 11.70 kV. The axisymmetric results are mirrored in the symmetry axis. For the 3D simulations cross sections are shown. Multiple runs are shown for the stochastic particle simulations. For the fluid simulations Monte Carlo flux transport data was used.



ers can now move slightly off axis. The 3D particle model can in principle capture realistic stochastic fluctuations, but only if single electrons are used instead of super-particles. This is computationally not feasible for the simulations performed here.

Stochastic fluctuations are not present in the fluid simulations, in which the electron densities and electric fields evolve smoothly in time. The results of the cylindrical and 3D fluid models are nearly identical. Small differences can occur because the computational domains correspond to a rectangle and a cylinder, which means that the applied boundary conditions are not equivalent. Furthermore, the numerical grids and operators are also slightly different in these two geometries.

To more quantitatively analyze the differences between models, the maximal field  $E_{max}$ , the streamer head position  $z$  and streamer velocity  $v$  are shown in figure 2.4. The streamer head position is defined as the  $z$ -coordinate where the electric field is maximal. The velocity is shown versus streamer position, otherwise initial differences grow larger over time even if models agree well later on. The streamer velocity is computed as the numerical derivative of the streamer head position, which amplifies fluctuations. We use a second order Savitzky–Golay filter of width five to compute a smoothed velocity from the position versus time data. For the stochastic particle simulations the average of ten runs is shown.

The maximal electric field follows a similar trend in all models, with first a field of about 180 kV/cm and then a relaxation towards a field of about 130–135 kV/cm as the streamers propagate across the gap. When the streamers approach the grounded electrode the maximal field increases again, because the available voltage difference is compressed in a small region.

The peak electric fields during inception differ somewhat, with the particle model having the highest peak at about 190 kV/cm whereas it is about 180 kV/cm for both fluid models. The relaxation of this peak electric field occurs about 0.4 ns earlier in the fluid model. The main reason for this is that near the electrode, the degree of ionization in the streamer channel is somewhat higher in the particle simulations, which initially leads to stronger field enhancement.

For this study, we have designed the initial conditions such that inception behavior would be similar in the particle and fluid simulations, by

---

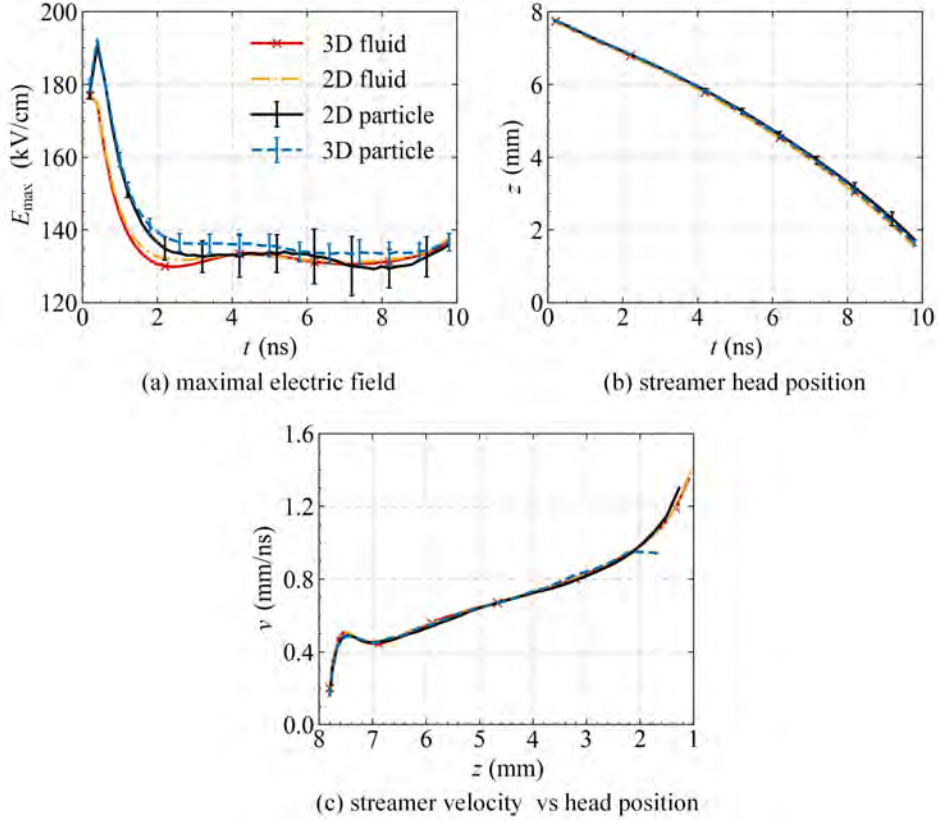


Figure 2.4: Comparison between axisymmetric and 3D particle and fluid simulations at an applied voltage of 11.70 kV. From top to bottom: maximal electric field versus time, streamer head position versus time and front velocity versus streamer position. For the stochastic particle simulations the average of ten runs is shown, and the error bars indicate  $\pm$  one standard deviation.

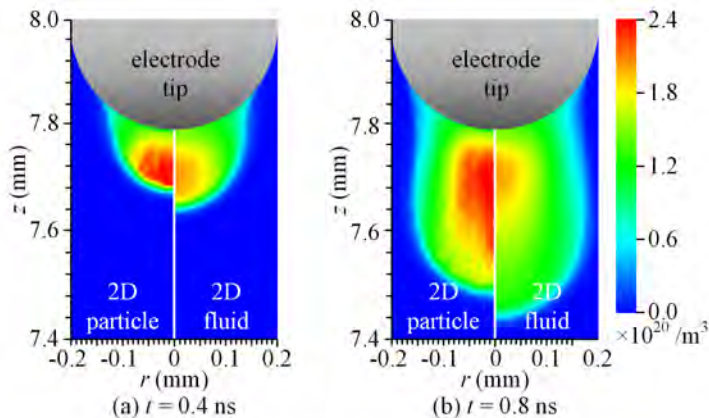


Figure 2.5: Electron density at 0.4 ns and 0.8 ns in the axisymmetric particle and fluid simulations, for an applied voltage of 11.70 kV. Results from one representative particle simulation are shown; stochastic fluctuations are initially small with the initial conditions used here.

using a sharp electrode and a compact initial seed with sufficiently many electrons. If we define inception as the moment at which the streamer crosses the position  $z = 7.6$  mm, then inception is about 0.04 ns faster in the fluid simulations. This is illustrated in figure 2.5, which shows the electron density at 0.4 ns and 0.8 ns for the 2D fluid and particle simulations. The difference in streamer position at these times is primarily caused by faster inception in the fluid model. The difference increases somewhat in time, because a longer streamer propagates faster. Note that the electron density is higher in the particle model.

Faster inception in the fluid model could be due to the local field approximation, with which electrons are assumed to instantaneously relax to the background electric field. Electron multiplication therefore happens more rapidly in the fluid simulations at  $t = 0$  ns, and similarly photoelectrons also instantaneously produce new ionization. We remark that when inception is highly stochastic (with different initial conditions), another difference could be more relevant. With a fluid model low densities always rapidly grow in a high field, even if they correspond to a small probability of an electron being present, as was observed in [88]. Such continuous

growth of a low electron density in high field regions can then lead to faster inception.

There is good agreement among the models for the streamer position versus time, and thus also for the streamer velocities as a function of streamer position. Velocity differences are generally less than 0.04 mm/ns among the models. The mean relative deviation in velocity is below 2%. We compute this quantity as

$$\int |v_a(z) - v_b(z)| dz \Big/ \int v_a(z) dz , \quad (2.10)$$

where  $v_a$  and  $v_b$  denote the velocities in the particle and fluid simulations, which are linearly interpolated between known positions. After inception velocities increase approximately linearly with streamer length. At the end of the gap they increase more rapidly due to boundary effects.

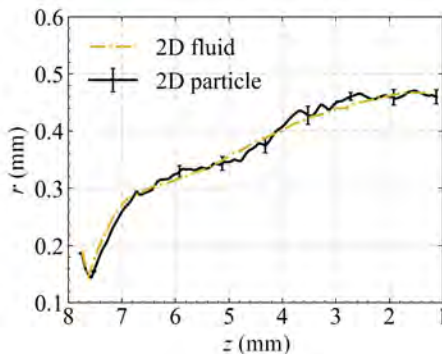


Figure 2.6: Streamer radius versus position for axisymmetric particle and fluid simulations at an applied voltage of 11.70 kV. The streamer radius was here defined as the radius at which  $E_r$ , the radial component of the electric field, is maximal. For the stochastic particle simulations the average of ten runs is shown, and the error bars indicate  $\pm$  one standard deviation.

Figure 2.6 shows the streamer radius versus position in axisymmetric particle and fluid simulations. Good agreement is found between the models, with the maximal difference in radius being below 0.02 mm. Note that there are substantial fluctuations in the radius in the particle simulations as indicated by the error bars. For 3D simulations the radius is harder to

compute, as it depends on the viewing angle. However, as can be seen from figure 2.3, the radius appears to in good agreement between the 2D and 3D simulations.

### 2.3.2 Fluid model transport and reaction data

As mentioned in section 2.2.2, transport and reaction data for a fluid model can be computed using different types of Boltzmann solvers. Furthermore, both so-called *flux* and *bulk* data can be computed. Flux data describes the behavior of individual electrons, whereas bulk data describes the behavior of a group of electrons, taking ionization and attachment into account. We here study how the choice of fluid model input data affects the consistency between particle and fluid simulations. The following types of input data are considered (with labels in bold):

- **(B+ temp.)** Flux data computed with BOLSIG+ using its temporal growth model [48]. With this setting, the two-term approximation is solved by assuming that the electron density grows exponentially in time. This is the default growth model, but it is not clear whether it is the most suitable growth model for streamer simulations [48].
- **(B+ spat.)** Flux data computed with BOLSIG+ using its spatial growth model [48], in which it is assumed that the electron density grows exponentially in space.
- **(flux)** Flux data computed with a Monte Carlo swarm method (available at [gitlab.com/MD-CWI-NL/particle\\_swarm](https://gitlab.com/MD-CWI-NL/particle_swarm)), which uses the same core routines for simulating electrons as our particle model [37].
- **(bulk-a)** Bulk data computed with the same Monte Carlo swarm method. In this variant, only the transport terms in equation (2.6) are modified, by computing the electron flux as  $-n_e\mu_e^B\mathbf{E} - D_e^B\nabla n_e$ , where  $\mu_e^B$  and  $D_e^B$  denote bulk coefficients.
- **(bulk-b)** The same bulk data as above, but in this variant the reaction terms in equation (2.6) are also modified by multiplying them with  $\mu_e^B/\mu_e$ , where  $\mu_e$  denotes the standard flux mobility.

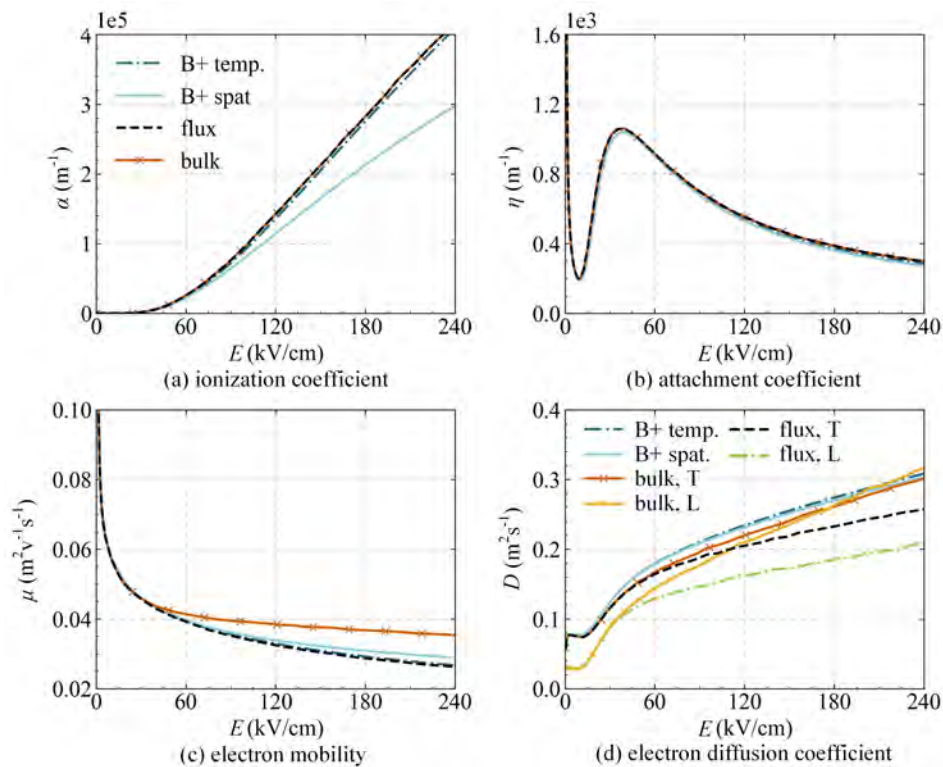


Figure 2.7: Electron transport data. a) Ionization coefficient, b) attachment coefficient, c) electron mobility and d) electron diffusion coefficient. The coefficients were computed for 80%  $\text{N}_2$  and 20%  $\text{O}_2$  at 1 bar and 300 K, using Phelps’s cross sections, see section 2.2.1. For BOLSIG+, data is shown using both a temporal and a spatial growth model. The data labeled “bulk” and “flux” was computed with a Monte Carlo swarm code. Both transverse and longitudinal diffusion coefficients were computed with this technique, but only the transverse coefficients are used in our fluid model.

With the **bulk-a** approach reaction rates are the same as with flux data. However, the number of reactions taking place per unit length (traveled by electrons) is changed, i.e., the so-called Townsend coefficients are different. With the **bulk-b** approach it is the other way around.

Different types of transport data are shown in figure 2.7. Above about 180 Td ionization becomes important and bulk mobilities are larger than flux mobilities. The spatial growth model of BOLSIG+ leads to a significantly smaller ionization coefficient. In high electric fields, its value is about 25-30% less than that of the other approaches. With the Monte Carlo approach both transverse and longitudinal diffusion coefficients are computed, but in our fluid simulations we for simplicity only use the transverse ones. The BOLSIG+ flux diffusion coefficient also corresponds to the transverse direction [86, 48], but it is larger than the Monte Carlo flux coefficient. Such differences between diffusion coefficients computed with a two-term approach and higher-order methods have been observed before, see e.g. [54]. However, the different diffusion coefficients only have a minor impact on our simulations, as shown below.

Figure 2.8 shows axisymmetric fluid simulations with the input data listed above; streamer positions over time are given in table 2.1 and streamer velocities in figure 2.9. There are minor differences in streamer velocity when comparing the BOLSIG+ flux data with temporal growth and the Monte Carlo flux data. When comparing streamer velocities at the same length, relative differences are below 3%. With both types of data good agreement is obtained with the axisymmetric particle simulations. In contrast, the BOLSIG+ data with the spatial growth model leads to a streamer velocity that is much too low, due to the lower ionization coefficient.

Both types of bulk transport data lead to significant deviations compared to the particle model. When only the transport coefficients are changed (**bulk-a**), the streamer is significantly slower and it has a lower degree of ionization. With this data electrons drift faster, but the degree of ionization produced in the streamer channel is lower, leading to a slower discharge. However, when the reaction terms are also changed (**bulk-b**), the streamer propagates too fast. The higher streamer velocity is to be expected, since most terms on the right-hand side of equation (2.6) are now scaled with the bulk mobility.

In conclusion, bulk data and data computed with a spatial growth model

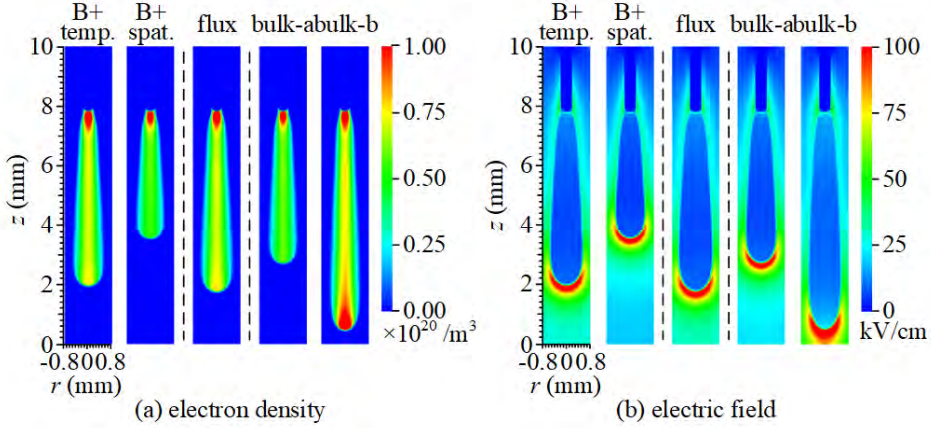


Figure 2.8: Electron densities and electric fields at  $t = 9.6$  ns for axisymmetric fluid simulations with an applied voltage of 11.7 kV. Different types of transport data are used, from left to right: BOLSIG+ with temporal growth, BOLSIG+ with spatial growth, Monte Carlo flux data, and two types of Monte Carlo bulk data. With **bulk-a** only transport terms are modified, and with **bulk-b** reaction terms are also scaled with the bulk mobility.

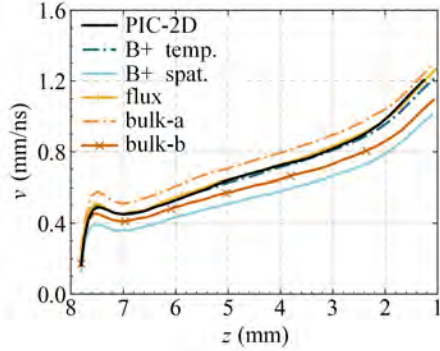


Figure 2.9: Streamer velocity versus streamer head position for different types of transport data. The labels are explained in figure 2.8 and in section 2.3.2.



are not recommended for the simulation of positive streamers. With flux transport data there are minor differences between BOLSIG+ data computed with a temporal growth model and Monte Carlo data, but both lead to good agreement with the particle simulations.

### 2.3.3 Mesh refinement and numerical convergence

We here study the sensitivity of the particle and fluid simulations to the grid spacing, to test whether our simulations are close to numerical convergence. To control the grid spacing, the refinement parameter  $c_0$  is varied, see section 2.2.5. Note that the time step in both models will also be affected by the grid spacing, as explained in section 2.2.1 and 2.2.2.

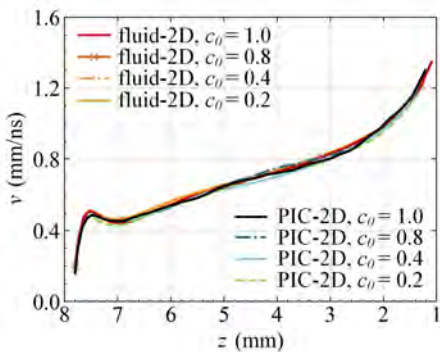


Figure 2.10: Streamer front velocities versus streamer head position for different refinement criteria. Other conditions are the same as in section 2.3.1. For the particle simulations the average of ten runs is shown to reduce stochastic fluctuations.

Figure 2.10 shows streamer velocities versus streamer position for  $c_0$  values of 1.0, 0.8, 0.4 and 0.2, for which the minimal grid spacing is 3.9, 3.9, 1.9, and 0.9  $\mu\text{m}$ , respectively. Streamer positions at  $t = 3, 6$  and  $9$  ns are given in table 2.2. With the fluid model, deviations in length at  $t = 9$  ns are about 3% with  $c_0 = 0.8$  compared to the finest-grid case. With the particle model, there are statistical fluctuations that make it harder to establish numerical convergence, but at  $t = 9$  ns streamer lengths are also within 3% for all tested cases. When comparing the streamer velocity

---

Simulating Positive Streamer Discharges in Air

---

Model	$c_0$	$z$ (3 ns)	$z$ (6 ns)	$z$ (9 ns)
PIC-2D	0.2	$6.51 \pm 0.02$	$4.81 \pm 0.09$	$2.59 \pm 0.11$
PIC-2D	0.4	$6.45 \pm 0.03$	$4.74 \pm 0.04$	$2.54 \pm 0.06$
PIC-2D	0.8	$6.45 \pm 0.03$	$4.74 \pm 0.11$	$2.41 \pm 0.21$
PIC-2D	1.0	$6.45 \pm 0.04$	$4.71 \pm 0.13$	$2.45 \pm 0.13$
fluid-2D	0.2	6.37	4.54	2.14
fluid-2D	0.4	6.37	4.55	2.17
fluid-2D	0.8	6.40	4.64	2.31
fluid-2D	1.0	6.42	4.67	2.35

Table 2.2: Streamer head position ( $z$ , in mm) at 3, 6 and 9 ns, using an applied voltage of 11.7 kV. Different values of the refinement parameter  $c_0$  are used, see section 2.2.5. For the particle simulations averages over ten runs are shown, together with the standard deviation of the sample. Streamer lengths are given by  $7.8 \text{ mm} - z$ .

versus position for  $c_0 = 0.8$  and  $c_0 = 0.2$ , convergence errors are about 1% for the fluid model and about 2% for the particle model, using equation (2.10).

Table 2.2 allows to compare differences in streamer length between particle and fluid simulations using the same refinement. Interestingly, these differences are larger on finer grids: with  $c_0 = 0.2$ , the relative differences in streamer length are about 8–10% at 3, 6 and 9 ns, whereas for  $c_0 = 0.8$  they are about 2–4%. For streamer velocities (compared at the same streamer length) the mean deviations are about 4% and 2% for these two cases, using equation (2.10).

Based on the above, we conclude that numerical convergence errors are relatively small for our default refinement parameter  $c_0 = 0.8$  – they do at least not exceed the intrinsic differences between the models, which are already quite small. For the test case considered here, with an applied voltage of 11.7 kV, the difference in streamer velocity is about twice as large (4% instead of 2%) on the finest grid. The main reason for this is that in the fluid simulations, which are more sensitive to the grid refinement, the streamer velocity is somewhat higher on finer grids. In section 2.3.5 we show that for higher applied voltages, the velocity is actually higher

in the particle simulations. We therefore expect that using a finer grid somewhat increases model discrepancies for lower applied voltages, and that is somewhat reduces model discrepancies for higher applied voltages.

### 2.3.4 Stochastic fluctuations

To investigate the source of stochastic fluctuations in the axisymmetric simulations we vary two parameters. The first is the photoionization factor  $\xi$ , see equation (2.9), which is a proportionality factor that relates the number of UV photons produced to the electron impact ionization source term. It therefore directly controls the amount of photoionization. To study how  $\xi$  affects stochastic behavior, we use the discrete photoionization model in both the particle and the fluid simulations presented here. The second parameter we vary is  $N_{ppc}$ , which controls the ‘desired’ number of particles per cell in particle simulations, see equation (2.3).

Figure 2.11 shows results of axisymmetric particle and fluid models for  $\xi = 0.0375, 0.075, 0.15$  and  $N_{ppc} = 50, 100, 200$ . In both models the streamer length is not sensitive to the amount of photoionization, as was also observed in e.g. [89]. However, fluctuations in the electron density are significantly larger for the  $\xi = 0.0375$  case, whereas these fluctuations are reduced for the  $\xi = 0.15$  case, as was also observed in [65]. With  $\xi = 0.0375$  we even observed branching in a few of the simulation runs, which is probably due to increased density fluctuations near the  $z$ -axis when the amount of photoionization is decreased. Fluctuations in the streamer radius are also larger for a lower value of  $\xi$ . When  $N_{ppc}$  is increased, fluctuations in electron densities and streamer radius are slightly reduced, but the effect is weaker than that of the  $\xi$  parameter. We therefore conclude that the discrete photoionization model is responsible for most of the stochastic fluctuations in our results. This confirms the assumptions made in recent work [65, 90], in which fluid models were used to demonstrate the importance of stochastic photoionization on streamer branching.

Finally, we remark that in figure 2.11 the stochastic fluctuations are demonstrated with axisymmetric models, in which these fluctuations are not completely physical. We have also performed 3D fluid simulations with stochastic photoionization, in which these fluctuations looked qualitatively similar to those shown in figure 2.3 for the 3D particle model. However, a statistical comparison of these 3D models for the parameter range shown

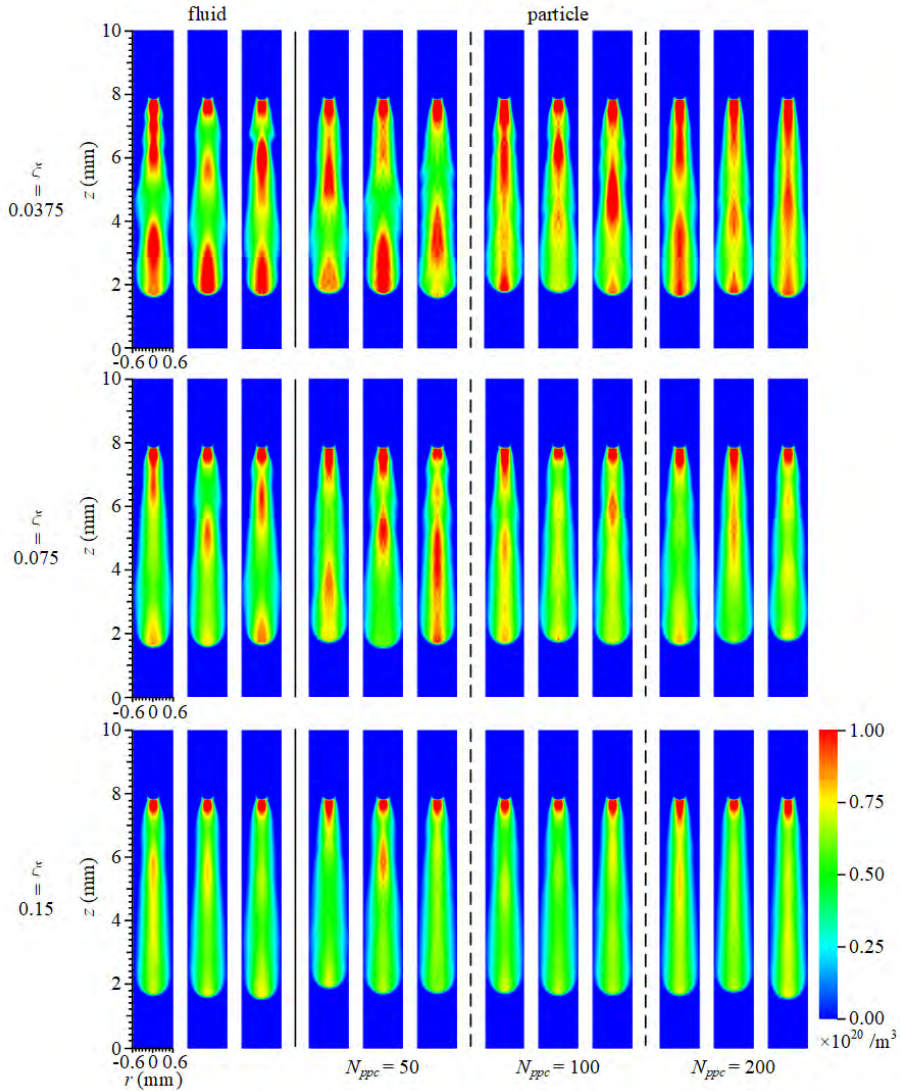


Figure 2.11: Electron densities at  $t = 10$  ns in axisymmetric fluid and particle simulations. For each combination of two parameters, three runs are shown. Stochastic photoionization is now also used in the fluid model. The condition are otherwise the same as in section 3.1.

in figure 2.11 could not be performed due to the high computational costs of the 3D particle simulations.

### 2.3.5 Results at different voltages

Figure 2.12 shows results for particle and fluid simulations at a higher applied voltage of 14.04 kV, which results in a background electric field of about 18 kV/cm. All the other parameters are the same as in section 2.3.1. For the 3D particle model results at later times are missing, because these simulations exceeded the memory and time constraints of our computational hardware, see Appendix A.

At this higher voltage, the agreement between the models is of similar quality as in figure 2.4, but there are a few differences. Figure 2.12(a) shows that inception is significantly faster. The relaxation of the initial high field takes place in about 1 ns, so roughly twice as fast, and the curves for the maximal electric field are now in better agreement. With a higher applied voltage the streamer velocity is higher, but the propagation is otherwise similar to that in figure 2.4. The agreement between the models is still good: between the 2D particle and 2D fluid simulations, the mean deviation in velocity (compared at the same streamer length) is about 1%. However, the discrepancy between the 2D and 3D fluid simulations is now somewhat larger. This is probably due to the difference in computational domains and electrostatic boundary conditions in 2D and 3D, which could play a stronger role for a more conducting streamer channel at a higher voltage. The sensitivity of discharge simulations to these boundary conditions was recently observed in [88].

Figure 2.13 shows the relative difference  $\Delta_L$  in streamer length between axisymmetric particle and fluid models for applied voltages from 11.70 kV to 15.60 kV. These voltages correspond to background electric fields of about 15 kV/cm to 20 kV/cm. The difference is computed as

$$\Delta_L = (L_{\text{fluid},2\text{D}} - L_{\text{pic},2\text{D}})/L_{\text{pic},2\text{D}},$$

where  $L_{\text{fluid},2\text{D}}$  and  $L_{\text{pic},2\text{D}}$  are the streamer lengths in the fluid and particle model at a particular time.

In all cases,  $\Delta_L$  peaks during streamer inception. This happens because inception occurs faster in the fluid model, as explained in section 2.3.1, and

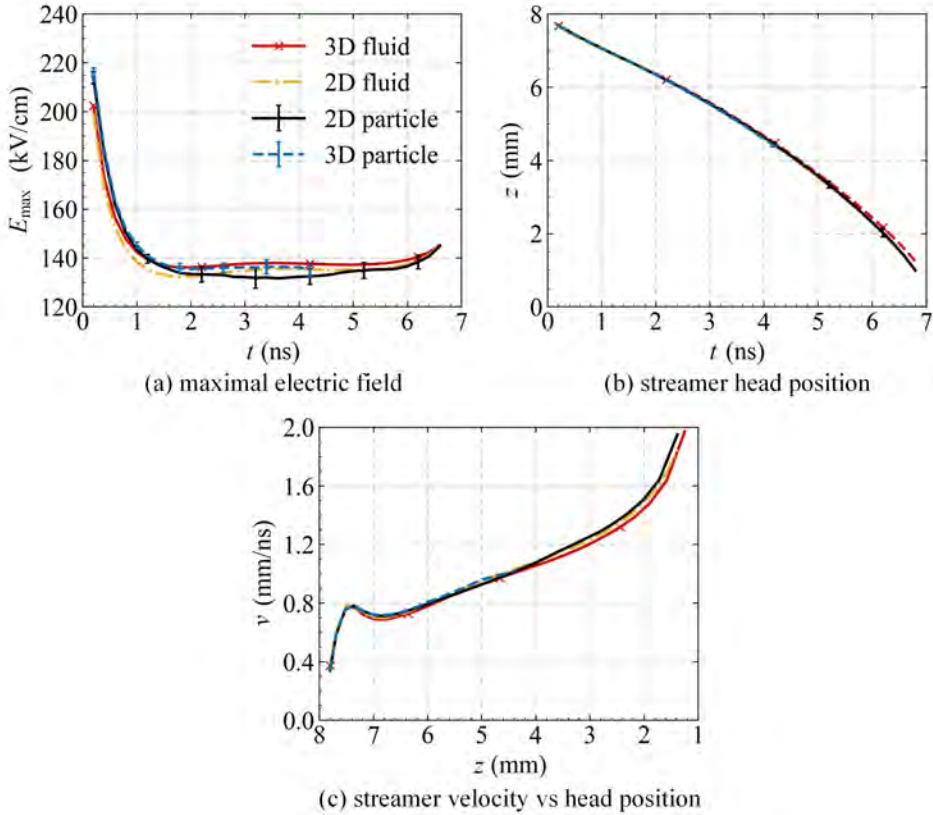


Figure 2.12: Comparison between axisymmetric and 3D particle and fluid models at an applied voltage of 14.04 kV, similar to figure 2.4. From top to bottom: the maximal electric field and streamer position versus time, and streamer velocity versus streamer position. For the particle model the average of ten runs is shown with error bars indicating  $\pm$  one standard derivation.

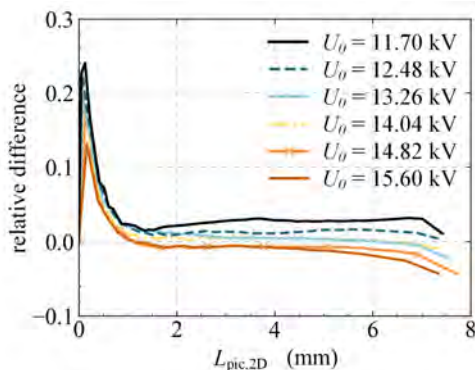


Figure 2.13: The relative difference  $\Delta_L$  in streamer length versus time, shown for axisymmetric particle and fluid simulations at several voltages. The difference is computed as  $\Delta_L = (L_{\text{fluid},2\text{D}} - L_{\text{pic},2\text{D}})/L_{\text{pic},2\text{D}}$ . Besides the applied voltage, simulations conditions are the same as in section 2.3.1.

because the denominator is initially small. For higher applied voltages, the initial peak in  $\Delta_L$  becomes smaller.

In which model the streamer has advanced the furthest at a particular time depends on the applied voltage. When  $U_0$  is lower than 14.04 kV,  $\Delta_L$  is generally positive, whereas for higher voltages it becomes negative. This indicates that relative to the fluid simulations, the velocity in the particle simulations is higher at higher voltages. The mean deviations between velocities in the particle and fluid simulations are 1.8% (11.7 kV case), 1.9% (12.48 kV), 1.3% (13.26 kV), 1.3% (14.04 kV), 1.4% (14.82 kV) and 2.4% (15.6 kV).

## 2.4 Conclusions

We have quantitatively compared a PIC-MCC (particle-in-cell, Monte Carlo collision) model and a drift-diffusion-reaction fluid model with the local field approximation for simulating positive streamer discharges. The simulations were performed in air at 1 bar and 300 K, in background fields below breakdown ranging from 15 kV/cm to 20 kV/cm, using both axisymmetric and fully three-dimensional geometries.

We have found surprisingly good agreement between the particle and fluid simulations. Streamer properties such as maximal field, radius, and velocity were all very similar. When compared at the same streamer length, the mean difference in streamer velocity was generally below 4%. One source of differences was the photoionization model, for which we used a stochastic approach in the particle simulations and a continuum approach in most of the fluid simulations.

We have investigated the effect of different types of transport data in fluid models, how well the models are numerically converged, what the main source of stochastic fluctuations is, and how the agreement between the models is affected by the applied voltage. Our main conclusions on these topics are:

- The type of transport data used in a fluid model is important. By using flux transport coefficients computed with a Monte Carlo approach or BOLSIG+ (using its temporal growth model), good agreement is obtained between the fluid and particle simulations. The use of bulk coefficients leads to either faster or slower streamer propagation, depending on how the coefficients are used. Data computed with the spatial growth model of BOLSIG+ leads to a significantly slower streamer discharge.
- Numerical convergence errors are small in the particle and fluid simulations presented here. We have compared axisymmetric particle and fluid simulations with grid refinement satisfying  $\alpha(E)\Delta x < c_0$  for  $c_0 = 0.2, 0.4, 0.8$  and  $1.0$ , where  $\alpha(E)$  is the ionization coefficient. For an applied voltage of 11.7 kV, convergence errors in streamer velocity (compared at the same position) were about 1% for the fluid simulations and about 2% for the particle simulations. On the finest grids, streamer velocities increased slightly in the fluid simulations.
- Stochastic fluctuations are visible in axisymmetric and 3D particle simulations, for example in the streamer's degree of ionization, maximal electric field and radius. In our simulations, the dominant source of these stochastic fluctuations is discrete photoionization. Fluid simulations with the same discrete photoionization model exhibit similar fluctuations as particle simulations. Due to these fluctuations,



streamers in 3D simulations propagate slightly off-axis. In the particle simulations, the number of particles per cell did not significantly affect these fluctuations.

- Axisymmetric simulations were performed for applied voltages between 11.7 kV to 15.6 kV, corresponding to background fields of about 15 kV/cm to 20 kV/cm. Discrepancies in streamer length (versus time) between particle and fluid simulations were generally below 3%. The mean deviations in streamer velocity (versus length) were about 2% for all applied voltages. Other streamer properties, such as the maximal electric field, were also in good agreement.

Finally, we expect differences between particle and fluid models to increase at lower applied electric fields. Inception will be more stochastic, and a smaller streamer radius in lower fields will lead to steeper gradients in the electron density and electric field, which could increase errors due to the local field approximation. However, a comparison in lower fields, in which streamer branching would probably have to be taken into account, is left for future work.



## Chapter 3

# A comparison of 2D Cartesian and 2D axisymmetric models for positive streamer discharges in air

Simulating streamer discharges in 3D can computationally be very expensive, which is why 2D Cartesian simulations are sometimes used instead, especially when dealing with complex geometries. Although 2D Cartesian simulations can only be used to obtain qualitative results, it is nevertheless interesting to understand how they differ from their 3D or axisymmetric counterparts. We therefore compare 2D Cartesian and axisymmetric simulations of positive streamers in air, using a drift-diffusion-reaction fluid model with the local field approximation. With the same electrode length and width, inception voltages are found to be about a factor two higher in the 2D Cartesian case. When compared at the same applied voltage, the 2D Cartesian streamers are up to four times thinner and slower, their maximal electric field is about 30% lower and their degree of ionization is about 65% lower, with the largest differences occurring at the start of the discharge. When we compare at a similar ratio of applied voltage over inception voltage, velocities become rather similar, and so do the streamer radii at later propagation times. However, the maximal electric field in the 2D Cartesian case is then about 20-30% lower, and the degree of ionization is about 40-50% lower. Finally, we show that

streamer branching cannot qualitatively be modeled in a 2D Cartesian geometry.

### 3.1 Introduction

Streamer discharges play an important role in the early stages of electric discharges [9], as they generate the first ionized paths that can later become leaders or sparks. Due to their electric field enhancement, streamers can propagate into regions where the electric field is below the breakdown threshold of the insulating medium. Streamer discharges often form a complex tree-like structure with many branched channels. They are widely used in plasma and high voltage technology [91, 92, 93], and they appear in thunderstorms as streamer coronas ahead of lightning leaders or as sprite discharges high above thunderclouds [94, 95, 10].

Over the past decades, numerical simulations have been widely used to study streamer discharges. Two types of models are commonly used, namely particle models [59, 37, 60, 61, 62] and fluid models [63, 40, 64, 66, 67, 68, 96]. Simulations have been performed in different computational geometries. 3D Cartesian simulations are the most realistic, but also the most expensive. A fine grid is required to accurately describe the thin charge layers and steep density gradients around streamer channels, and small time steps are required to describe the non-linear evolution of these channels. Axisymmetric simulations are much cheaper to perform, as the solution only has to be evolved in two spatial coordinates ( $r, z$ ). For single channels propagating in a straight line, identical results can be obtained as with a full 3D model, see e.g. [56]. On the other hand, real streamer discharges are generally not axisymmetric, for example due to branching or other stochastic effects, or because of their interaction with dielectrics or electrodes. In 2D Cartesian simulations, discharges evolve in  $x, y$  coordinates while it is assumed there is no variation in the  $z$ -direction. Such simulations therefore describe planar discharges with an infinite extent in the  $z$ -direction, which can be a reasonable approximation for surface discharges that are approximately planar.

Because of the high cost of 3D simulations, 2D Cartesian simulations are often used to qualitatively study streamer discharges in complex geometries, which would in reality not be planar. The goal of this chapter is to be able to better interpret results of such 2D Cartesian simulations, by comparing them to axisymmetric simulations of positive streamers in air. A planar discharge is expected to have weaker electric field enhancement, because

---

its space charge layer is curved in only one instead of two dimensions. We aim to understand how this difference affects streamer properties and the conditions for streamer inception.

Below, we briefly mention some of the past work on streamer discharges using 2D Cartesian simulations. Such simulations have frequently been used to describe surface dielectric barrier discharges (SDBDs). We remark that depending on the conditions, SDBDs can be approximately planar but they can also be highly filamentary, see e.g. [97, 98, 99].

Soloviev *et al* used a 2D Cartesian fluid model to study SDBDs in atmospheric air [100, 101]. Singh *et al* used a 2D Cartesian fluid model to simulate the propagation of streamer discharges towards and then along a solid surface, taking into account charge transport in the dielectric. Meyer *et al* [102] used a 2D planar fluid model to simulate positive surface streamers and the surface charge distribution on a grounded dielectric barrier. The same model was used to study streamer propagation along a dielectric surface with a wave-like profile in [103]. In [104, 105], positive and negative streamers propagating over a dielectric surface were studied using a 2D Cartesian fluid model. In [106], a two dimensional fluid model (nonPDPSIM) was used to simulate the propagation of discharges through interconnected pores in dielectric materials. In [107], the interaction of positive streamers in air with bubbles floating on liquid surfaces was computationally studied with a 2D Cartesian fluid model.

The outline of the chapter is as follows. In section 3.2, the fluid models and the input data are described. In section 3.3.1, we compare 2D Cartesian and axisymmetric simulations of positive streamers in air at the same applied voltage. Inception voltages are compared in section 3.3.2, and simulations are compared at different applied voltages in section 3.3.3. Finally, we discuss the effect of a 2D Cartesian geometry on streamer branching in section 3.3.5.

## 3.2 Model description

Simulations are performed using Afivo-streamer, a code for drift-diffusion-reaction fluid simulations [40]. The electron density evolves in time as

$$\partial_t n_e = \nabla \cdot (n_e \mu_e \mathbf{E} + D_e \nabla n_e) + S_i - S_a + S_{\text{ph}}. \quad (3.1)$$

Here  $\mu_e$  and  $D_e$  are the electron mobility and diffusion coefficient, which are assumed to be functions of the local electric field.  $S_{\text{ph}}$  is a non-local photoionization source term discussed below, and  $S_i$ - $S_a$  are source terms due to ionization ( $S_i$ ) and attachment ( $S_a$ ) reactions, see section 3.2.2. Ions and neutral species are assumed to be immobile, and their densities  $n_j$  (for  $j = 1, 2, \dots$ ) evolve as

$$\partial_t n_j = S_j, \quad (3.2)$$

where the source terms  $S_j$  are determined by the reaction list, see section 3.2.2. The electric field is computed as  $\mathbf{E} = -\nabla\phi$ , where the electric potential  $\phi$  is obtained by solving Poisson's equation using a parallel multi-grid solver [108, 40]. The fluid equations are solved with a finite-volume method and explicit time integration, as described in [40].

Photoionization is included according to Zhelenznyak's model [28] using the Helmholtz approximation, using the three-term expansion given in [43]. The parameters used for photoionization are the same as those in [65].

In section 3.3.5, we additionally show some results with stochastic photoionization, which is implemented as a Monte-Carlo method with discrete photons, see [65] for details.

The Afivo-streamer code includes adaptive mesh refinement (AMR), as described in [40, 41]. As a refinement criterion we use  $\alpha(E)\Delta x < 1$ , where  $\Delta x$  is the grid spacing and  $\alpha(E)$  is the field-dependent ionization coefficient. The mesh is de-refined if  $\alpha(E)\Delta x > 0.125$ , but only if  $\Delta x$  is smaller than  $10 \mu\text{m}$ .

### 3.2.1 Simulation conditions and computational domain

Simulations are performed in artificial air (80%  $\text{N}_2$ , 20%  $\text{O}_2$ ) at 1 bar and 300 K. The computational domain used for the 2D Cartesian simulations measures  $20 \text{ mm} \times 10 \text{ mm}$ , and a corresponding domain with a radius of 10 mm and a height of 10 mm is employed for the axisymmetric model, see figure 3.1(b). We include a rod electrode with a semi-spherical cap to get electric field enhancement. The electrode is 2 mm long and has a radius of 0.2 mm. Note that in the 2D Cartesian model, this rod actually becomes a blade-like electrode, see figure 3.1(a).

A Dirichlet boundary condition is used for the electric potential at upper and lower domain boundaries, and a homogeneous Neumann bound-

Table 3.1: Reactions included in the model. Rate coefficients for  $k_1$  to  $k_5$  were computed using BOLSIG+ [48, 49] from Phelps' cross sections [85, 109], and  $k_6$  to  $k_8$  were obtained from [1].

Reaction	Rate coefficient
$e + N_2 \xrightarrow{k_1} e + e + N_2^+$	$k_1(E/N)$
$e + O_2 \xrightarrow{k_2} e + e + O_2^+$	$k_2(E/N)$
$e + O_2 + O_2 \xrightarrow{k_3} O_2^- + O_2$	$k_3(E/N)$
$e + O_2 \xrightarrow{k_4} O^- + O$	$k_4(E/N)$
$e + N_2 \xrightarrow{k_5} e + N_2(C^3\Pi_u)$	$k_5(E/N)$
$N_2(C^3\Pi_u) + N_2 \xrightarrow{k_6} N_2 + N_2$	$k_6 = 0.13 \times 10^{-16} \text{ m}^3\text{s}^{-1}$
$N_2(C^3\Pi_u) + O_2 \xrightarrow{k_7} N_2 + O_2$	$k_7 = 3.0 \times 10^{-16} \text{ m}^3\text{s}^{-1}$
$N_2(C^3\Pi_u) \xrightarrow{k_8} N_2(B^3\Pi_g)$	$k_8 = 1/(42 \text{ ns})$

ary condition is applied on the other boundaries. Homogeneous Neumann boundary conditions are also used for species densities at all domain boundaries.

Figure 3.1(c) shows that the electric field enhancement at the electrode tip is about 2.6 times higher in the 2D axisymmetric model, namely 310 kV/cm compared to 120 kV/cm. This higher field decays more rapidly, so that farther away from the electrode the field is slightly higher in the 2D Cartesian model (the area under both curves is equal). In both models, the electric field far away from the electrode is approximately equal to the average electric field  $E_{bg} = 25 \text{ kV/cm}$  between the plate electrodes.

As an initial condition, a homogeneous background ionization density of  $1 \times 10^{10} \text{ m}^{-3}$  electrons and positive ions is included, which provides initial free electrons so that a discharge can start.

### 3.2.2 Input data

We use Phelps' cross sections for  $N_2$  and  $O_2$  [110, 86, 85, 109] and a relatively simple plasma chemistry, see table 3.1. Electron transport coefficients ( $\mu_e$  and  $D_e$ ) and reaction rates are computed using BOLSIG+ [49, 48]. To get the optical radii of simulated streamers, we included the  $N_2(C^3\Pi_u \rightarrow B^3\Pi_g)$  transition in the reaction list, since it is the main source of emitted



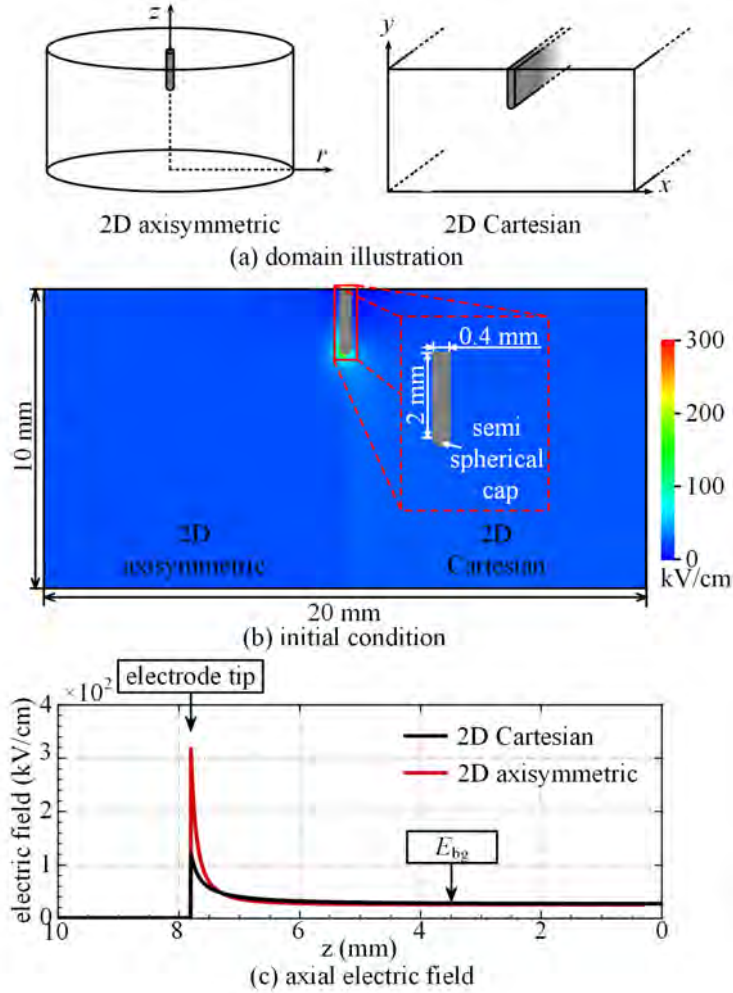


Figure 3.1: (a) Illustration of the 2D Cartesian and 2D axisymmetric computational domains. (b) The electrode and the electric field strength in the computational domains. (c) Profile of the electric field strength along a central axis in the two models, for an applied voltage of 25 kV/cm.  $E_{bg}$  is the average electric field between the plate electrodes.

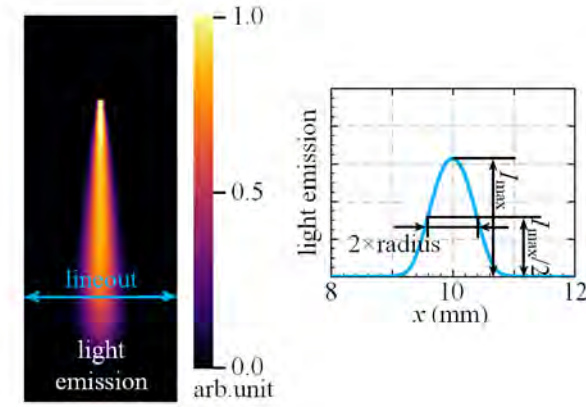


Figure 3.2: Illustration of how the streamer radius is determined from the light emission profile. At a given position, the full width at half maximum (FWHM) is determined by taking a line-of-sight integrated profile of the light emission, after which the radius is given by half of the FWHM.

light [111] in  $N_2$ - $O_2$  mixtures close to atmospheric pressure.

### 3.2.3 Computation of streamer radius

There are different definitions of the streamer radius. In this chapter we use the optical radius, defined as half of the FWHM (full width at half maximum) of the time-integrated light emission, see figure 3.2. For axisymmetric simulations, a forward Abel transform is first performed to compute the light emission profile as it would be observed experimentally.

## 3.3 Results

### 3.3.1 Comparison under the same applied voltage

In this section, 2D Cartesian and 2D axisymmetric simulations of positive streamer discharges are compared using the same applied voltage of  $U_0 = 25$  kV, which results in a background field of 25 kV/cm. Figure 3.3 shows the electron density and the electric field from a 2D Cartesian simulation at  $t = 7.8$  ns and a 2D axisymmetric simulation at  $t = 2.9$  ns. Corresponding

profiles of the maximal electric field, the streamer velocity and the streamer radius are shown in figure 3.4.

A much smaller streamer radius can be observed in the 2D Cartesian model, as well as a lower electric field at the streamer head and a lower channel conductivity. Normally, one would expect a higher maximal field for a smaller streamer radius, so these differences are caused by the lower electric field enhancement in a 2D Cartesian geometry. Both the radius and the velocity are initially already significantly higher in the axisymmetric model. The maximal electric field relaxes to about 150 kV/cm in the axisymmetric model and to about 100 kV/cm in the 2D Cartesian model.

The two models clearly give rather different results when compared at the same applied voltage. Due to the lower electric field enhancement in a 2D Cartesian geometry we have to use a relatively high voltage to get a discharge started. In the axisymmetric simulations, this voltage is well above the inception voltage, leading to the formation of a wide and fast-propagating discharge channel.

### 3.3.2 Effect of electrode geometry on inception voltage

In table 3.2, inception voltages are compared between the two models, defined as the lowest applied voltage that can initiate a streamer discharge. The same computational domain as before is used, but we vary the electrode length and radius. On average, inception voltages in the 2D Cartesian model are about two times higher than in the axisymmetric model. Note that the inception voltage is somewhat more sensitive to the electrode geometry in the axisymmetric model due to the stronger field enhancement in this geometry.

### 3.3.3 comparison around streamer inception voltage

We now compare 2D Cartesian and axisymmetric simulations at different applied voltages, considering two cases: a comparison at the same applied voltage  $U_0$ , and a comparison at a similar value of  $U_0/U_{\text{inc}}$ , where  $U_{\text{inc}}$  is the inception voltage. With the electrode geometry used in section 3.3.1,  $U_{\text{inc}} = 19.0\text{ kV}$  for the 2D Cartesian model and  $U_{\text{inc}} = 10.4\text{ kV}$  for the axisymmetric model, see table 3.2.

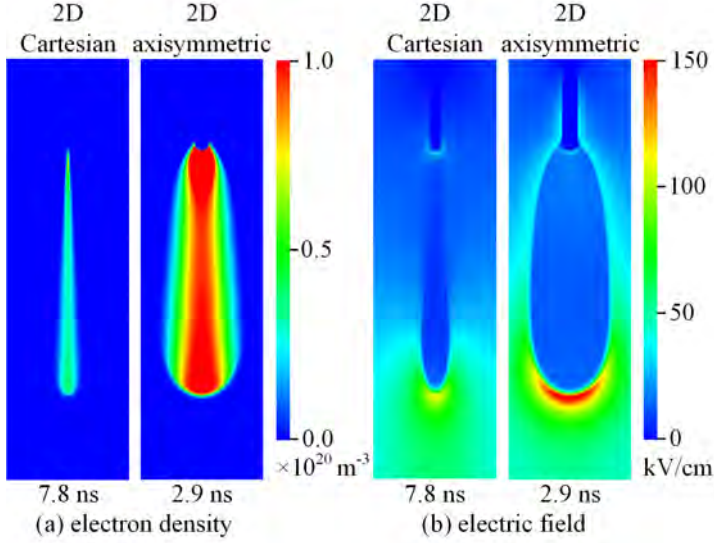


Figure 3.3: Comparison of electron density and electric field profiles for positive streamer discharges with an applied voltage of  $U_0 = 25 \text{ kV/cm}$ . Results are shown when the streamers are approximately at the same position in the 2D Cartesian and axisymmetric simulations.

Table 3.2: Streamer inception voltages  $U_{\text{inc}}$  for different electrode radii and electrode lengths.

	electrode length	electrode radius		
		0.2 mm	0.15 mm	0.1 mm
2D Cartesian	2 mm	19.0 kV	18.4 kV	17.6 kV
	3 mm	15.8 kV	15.2 kV	14.4 kV
Axisymmetric.	2 mm	10.4 kV	9.6 kV	8.3 kV
	3 mm	7.9 kV	7.2 kV	6.1 kV

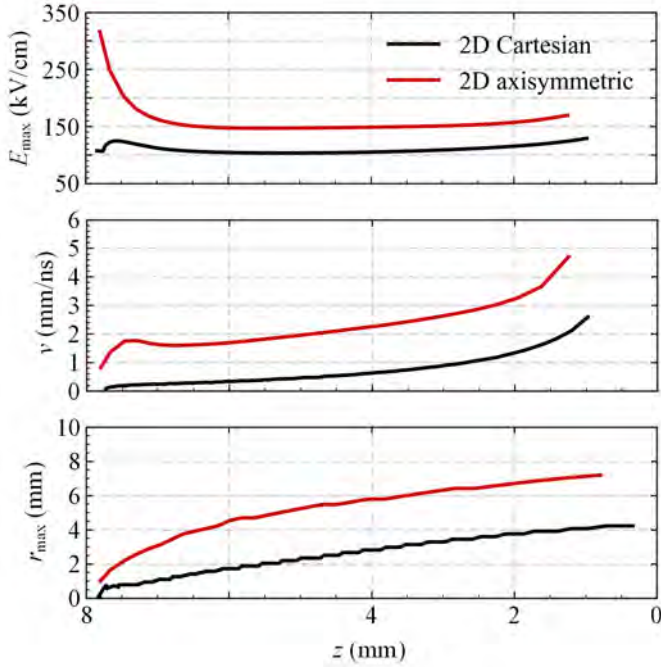


Figure 3.4: Comparison between 2D Cartesian and axisymmetric simulations for positive streamer discharges at an applied voltage of 25 kV. The streamer head position is determined by the  $y/r$ -coordinate of the maximal electric field. Here a second order Savitzky–Golay filter of width five is used to compute a smoothed velocity from the streamer head position versus time data.

Figure 3.5 and 3.6 shows the electron density, electric field and light emission for different applied voltages at the moment the streamer heads reach  $z = 2$  mm. In figure 3.5, the applied voltages are  $U_0 = 21, 22, 23, 24$  and 25 kV. With these voltages,  $U_0/U_{\text{inc}}$  ranges from 1.11 to 1.32 for the 2D Cartesian model and from 2.0 to 2.4 for the axisymmetric model. In figure 3.6, same results are used for the 2D Cartesian model, and axisymmetric results are shown at lower voltages of 12, 13, 14, 15, 16 kV, which correspond to  $U_0/U_{\text{inc}}$  ranging from 1.15 to 1.54. Figure 3.7 shows the axial electron density profiles for all these cases, streamer radius, velocity and maximal electric field versus position.

When the 2D Cartesian simulations at 21 kV–25 kV are compared with the axisymmetric simulations at the same voltage, the same large differences as in section 3.3.1 are observed. The axisymmetric streamer is two to four times wider, with the largest differences occurring near the electrode, and it is also two to four times faster. Furthermore, the maximal electric field  $E_{\text{max}}$  is about 50% higher in the axisymmetric case and the electron density in the channel is about two to three times higher, see figure 3.7.

When the 2D Cartesian simulations are compared with the axisymmetric simulations at lower voltages, the streamers have similar velocities. Their radii in the later stages of propagation are similar as well, although initially the 2D Cartesian streamers are much thinner. However, several other differences persist. For the axisymmetric streamers  $E_{\text{max}}$  is about 20–30% higher and the electron density in the channel is about 50–100% higher, see figure 3.7. Another important difference is in the decay of the electric field ahead of the streamer, which takes place over a longer distance in a 2D Cartesian geometry. This effect can clearly be seen in figure 3.6: the region with an electric field strength close to  $E_{\text{max}}$  is much smaller in the axisymmetric case. This can explain why the 2D Cartesian streamers tend to accelerate more rapidly when they approach the bottom electrode, as there is a larger region ahead of the discharge where the electric field exceeds the critical field.

### 3.3.4 Relation between streamer properties

For streamers in air, several (mostly empirical) relations between streamer properties such as velocity, radius and maximal electric field have been established, see e.g. [112, 9]. We now look at a couple of these relations to

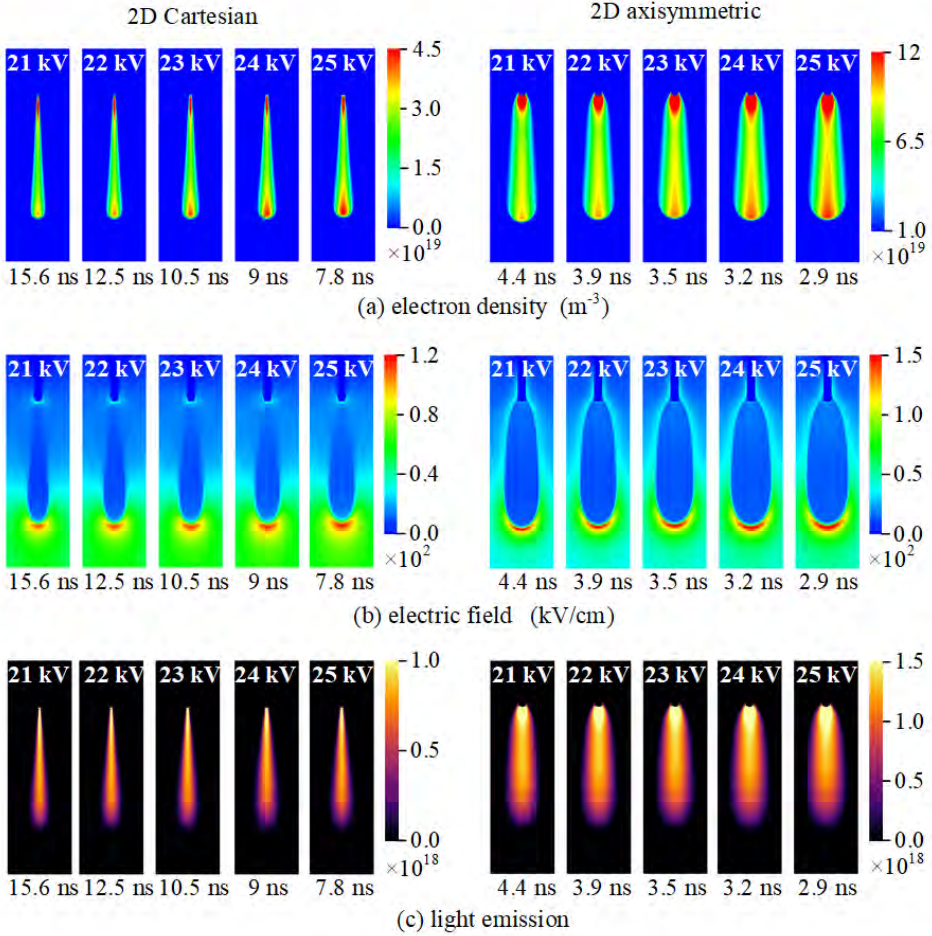


Figure 3.5: Comparison between 2D Cartesian and axisymmetric models using the same applied voltages. The presenting time is selected when the streamer tip reaches  $z = 2$  mm. The applied voltages are showed at the top of each plot and the time is at the bottom. Note that different color bars are used.

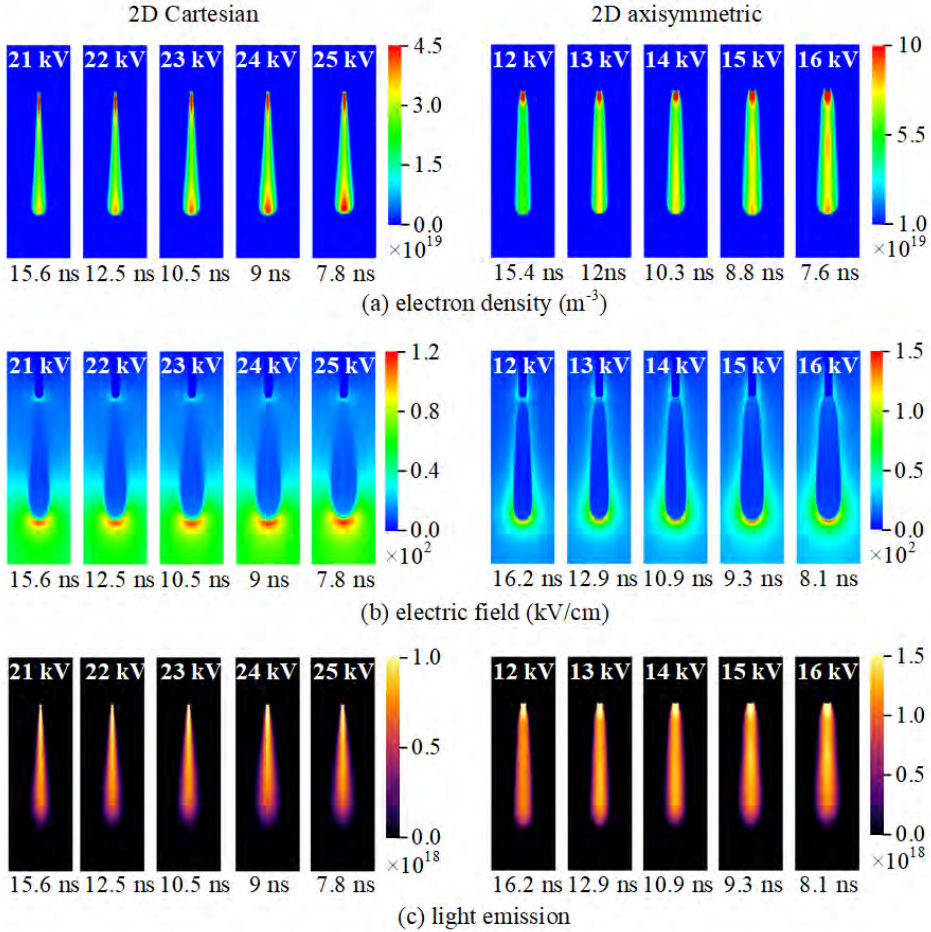


Figure 3.6: Comparison between 2D Cartesian and axisymmetric models using the voltages near the inception value. The presenting time is selected when the streamer tip reaches  $z = 2$  mm. The applied voltages are showed at the top of each plot and the time is at the bottom. Note that different color bars are used.



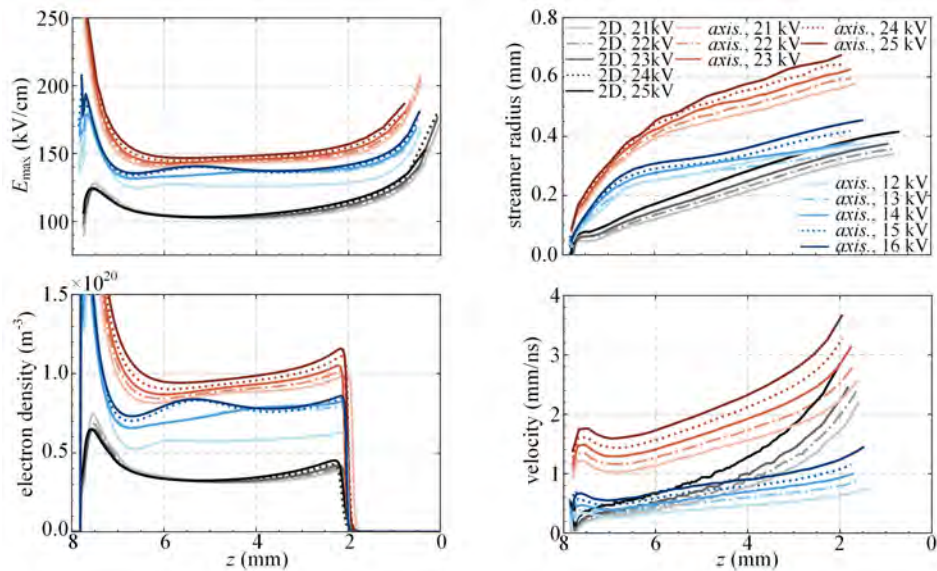


Figure 3.7: Streamer maximal electric field, radius and velocity versus the streamer head position, for all the cases shown in figure 3.5 and 3.6. The streamer head position is defined as the vertical coordinate of  $E_{\max}$ .

see whether they change in some particular way for planar (2D Cartesian) discharges.

Figure 3.8 shows the streamer radius versus velocity. When the applied voltage is near the inception value for both models (21–25 kV for the 2D Cartesian case and 12–16 kV for the axisymmetric case), the velocities increase approximately linearly with the streamer radii. When compared at the same streamer radius, the 2D Cartesian streamers typically have a higher velocity than the axisymmetric ones, but this is not surprising due to the difference in applied voltage.

Table 3.3 lists the electron density  $n_e$  in the streamer channel (just behind the streamer head) and the maximal electric field strength  $E_{\max}$  at the moment the streamers reach  $z = 4$  mm. These values are compared with the ionization integral [113, 114, 115]

$$n_{\alpha}(E_{\max}) = \frac{\varepsilon_0}{e} \int_0^{E_{\max}} \alpha_{\text{eff}}(E) dE, \quad (3.3)$$

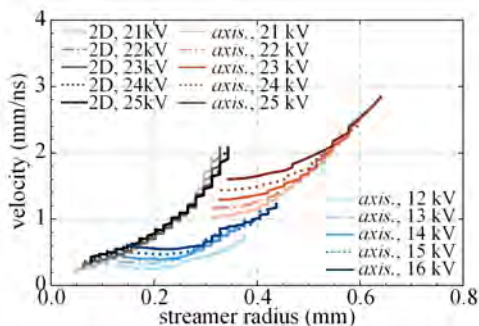


Figure 3.8: Streamer velocities  $v$  versus the maximal streamer radius  $r_{\max}$ . The streamer radius is defined based on the light emission, using FWHM method. The same color scheme is used here as in figure 3.7. The data are extracted when streamer head position is between  $z = 2 - 7$  mm.

and the ratio  $n_e/n_\alpha$  is given. This integral is accurate for one-dimensional ionization waves, in which the charge layers are not curved. In axisymmetric or 3D simulations of positive streamers it has been observed that the ratio  $n_e/n_\alpha$  is typically about two [116], which was recently related to the role of the displacement current [117]. We find the same ratio  $n_e/n_\alpha \approx 2$  for the 2D Cartesian case, even though this geometry lies ‘in between’ a planar 1D ionization wave and a 3D streamer. It is also interesting to note that  $E_{\max}$  is not sensitive to the applied voltage for voltages between 21 kV and 25 kV.

### 3.3.5 Discussion on streamer branching in 2D Cartesian model

Branching determines the morphology of a streamer discharge tree and it influences streamer properties, for example because wider channels are more likely to branch than thinner ones. In previous work [96], we have studied positive streamer branching in artificial air, using a 3D drift-diffusion-reaction fluid model coupled with stochastic photoionization, and we found good agreement with experimental observations. In earlier work, streamer branching has also been computationally studied in a 2D coaxial geometry [118]. An interesting question is therefore to what extent branching can qualitatively be described in a 2D Cartesian geometry.

Table 3.3: Degree of ionization  $n_e$ , maximal electric field  $E_{\max}$  and value of ionization integral  $n_\alpha$ , see equation (3.3). The values were obtained for the cases shown in figures 3.5– 3.7 when the streamers reached a vertical position  $z = 4$  mm.

	Voltage (kV)	$E_{\max}$ (kV/cm)	$n_e$ ( $10^{19} \text{ m}^{-3}$ )	$n_\alpha$ ( $10^{19} \text{ m}^{-3}$ )	$n_e/n_\alpha$ -
2D Cartesian	21	102.1	3.16	1.46	2.16
	22	102.6	3.18	1.49	2.14
	23	103.3	3.22	1.53	2.11
	24	104.3	3.29	1.58	2.08
	25	105.3	3.38	1.64	2.06
Axisymmetric	21	143.3	8.95	4.70	1.90
	22	144.5	9.12	4.83	1.89
	23	145.7	9.34	4.96	1.88
	24	147.1	9.57	5.11	1.87
	25	148.7	9.85	5.29	1.86
Axisymmetric	12	126.1	5.99	3.09	1.94
	13	136.8	7.97	4.05	1.97
	14	137.1	7.89	4.08	1.93
	15	136.2	7.93	3.99	1.99
	16	137.3	8.06	4.09	1.97

We expect branching to be significantly weaker in a 2D Cartesian geometry. A first difference is that charge layers are only curved in one dimension. This curvature drives the branching process through a Laplacian instability, since a protrusion can locally increase the electric field enhancement, see e.g. [119, 9]. In a 2D Cartesian geometry this instability will be significantly weaker. A second difference is that the electric field ahead of a 2D Cartesian streamer has a lower maximum but decays over a longer distance. This leads to less steep electron density gradients, and therefore a reduced probability of branching. A third difference is that higher applied voltages are required to initiate discharges in 2D Cartesian simulations. Streamer can usually grow wider, and thus branch later, with

a higher applied voltage.

To test these ideas, we have performed 2D Cartesian simulations with a Monte Carlo photoionization model. By limiting the maximum number of photons  $n_{\text{photon}}$  that are used to compute the photoionization source term (which is updated every time step), we can artificially increase the amount of noise and induce branching in this model. Figure 3.9 shows examples of 3D Cartesian simulations from our previous work and examples of branching streamers in 2D Cartesian simulations for different values of  $n_{\text{photon}}$ . The branching streamers in the 2D Cartesian simulations have a feather-like shape with many very thin branches, which is completely different from the morphology observed in the 3D simulations and in real discharges in air. This type of branching can only be induced for relatively small values of  $n_{\text{photon}}$ , showing that branching is suppressed rather strongly. We therefore conclude that 2D Cartesian models cannot qualitatively reproduce streamer branching.

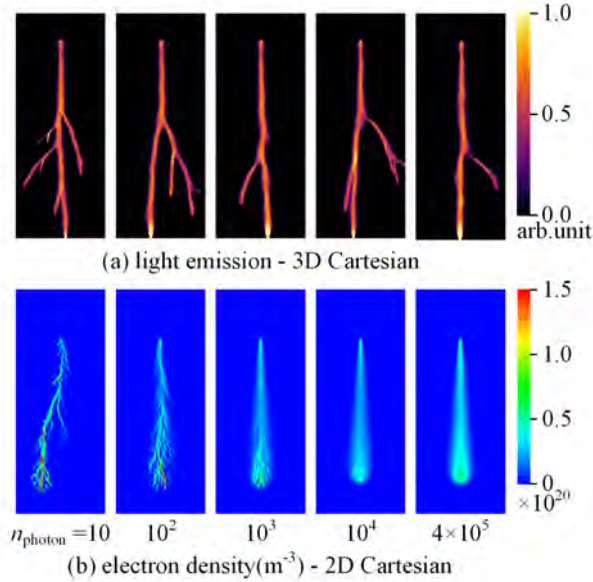


Figure 3.9: Examples of positive branching streamer in 2D Cartesian model and 3D Cartesian model. The stochastic photoionization is applied in both model to get streamer branching. 5 runs are showed for 3D Cartesian model under the same initial condition, see details in [96]. Different desired weight of super-photons  $n_{\text{photon}}$  are discussed in 2D Cartesian model, and one run is showed for each value of  $n_{\text{photon}}$ .

### 3.4 Conclusions

In this chapter, we have compared 2D Cartesian and 2D axisymmetric simulations of positive streamers. The simulations were performed in air at 1 bar and 300 K, using a drift-diffusion-reaction fluid model. An electrode of the same length and width was used in both geometries, corresponding to a needle in the axisymmetric case and a blade in the 2D Cartesian case. The applied voltage was varied to obtain background fields ranging from 12 kV/cm to 25 kV/cm.

When compared at the same applied voltage, the 2D Cartesian streamers were up to four times thinner and slower, with the largest differences occurring near the start of the discharge. Furthermore, their maximal elec-

tric field was about 30% lower and their degree of ionization was about 65% lower. These differences in streamer properties can to some extent be explained by differences in the respective inception voltages. For several electrode lengths and widths, we found inception voltages to be about twice as high in a 2D Cartesian geometry, due to the weaker electric field enhancement.

We therefore also performed a comparison at a similar ratio of applied voltage over inception voltage. Velocities then became rather similar in the two types of models, and so did the streamer radii at later propagation times. However, the maximal electric field in the 2D Cartesian case was still about 20-30% lower, and the degree of ionization was about 40-50% lower.

We have briefly looked at several relations between streamer properties, such as velocity, radius, maximal electric field and degree of ionization. Furthermore, we have show that streamer branching cannot qualitatively be reproduced in a 2D Cartesian simulations. Branching only occurs when strong noise is added to such simulations, and the resulting branches are much thinner than in real discharges in air.

Our findings can help to interpret the results of 2D Cartesian simulations, which can be a valuable tool to qualitatively study streamer phenomena under conditions that are computationally too expensive to simulate in full 3D.

## Chapter 4

# Quantitative modeling of streamer discharge branching in air

Streamer discharges are the primary mode of electric breakdown of air in lightning and high voltage technology. Streamer channels branch many times, which determines the developing tree-like discharge structure. Understanding these branched structures is for example important to describe streamer coronas in lightning research. We simulate branching of positive streamers in air using a 3D fluid model where photoionization is included as a discrete and stochastic process. The probability and morphology of branching are in good agreement with dedicated experiments. This demonstrates that photoionization indeed provides the noise that triggers branching, and we show that branching is remarkably sensitive to the amount of photoionization. Our comparison is therefore one of the first sensitive tests for Zheleznyak's photoionization model, confirming its validity.

This chapter is published as:

Z. Wang, S. Dijcks, Y. Guo, M. Van Der Leegte, A. Sun, U. Ebert, S. Nijdam, and J. Teunissen. Quantitative modeling of streamer discharge branching in air. *Plasma Sources Science and Technology*, 32(8):085007, 2023.



## 4.1 Introduction

Streamer discharges are the first stage of electric breakdown of air (or of other gases) when suddenly exposed to high electric fields [9]. They are elongated growing plasma channels; therefore their interior is largely screened from the electric field while the field is strongly enhanced at their propagating tips. Electron impact ionization in this enhanced field causes non-linear growth with velocities of  $10^5$ – $10^7$  m/s. Streamers are precursors of sparks and lightning leaders, they can be observed directly as sprites high above thunderclouds [94, 95, 10], and they play a prominent role in lightning inception [120, 121]. They are also widely used in plasma and high voltage technology [9, 91, 92, 93].

Branching is an integral part of streamer dynamics, as we illustrate with three examples. First, sprite discharges high above thunderstorms have been observed to start from a single channel shooting downwards from the lower edge of the ionosphere [94, 10]; this primary streamer discharge rapidly branches out into a multi-branch tree structure over tens of kilometers. Second, similar discharge trees are seen in experiments starting from needle electrodes; they are much smaller and occur at much higher pressure, and they are related to sprites by approximate scaling laws [122, 9]. Third, radio measurements of lightning initiation in thunderstorms are interpreted as “a volumetric system of streamers” growing over lengths of tens to hundred of meters [120]. Such dynamics has recently been observed in greater detail [121], where the radio emission of the initiating discharge grew exponentially in time while the velocity was fairly constant. As sketched in the outlook of [116], the explanation could be a dynamics where streamers accelerate and become wider, and branch whenever they reach a critical radius. As streamer velocity is related to radius, the streamers would then increase exponentially in number due to repetitive branching, but move with the same average velocity.

To understand these observations and to predict multi-streamer behavior by macroscopic breakdown models [123, 124], streamer branching needs to be characterized quantitatively. Experimental methods to measure streamer branching have been developed in [2, 125, 126, 127]. Here we present fully three-dimensional simulations based on tabulated microscopic parameters and compare them with dedicated experiments under the same

conditions. Our focus is on positive streamers as they emerge and propagate more easily than negative ones. They carry a positive head charge and propagate against the electron drift direction.

## 4.2 Photoionization and branching

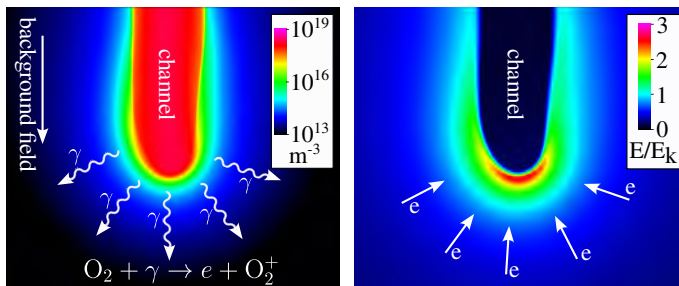


Figure 4.1: Cross sections through a positive streamer simulation at 15 kV. Left: electron density, with UV photons ( $\gamma$ ) schematically illustrated. Right: electric field strength, relative to breakdown field  $E_k$ . The drift of free electrons produced by photoionization is illustrated by arrows. These electrons trigger overlapping electron avalanches propagating towards the streamer head.

Positive streamers require seed electrons ahead of them, which in air are typically provided by photoionization [42, 128]: an excited nitrogen molecule emits a UV photon that ionizes an oxygen molecule at some distance. The liberated electrons generate electron avalanches in the high-field region in front of a streamer, which cause the streamer to grow, as illustrated in figure 4.1. The electron density ahead of the discharge affects the number of overlapping avalanches and thus the stochasticity of the streamer’s growth. It has been experimentally confirmed that there is more branching in gases with less photoionization and less background ionization, see e.g., [3, 129, 130].

That the stochasticity of photoionization triggers branching is also found in simulations in 2D [118], and in full 3D [37, 65, 90], while early 3D studies [131] worked with stochastic background ionization. Branching simu-

lated in [37, 65, 90] qualitatively resembled branching in experiments, but no quantitative comparison was performed – this is the goal of the present chapter.

In general, protrusions in the space charge layer around a streamer head can locally enhance the electric field, causing them to grow. This Laplacian destabilization can occur in a fully deterministic manner [132, 119], but it is accelerated by noise [133].

### 4.3 Set-up of experiments and simulations

To obtain a more quantitative understanding, we here compare streamer branching in simulations and experiments under the same conditions. The simulations and experiments are performed in synthetic air (80% N<sub>2</sub>, 20% O<sub>2</sub>, no humidity) at 233 mbar and approximately 300 K, under applied voltages of 15 kV, 17 kV and 19 kV, using the geometry illustrated in figure 4.2. Under these conditions, experiments with a moderate amount of branching could be performed, which could also be imaged well.

The experiments are performed with a pulse repetition rate of 20 Hz. Images are captured that are both stereoscopic and stroboscopic, as illustrated in figure 4.3. We use a similar stereoscopic setup as in [125]. In stroboscopic mode, the ICCD camera (LaVision PicoStar HR) has a gating time of 8 ns and a repetition rate of 50 MHz. From the captured images, 3D paths of streamers are reconstructed. This is done by connecting the bright dots, resulting from the stroboscopic gating, based on a shortest-path tree algorithm that can account for streamer branching. A quadratic extrapolation is used to smooth the streamer paths, from which branching angles and local velocities are obtained. More detailed information about this scheme can be found in [134].

Simulations are performed with a 3D drift-diffusion-reaction fluid model in which the only source of stochasticity is the discreteness of photoionization. We have recently established the approximate validity of this model for propagating streamers by comparing against experimental results [88] and particle simulations [56]. The model is described in detail in [40, 65, 88, 56], but we provide a brief overview below. The electron de

---

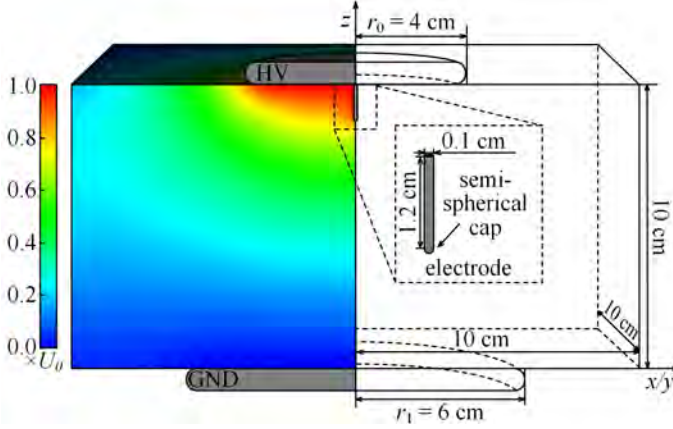


Figure 4.2: Electrode geometry both in simulations and experiments. The full computational domain is  $20\text{ cm} \times 20\text{ cm} \times 10\text{ cm}$ ; half of it is shown. There are plate electrodes at the upper and lower boundaries. The discharges start from a needle electrode that protrudes from the upper electrode. The electric potential distribution without space charge is shown on the left. In the experiments, the electrodes are inside a grounded discharge vessel. In the simulations, custom boundary conditions for the electric potential are used to account for this vessel, as described in [88].

nsity  $n_e$  evolves in time as

$$\partial_t n_e = \nabla \cdot (n_e \mu_e \mathbf{E} + D_e \nabla n_e) + S_i - S_a + S_p h, \quad (4.1)$$

where  $\mu_e$  and  $D_e$  are the electron mobility and the diffusion coefficient,  $S_p h$  is the non-local photoionization source term discussed below, and  $S_i - S_a$  is a source term due to the ionization ( $S_i$ ) and attachment ( $S_a$ ) reactions given in table 4.1.

Electron transport coefficients are assumed to be functions of the local electric field. They are computed from electron-neutral cross sections for  $\text{N}_2$  and  $\text{O}_2$  [85, 109] using BOLSIG+ [48, 49]. Ions and neutral species are assumed to be immobile, and their densities  $n_j$  (for  $j = 1, 2, \dots$ ) evolve as

$$\partial_t n_j = S_j, \quad (4.2)$$

with  $S_j$  determined by the reactions from table 4.1.

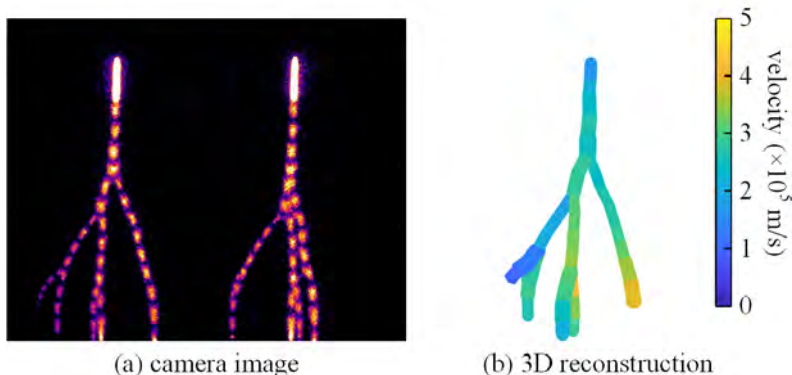


Figure 4.3: Example of 3D reconstruction of streamer paths and velocities in experiments, using stereoscopic stroboscopic images.

At every time step, the electric field is computed as  $\mathbf{E} = -\nabla\phi$ , where the electric potential  $\phi$  is obtained by solving Poisson's equation [40, 108]. For  $\text{N}_2\text{-O}_2$  mixtures close to atmospheric pressure, the  $\text{N}_2(\text{C}^3\Pi_u \rightarrow \text{B}^3\Pi_g)$  transition is the main source of emitted light [111]. In the simulations, we approximate the time-integrated light emission by the time integral over this transition.

For photoionization, a Monte-Carlo version of Zheleznyak's model [135] with discrete photons is used, as described in [46, 65]. The photo-ionization source term  $S_{\text{ph}}(r)$  is then given by

$$S_{\text{ph}}(\mathbf{r}) = \int \frac{I(\mathbf{r}')f(|\mathbf{r} - \mathbf{r}'|)}{4\pi |\mathbf{r} - \mathbf{r}'|^2} d^3\mathbf{r}', \quad (4.3)$$

where  $f(r)$  is the photon absorption function [135] and  $I(\mathbf{r})$  is the source of ionizing photons, which is proportional to the electron impact ionization source term  $S_i$ :

$$I(\mathbf{r}) = \frac{p_q}{p + p_q} \xi S_i. \quad (4.4)$$

Here  $p$  is the gas pressure,  $p_q = 40$  mbar is the quenching pressure and  $\xi$  a proportionality factor. In principle,  $\xi$  depends on the electric field [135], but we here for simplicity approximate it by a constant  $\xi = 0.075$  [65]. In each computational grid cell, the number of emitted photons is sampled

Table 4.1: Reactions included in the model. Rate coefficients for  $k_1$  to  $k_5$  were computed using BOLSIG+ [48, 49] from Phelps' cross sections [85, 109], and  $k_6$  to  $k_8$  were obtained from [1].

Reaction	Rate coefficient
$e + N_2 \xrightarrow{k_1} e + e + N_2^+$	$k_1(E/N)$
$e + O_2 \xrightarrow{k_2} e + e + O_2^+$	$k_2(E/N)$
$e + O_2 + O_2 \xrightarrow{k_3} O_2^- + O_2$	$k_3(E/N)$
$e + O_2 \xrightarrow{k_4} O^- + O$	$k_4(E/N)$
$e + N_2 \xrightarrow{k_5} e + N_2(C^3\Pi_u)$	$k_5(E/N)$
$N_2(C^3\Pi_u) + N_2 \xrightarrow{k_6} N_2 + N_2$	$k_6 = 0.13 \times 10^{-16} \text{ m}^3\text{s}^{-1}$
$N_2(C^3\Pi_u) + O_2 \xrightarrow{k_7} N_2 + O_2$	$k_7 = 3.0 \times 10^{-16} \text{ m}^3\text{s}^{-1}$
$N_2(C^3\Pi_u) \xrightarrow{k_8} N_2(B^3\Pi_g)$	$k_8 = 1/(42 \text{ ns})$

from a Poisson distribution with the mean given by  $I(\mathbf{r})\Delta t\Delta V$ , where  $\Delta t$  is the time step and  $\Delta V$  is the volume of the cell. For each ionizing photon, an isotropic angle and an absorption distance (according to Zheleznyak *et al.* [135]) are sampled. The photons are then absorbed on the numerical grid to determine the photoionization source term  $S_p h$ .

In the experiments, the voltage rise time was about 100 ns, but inception would typically occur with a delay of several hundred ns, when the voltage had already reached its maximum. To ensure a significant probability of inception, a voltage pulse width and a camera gate time of 1  $\mu\text{s}$  were used. In the simulations, we therefore do not take the voltage rise time into account, but instead apply a constant voltage from time zero. A homogeneous background ionization density of  $10^{11} \text{ m}^{-3}$  of electrons and positive ions is included to facilitate discharge inception. This density has no significant effect on the later discharge propagation since photoionization produces ionization densities that are orders of magnitude higher [89], as also illustrated in Appendix B.2.

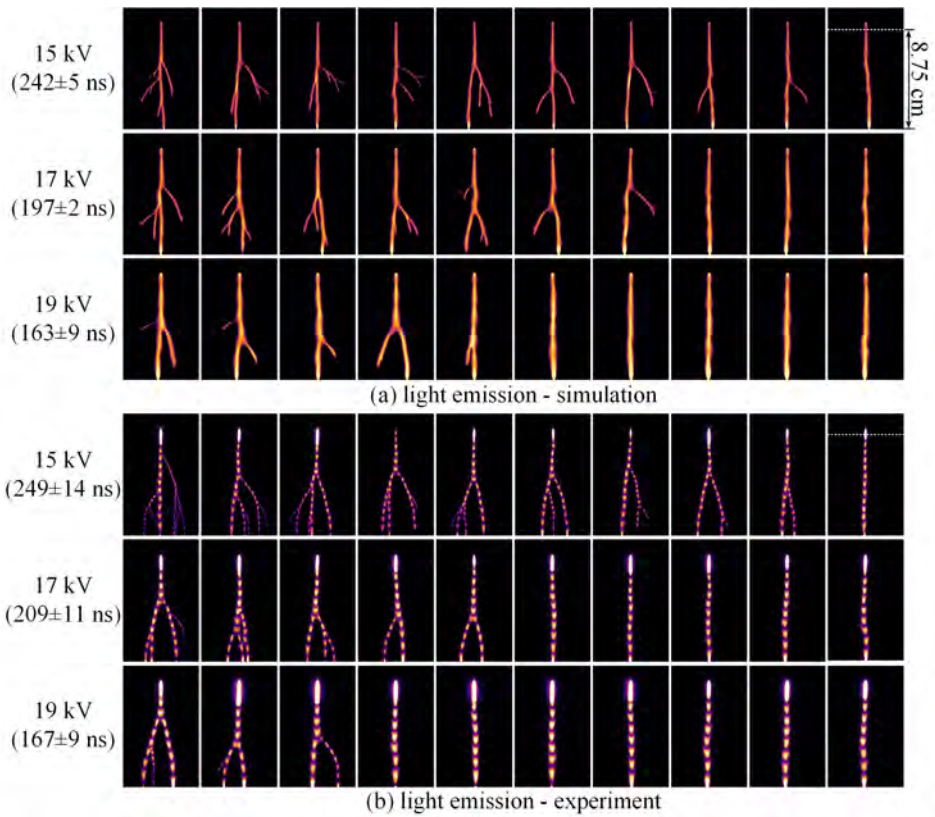


Figure 4.4: Comparison of streamer branching morphologies under applied voltages of 15, 17 and 19 kV, all at 233 mbar. For each voltage 60 simulations and 128 experiments were performed, and the 10 figures shown for each case are representative for the distribution given in table 4.2, with branched cases on the left. The simulations were stopped when the primary streamer reached the bottom electrode. In the experiments, a bright area is visible near the upper needle electrode due to a secondary streamer. Average times for crossing the last 8.75 cm of the gap are indicated on the left, together with standard deviations.

## 4.4 Results

For each applied voltage, 60 3D simulations were performed and 128 experimental images were captured. Figures 4.4(a) and 4.4(b) show ten representative examples from simulations and experiments for each voltage. The number of (non-)branching cases shown is proportional to the measured branching percentages as given in table 4.2.

Table 4.2: The number of cases with and without branching versus applied voltage. For the branching percentages, an estimate of the standard deviation due to the limited sample size is included. Cases without inception are excluded from the branching statistics.

		15 kV	17 kV	19 kV
Sim.	Branched	55	46	30
	Non-branched	5	14	30
	Branched %	$92 \pm 4\%$	$77 \pm 5\%$	$50 \pm 6\%$
Exp.	Branched	34	60	40
	Non-branched	2	54	78
	No inception	92	14	10
	Branched %	$94 \pm 4\%$	$53 \pm 5\%$	$34 \pm 4\%$

The morphology of the simulated and experimental discharges is highly similar. The branching angles, the location of first branching, and the streamer optical radii all agree well. The percentage of cases in which the primary streamer branches differs up to a factor of about 1.5 between experiments and simulations, but we argue below that this is still very good agreement given the sensitivity of this percentage to the photoionization coefficients. The average time it takes streamers to cross the last 8.75 cm of the gap is indicated in figure 4.4. These gap bridging times agree within about 5% between simulations and experiments, and in both cases they were similar for branched and non-branched cases. Streamer velocities ranged from about 0.3 mm/ns to 0.6 mm/ns, with average velocities in the second half of the gap being about 20-25% higher than in the first half.

Figure 4.5 shows the distribution of branching angles, measured between the two new segments. The mean branching angle was  $60^\circ$  in the



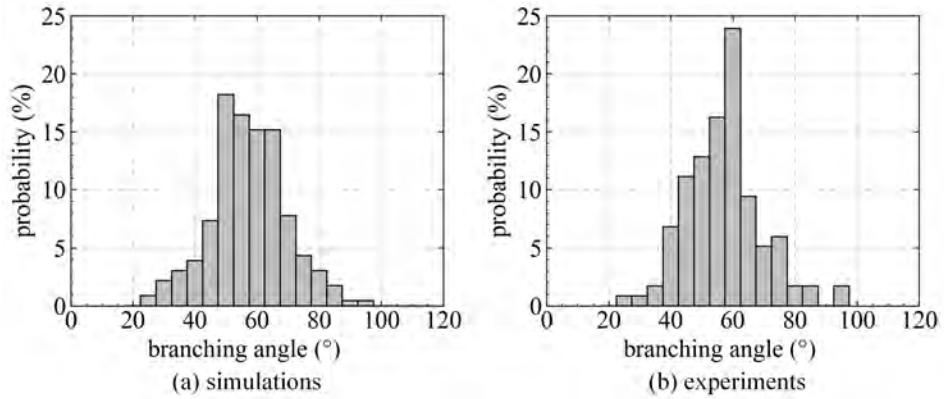


Figure 4.5: Probability distribution of the angle between two new segments after branching.

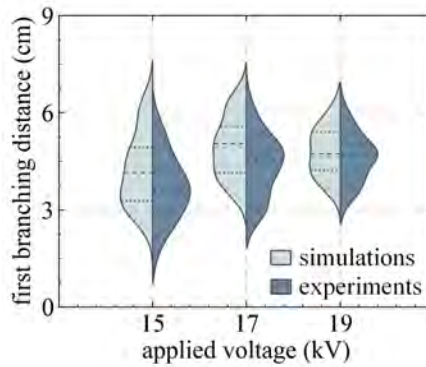


Figure 4.6: Distributions of the distance until a first branching, as measured from the electrode tip. The horizontal dashed lines indicate quartiles. A kernel density estimation of the underlying data is also shown. (The area between quartiles is not conserved due to smoothing.)

simulations and  $58^\circ$  in the experiments, with respective standard deviations of  $16.1^\circ$  and  $12.0^\circ$ . The distribution of the first branching location is shown in figure 4.6.

As the applied voltage increases, the percentage of cases in which the primary streamer branches decreases. The reason for this is that more

Table 4.3: The sensitivity of streamer branching to the photoionization coefficient  $\xi$  in equation (4.4). The simulations were performed at 17 kV.  $N_{\text{branchings}}$  denotes the average number of branching events. Experimental values are included for comparison.

$\xi$	0.0375	0.075	0.15	Exp.
Branched %	85%	77%	5%	53%
$N_{\text{branchings}}$	7.30	1.40	0.05	0.92

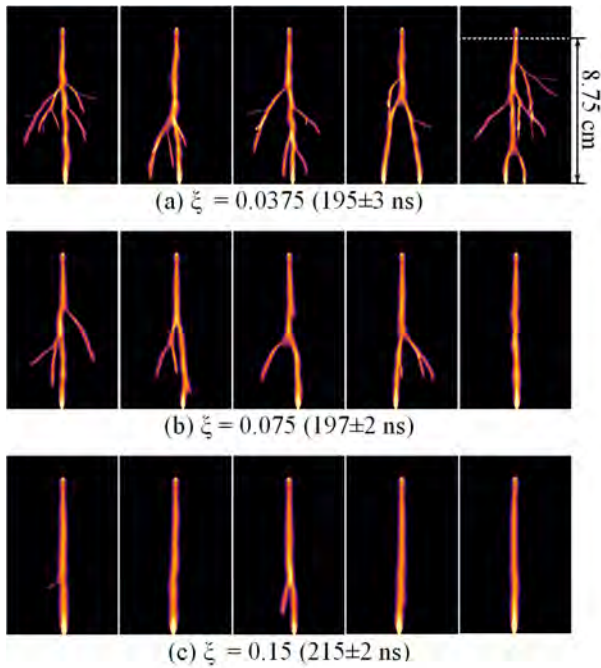


Figure 4.7: Representative simulations of streamer branching for different photoionization coefficients  $\xi$ . The value of  $\xi$  for each row is given on the left, and the value used elsewhere in the chapter is  $\xi = 0.075$ . The simulations were performed at 17 kV. Experimental images at 17 kV are shown in figure 4.4.

ionization is produced at a higher voltage, and thus also more photoionization, which makes the growth of the streamer less stochastic. At 15 kV, the branching percentage is almost the same in experiments and simulations. At 17 kV and 19 kV, the branching percentage is about 1.5 times larger in the simulations. We consider this good quantitative agreement, since the branching probability in simulations is very sensitive to the photoionization coefficients. To demonstrate this sensitivity, we have varied the parameter  $\xi$  in equation (2.9), by setting it to half and double the value of  $\xi = 0.075$  used elsewhere in the chapter. The resulting branching statistics are described in table 4.3, and representative cases are shown in figure 4.7. When halving or doubling  $\xi$ , the branching behavior qualitatively and quantitatively disagrees with the experiments. In contrast, average streamer velocities (deduced from the gap bridging times in figure 4.7) are not sensitive to  $\xi$ . When  $\xi$  is halved, there is hardly any difference, and when  $\xi$  is doubled the velocity is about 10% lower.

Zheleznyak's photoionization model is a rather simple approximation of several photoionization mechanisms [128], in which the coefficient  $\xi$  is essentially a fitting parameter. In [42], it was pointed out that  $\xi$  can vary between about 0.02 and 0.2 in air, depending on the electric field strength and the experimental data used for the fit. Given these uncertainties, and given the sensitivity of the simulations with respect to  $\xi$ , we think the agreement between simulations and experiments is surprisingly good. We furthermore emphasize that the constant value  $\xi = 0.075$  used here was based on previous work [65] and not tuned in any way. Our results therefore suggest that Zheleznyak's model gives an accurate description of photoionization in air.

## 4.5 Conclusions

We have found quantitative agreement between simulations and experiments of positive streamer branching in air, from which we draw three main conclusions: First, we have demonstrated that photoionization is the main mechanism that governed the branching observed here, as this was the only source of stochastic fluctuations in the simulations. Second, our comparison is one of the first sensitive tests for Zheleznyak's photoionization model, since the branching probability was shown to be very sensitive to the

photoionization coefficients, whereas other streamer properties like velocity are much less sensitive to these coefficients. Third, the presented validation of the model opens the opportunity to computationally study streamer branching. This is important for understanding the physical questions addressed in the introduction, in which branching plays a fundamental role in the discharge evolution.

## Chapter 5

# 3D simulations of positive streamers in air in a strong external magnetic field

We study how external magnetic fields from 0 to 40 T influence positive streamers in atmospheric pressure air, using 3D PIC-MCC (particle-in-cell, Monte Carlo collision) simulations. When a magnetic field  $\mathbf{B}$  is applied perpendicular to the background electric field  $\mathbf{E}$ , the streamers deflect towards the  $+\mathbf{B}$  and  $-\mathbf{B}$  direction which results in a branching into two main channels. With a stronger magnetic field the angle between the branches increases, and for the 40 T case the branches grow almost parallel to the magnetic field. Due to the  $\mathbf{E} \times \mathbf{B}$  drift of electrons we also observe a streamer deviation in the opposite  $-\mathbf{E} \times \mathbf{B}$  direction, where the minus sign appears because positive streamers propagate opposite to the electron drift velocity. The deviation due to this  $\mathbf{E} \times \mathbf{B}$  effect is smaller than the deviation parallel to  $\mathbf{B}$ . In both cases of  $\mathbf{B}$  perpendicular and parallel to  $\mathbf{E}$ , the streamer radius decreases with the magnetic field strength. We relate our observations to the effects of electric and magnetic fields on electron transport and reaction coefficients.

This chapter is available ahead of publishing as an electronic publication:  
Z. Wang, A. Sun, S. Dujko, J. Teunissen, and U. Ebert. 3D Simulations of  
positive streamers in air in a strong external magnetic field. arXiv:2309.02300  
[physics.plasm-ph], September 2023

## 5.1 Introduction

Streamer discharges are often the first stage in the electric breakdown of gases [9]. They are ionized channels that rapidly grow due to strong enhancement of the electric field at their tips; this high local field causes electron impact ionization which lets the plasma channel grow. In air, the growth of positive streamers against the electron drift direction is supported by nonlocal photoionization near regions of high impact ionization. The ionized paths created by streamers can later turn into sparks and lightning leaders, through Ohmic heating and gas expansion. A streamer corona paves the way of lightning leaders, and streamers are directly visible as huge sprite discharges below the ionosphere [136, 29]. Streamers also play a role in technological applications, such as plasma medicine [137], and plasma assisted combustion [21].

Magnetic fields play an important role for many types of discharges and plasmas, but for streamer discharges magnetic effects are usually not considered. The magnetization of electrons can be expressed by the Hall parameter  $\beta_{\text{Hall}} = \omega_{ce}/\nu$ , where  $\omega_{ce} = eB/m_e$  is the electron gyrofrequency in the magnetic field strength  $B$ ,  $\nu$  is the electron-neutral collision frequency,  $e$  is the elementary charge and  $m_e$  is the electron mass, see e.g. [138]. In other words, the Hall parameter determines over which angle the electrons spiral on average around a magnetic field line, before a collision with an air molecule randomizes their propagation direction. Electrons contributing to the growth of a streamer discharge typically have a high energy (of multiple eV), and therefore a high collision frequency. For example, in air at standard conditions the electron collision frequency in an electric field of 3 MV/m (which is approximately the breakdown field) is  $\nu \sim 3 \times 10^{12} \text{ s}^{-1}$ . A substantial effect of a magnetic field can be expected when  $\beta_{\text{Hall}} \sim 1$ , see e.g. [29, 35], which would require  $B \sim 17 \text{ T}$ . The magnetic fields induced by the currents inside a streamer are generally many order of magnitude weaker, as discussed in section 5.1 of [9]. Significant magnetic effects can therefore only come from an external magnetic field.

We remark that an estimate for the maximal magnetic field strength  $B_{\text{max}}$  induced by a streamer is given in section 5.1 of [9]:

$$B_{\text{max}} \approx vE_{\text{max}}/c^2, \quad (5.1)$$

where  $v$  is the streamer velocity,  $E_{\text{max}}$  the maximal electric field at the

streamer head and  $c$  the speed of light. This approximation is valid regardless of the gas number density.

Since  $\nu$  is proportional to the gas number density  $N$  (with small corrections due to three-body processes), the Hall parameter depends on the reduced magnetic field  $B/N$ . Ness proposed the Huxley as a unit of  $B/N$  ( $1 \text{ Hx} = 10^{-27} \text{ T m}^3$ ) that is commonly utilized in swarm studies of electron transport in electric and magnetic fields [139]. This scaling with gas density is similar to the dependence of (reduced) electron transport coefficients on the reduced electric field  $E/N$  [140, 29]. A streamer at ground pressure in an electric field of 1.5 MV/m and in a magnetic field of 10 T therefore scales approximately to a sprite streamer at 83 km altitude, hence in an air density of  $N = 10^{-5} N_{\text{ground}}$ , in an electric field of 15 V/m and in a magnetic field of 100  $\mu\text{T}$ . As discussed in [141, 29], the geomagnetic field at the equator is weaker (about 30  $\mu\text{T}$ ), which is why sprites on earth are not seen to be magnetized. (The geomagnetic field rises to about 60  $\mu\text{T}$  near the poles at sprite altitude, but there the field direction is vertical, and lightning and sprites are rare.) However, on Jupiter streamer discharges in sprites and lightning could be magnetized in the strong and irregular magnetic field of that planet [142, 143, 144, 145].

There have only been a few experimental studies on streamers in magnetic fields, as it is challenging to obtain a strong enough magnetic field in a sufficiently large volume. In [32] the early stages of magnetized streamers were studied in 99.9%-pure nitrogen at pressures of 0.27 to 0.8 bar, using a magnetic field strength of up to 12.5 T. For negative streamers a clear bending in the  $\mathbf{E} \times \mathbf{B}$  direction was observed, as expected for electrons drifting in a crossed electric field  $\mathbf{E}$  and magnetic field  $\mathbf{B}$ , but for positive streamers, the experimental results were more difficult to interpret. In earlier work, the effect of a magnetic field on surface discharges has also been studied using the Lichtenberg technique [33, 34]. In these studies, a clear bending of negative discharges was also observed, whereas positive streamers showed a smaller deviation.

Recently, the effect of an external magnetic field on streamer discharges has been investigated in two computational studies [35, 36] in which the magnetic field was assumed to be parallel to the background electric field. In [35], a 2D axisymmetric model was used to simulate both positive and negative streamers in an external parallel magnetic field. A decrease of



streamer radius was observed for both streamer polarities. The authors attributed this ‘self-focusing’ phenomenon to a sharp slowdown in the radial growth of the streamers. The same phenomenon was recently also observed in [36], in which the effects of Jupiter’s strong magnetic field (from 0.2 to 1.5 mT) on streamer inception and propagation were studied.

In this chapter, we generalize the above computational studies by also considering perpendicular magnetic fields, using 3D particle-in-cell simulations. In order to explain the main propagation phenomena of streamers, electron transport data in electric and magnetic fields crossed at arbitrary angle are also presented. We focus on positive streamers in air at 1 bar, and on magnetic field strengths of up to 40 Tesla. However, our results can be scaled to different pressures and corresponding field strengths, as discussed above.

We use a PIC-MCC (particle-in-cell, Monte-Carlo Collision) model, which combines the particle model described in [37] with the Afivo AMR (adaptive mesh refinement) framework described in [41]. In this model, only free electrons are tracked as particles, ions are tracked as densities, and neutral gas molecules are included as a background that electrons stochastically collide with. We use Phelps’ cross sections for  $N_2$  and  $O_2$  [85, 109]. To use them in particle simulations, we assume isotropic electron scattering and convert the effective momentum transfer cross-sections to elastic momentum transfer cross sections by subtracting the sum of the inelastic cross sections [86].

An advantage of a PIC-MCC model is that a magnetic field can relatively easily be included by modifying the particle mover, see section 5.1. To include a magnetic field in a fluid model is more complicated, since both the computation of transport data and the inclusion of such data into the model are non-trivial, see e.g. [30, 31].

## **Photoionization.**

Zhelenyak’s photoionization model [135] is included as a stochastic process, as described in [146, 37]. We briefly summarize the Monte Carlo method below. When a simulated electron with a weight  $w$  ionizes a neutral molecule, the number of ionizing photons that is generated is sampled

from the Poisson distribution with mean

$$n_{\text{photons}} = \frac{p_q}{p + p_q} \xi w, \quad (5.2)$$

where  $p$  is the gas pressure,  $p_q = 40$  mbar is the quenching pressure, and  $\xi = 0.075$  is a proportionality factor that we assume to be constant for simplicity. Note that the photons thus have a weight of one. For each photon, an absorption length is sampled from the absorption function

$$f(r) = \frac{\exp(-\chi_{\min} p_{O_2} r) - \exp(-\chi_{\max} p_{O_2} r)}{r \ln(\chi_{\max}/\chi_{\min})}, \quad (5.3)$$

as described in [146, 37]. Here  $\chi_{\max} = 1.5 \times 10^2 / (\text{mm bar})$ ,  $\chi_{\min} = 2.6 / (\text{mm bar})$ , and  $p_{O_2}$  is the partial pressure of oxygen. An isotropic direction is then sampled, after which an ionization event of  $O_2$  is generated at the location of absorption if this location is inside the gas region of the computational domain.

### Super-particles.

So-called super-particles [82] are used to speed up the simulations and save memory. The weight parameter  $w_i$  determines how many physical particles the  $i^{\text{th}}$  simulation particle represents. During a simulation, the weights  $w_i$  change over time by merging and splitting particles as described in [56]. Particle weights are updated when the number of simulation particles has grown by a factor of 1.25 or following a change of the AMR mesh (see section 5.1), so that they stay close to a desired weight  $w$  given by

$$w = n_e \times \Delta V / N_{ppc}, \quad (5.4)$$

where  $n_e$  is the electron density in a cell,  $\Delta V$  the cell volume and  $N_{ppc}$  is the target number of simulation particles per cell, here set to  $N_{ppc} = 75$ .

### Particle mover.

We use Boris' rotation method [147] to advance the position and velocity of electrons in time. The timestep in our simulations is limited by several restrictions

$$\Delta t \leq \min(0.5 \times \Delta x_{\min} / \tilde{v}_{\max}, \Delta t_{\text{drt}}, 0.1 \times 2\pi / \omega_{ce}). \quad (5.5)$$

Here  $\Delta x_{\min}$  indicates the minimal grid spacing, and  $\tilde{v}_{\max}$  is an estimate of the particle velocity at the 90%-quantile.  $\Delta t_{\text{drt}}$  is the Maxwell time, also known as the dielectric relaxation time, which is a typical time scale for electric screening. Finally, the last criterion ensures that the gyration of electrons is accurately resolved.

### Adaptive mesh refinement.

Adaptive mesh refinement (AMR) is used for both computational efficiency and computational accuracy. The mesh is refined based on the following criteria [40]:

- refine if  $\alpha(E)\Delta x > 1.0$ ,
- de-refine if  $\alpha(E)\Delta x < 0.125$ , but only if  $\Delta x$  is smaller than 10  $\mu\text{m}$ .

Here  $\alpha(E)$  is the field-dependent ionization coefficient, and  $\Delta x$  is the grid spacing, which is bound by  $2 \mu\text{m} \leq \Delta x \leq 0.4 \text{ mm}$ .

### 5.1.1 Computational domain and simulation conditions

Simulations are performed in artificial air, containing 80%  $\text{N}_2$  and 20%  $\text{O}_2$ , at  $p = 1 \text{ bar}$  and  $T = 300 \text{ K}$ . Figure 5.1 shows a cross section of the  $20 \text{ mm} \times 20 \text{ mm} \times 10 \text{ mm}$  computational domain. A rod-shaped electrode with a semi-spherical cap is placed at the center of the domain [148]. This electrode is 2 mm long and has a radius of 0.2 mm. Boundary conditions for the electric potential are given in the caption of figure 5.1. In our computational domain, the background electric field points in the  $-z$  direction, and a magnetic field is applied in either the  $-z$  direction (parallel case) or in the  $-x$  direction (perpendicular case).

There is initially no background ionization besides an electrically neutral plasma seed, which is placed at the tip of the electrode to provide initial ionization. Electrons and positive ions are generated by sampling from a Gaussian distribution

$$n_i(\mathbf{r}) = n_e(\mathbf{r}) = 10^{16} \text{ m}^{-3} \exp \left[ \frac{-|\mathbf{r} - \mathbf{r}_0|^2}{(0.1 \text{ mm})^2} \right], \quad (5.6)$$

where  $\mathbf{r}_0$  is the location of the tip of the electrode, given by  $(x, y, z) = (10, 10, 7.8) \text{ mm}$ .

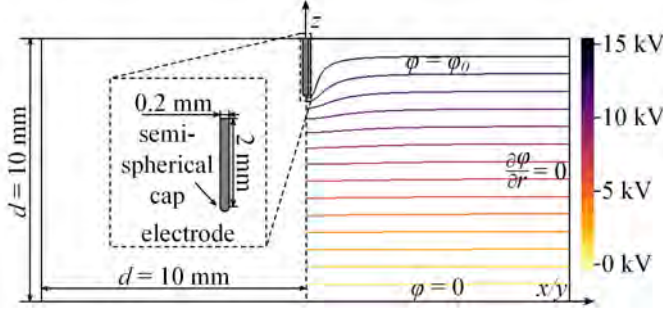


Figure 5.1: Cross section of the 3D computational domain, which measures  $20 \text{ mm} \times 20 \text{ mm} \times 10 \text{ mm}$ . The electric potential  $\varphi$  (in the absence of a discharge) and the electrode geometry are shown. A voltage of  $\varphi_0 = 15 \text{ kV}$  is applied at the top of the domain and the needle electrode. The bottom of the domain is grounded ( $\varphi = 0$ ), and at the sides a Neumann zero boundary condition is used for  $\varphi$ .

### 5.1.2 Effect of magnetic field on electron drift and ionization

To understand the behavior of streamer discharges in  $\mathbf{E}$  and  $\mathbf{B}$  fields, it helps to know how free electrons behave in these fields. We have therefore computed electron transport coefficients for homogeneous  $\mathbf{E}$  and  $\mathbf{B}$  fields at an arbitrary angle with a Monte Carlo swarm code [https://github.com/MD-CWI/particle\\_swarm](https://github.com/MD-CWI/particle_swarm). Data computed for background electric fields of  $150 \text{ kV/cm}$  and  $15 \text{ kV/cm}$  and for magnetic fields between  $0$  and  $40 \text{ T}$  are shown in figure 5.2 as a function of the angle between  $\mathbf{E}$  and  $\mathbf{B}$ . The Hall parameter  $\beta_{\text{Hall}}$  for the ensemble of electrons is also indicated. In this case, we define  $\beta_{\text{Hall}} = \omega_{ce}/\bar{\nu}$  where  $\bar{\nu}$  is the average electron collision frequency [149].

For the analysis of electron motion, we decompose the electric field into a part parallel and perpendicular to  $\mathbf{B}$  as  $\mathbf{E} = \mathbf{E}_{\parallel} + \mathbf{E}_{\perp}$ . Then three components of the electron mobility can be distinguished:

$$\mu_{\parallel} = v_{\parallel}/E_{\parallel} = |\mathbf{v} \cdot \hat{\mathbf{E}}_{\parallel}|/E_{\parallel}, \quad (5.7)$$

$$\mu_{\perp} = v_{\perp}/E_{\perp} = |\mathbf{v} \cdot \hat{\mathbf{E}}_{\perp}|/E_{\perp}, \quad (5.8)$$

$$\mu_{\times} = v_{\times}/E_{\perp} = |\mathbf{v} \cdot (\hat{\mathbf{E}}_{\perp} \times \hat{\mathbf{B}})|/E_{\perp}, \quad (5.9)$$

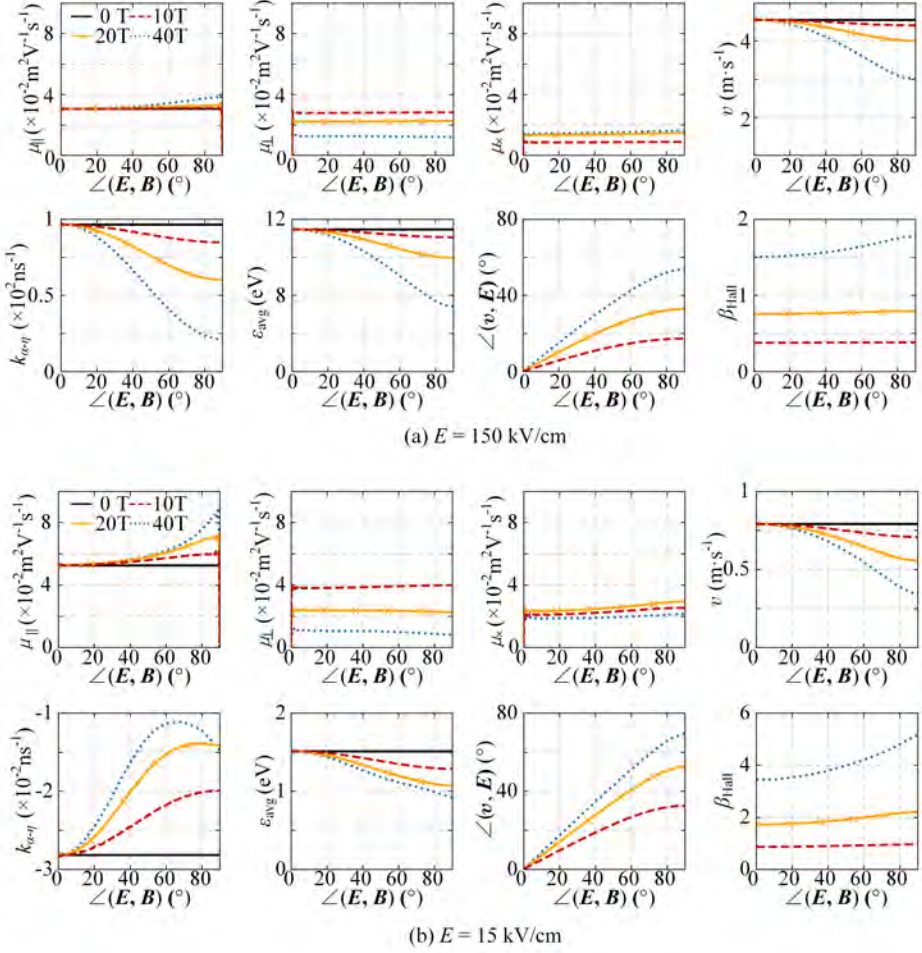


Figure 5.2: Electron transport coefficients in homogeneous  $\mathbf{E}$  and  $\mathbf{B}$  fields as a function of the angle  $\angle(\mathbf{E}, \mathbf{B})$  between the fields. The data was generated (a) for a typical maximal field at the streamer head of  $E = 150 \text{ kV/cm}$  and (b) for half the breakdown field  $E = 15 \text{ kV/cm}$ , and for magnetic fields of  $B = 0, 10, 20, 40 \text{ T}$ , in synthetic air at 1 bar and 300 K. Here  $\mu_{\parallel}$  and  $\mu_{\perp}$  are the flux mobility components parallel and perpendicular to  $\mathbf{B}$ , and  $\mu_{\times}$  is a flux mobility component in the  $\mathbf{E} \times \mathbf{B}$  direction, see section 5.1.2.  $v$  is the electron drift velocity,  $k_{\alpha-\eta}$  is the effective ionization rate (positive for  $E = 150 \text{ kV/cm}$  and negative for  $E = 15 \text{ kV/cm}$ ), and  $\epsilon_{\text{avg}}$  is the mean electron energy.  $\angle(\mathbf{v}, \mathbf{E})$  is the angle between the electron drift velocity  $\mathbf{v}$  and  $\mathbf{E}$ , and  $\beta_{\text{Hall}}$  is the Hall parameter for the ensemble of electrons, see section 5.1.2

where  $\mathbf{v}$  is the electron drift velocity, and  $\mu_{\parallel}$ ,  $\mu_{\perp}$  and  $\mu_{\times}$  are respectively the mobility parallel to the magnetic field, the mobility perpendicular to the magnetic field (but parallel to  $\mathbf{E}_{\perp}$ ), and the “mobility” in the  $\mathbf{E} \times \mathbf{B}$  direction. Here  $\hat{\mathbf{E}}$  and  $\hat{\mathbf{B}}$  denote unit vectors in the direction of the  $\mathbf{E}$  and  $\mathbf{B}$  respectively. Note that  $E_{\parallel} = E \cos(\theta)$  and  $E_{\perp} = E \sin(\theta)$ , where  $\theta = \angle(\mathbf{E}, \mathbf{B})$  is the angle between  $\mathbf{E}$  and  $\mathbf{B}$ . Furthermore we remark that equations (5.7–5.9) define so-called flux mobilities, see e.g. [150].

A clear effect of a stronger magnetic field is that  $\mu_{\perp}$  is reduced. The reduction in  $\mu_{\perp}$  leads to a lower mean electron energy and a smaller ionization coefficient when the angle between  $\mathbf{E}$  and  $\mathbf{B}$  increases, because the energy electrons on average gain per unit time from the electric field is given by  $e\mu_{\parallel}E_{\parallel}^2 + e\mu_{\perp}E_{\perp}^2$ . For  $\mathbf{B} = 40$  T, the ionization rate is reduced by almost 80% when  $\mathbf{E}$  and  $\mathbf{B}$  are perpendicular. The reduction in mean electron energy is also related to an increase in the parallel electron mobility  $\mu_{\parallel}$ , since electron mobilities are typically higher at lower electron energies.

The magnitude of the  $\mathbf{E} \times \mathbf{B}$  drift, here denoted by

$$v_{\times} = \mu_{\times} E_{\perp} = \mu_{\times} E \sin(\theta), \quad (5.10)$$

depends on the magnetization of electrons and on the respective fields. In the absence of collisions

$$v_{\times} = |\mathbf{E} \times \mathbf{B}|/B^2 = E \sin(\theta)/B, \quad (5.11)$$

so that a stronger magnetic field leads to a smaller  $v_{\times}$ . However, when collisions are included a lower magnetic field will lead to a lower magnetization (i.e., Hall parameter  $\beta_{\text{Hall}}$ ), with  $v_{\times} \rightarrow 0$  for  $\beta_{\text{Hall}} \rightarrow 0$ . For a given electric field,  $v_{\times}$  will thus first increase with the magnetic field strength and then decrease, as can be seen from the  $\mu_{\times}$  plot in figure 5.2b.

With a magnetic field the mobilities are  $\mu_{\perp} < \mu_{\parallel}$  and  $\mu_{\times} > 0$ , which means that the electron drift velocity  $\mathbf{v}$  makes an angle with the electric field  $\mathbf{E}$ . This angle can be as large as  $70^{\circ}$  for the conditions considered here, as shown in figure 5.2.

Note that when the electric and the magnetic field are parallel electron transport and reaction coefficients (except for transverse diffusion coefficients) hardly depend on the magnetic field strength. In this case, the magnetic field does not affect the energy gain of electrons due to their acceleration parallel to  $\mathbf{E}$ .

## 5.2 Results & Discussion

### 5.2.1 3D simulations

We simulate positive streamers with an external magnetic field of 0, 10, 20 and 40 T. In these simulations, the background electric field  $E = 15$  kV/cm between the plate electrodes is about half of the breakdown field, and it points downwards in  $-z$  direction, see Fig. 5.1. The magnetic field  $B$  either points in the same direction (parallel case) or in the  $-x$  direction (perpendicular case). In all cases, the positive streamers grow due to photoionization which produces free electrons ahead of them [9].

Results with a parallel magnetic field are shown in figure 5.3. In agreement with previous work [35, 36], the following main phenomena are observed:

- For a stronger magnetic field, the streamer diameter decreases and its velocity and the maximum electron density inside the channel increase.
- The streamer overall stays axisymmetric, if it started like this.

Results with a perpendicular magnetic field are shown in figure 5.4, and one particular run in a field of 20 T is magnified in figure 5.5. The main phenomena are:

- With growing magnetic field, the streamer diameter decreases and its velocity and the maximum electron density inside the channel decrease as well.
- The streamers deflect towards the  $+B$  and  $-B$  direction which results in a branching into two main channels. The angle between the branches increases with  $B$ . There seem to be two preferred streamer propagation directions in the plane spanned by  $E$  and  $B$ .
- The branched streamer does not completely lie in the plane spanned by  $E$  and  $B$ , but shows a slight deviation towards the  $-E \times B$  direction.

We will explain these phenomena below, making use of the electron transport data presented in section 5.1.2.

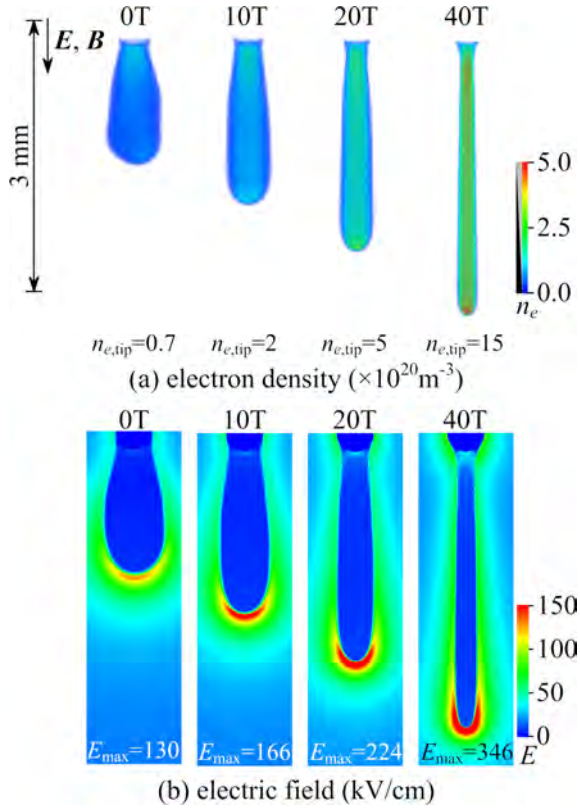


Figure 5.3: Simulations of positive streamers at  $t = 3$  ns in magnetic fields of 0, 10, 20 and 40 T that are parallel to a background electric field of 15kV/cm. (a) volume rendering of the electron density, (b) cross section of the electric field. For reference, the electron density behind the streamer tip ( $n_{e,\text{tip}}$ ) and the maximal electric field strength  $E_{\text{max}}$  are indicated in the panels.



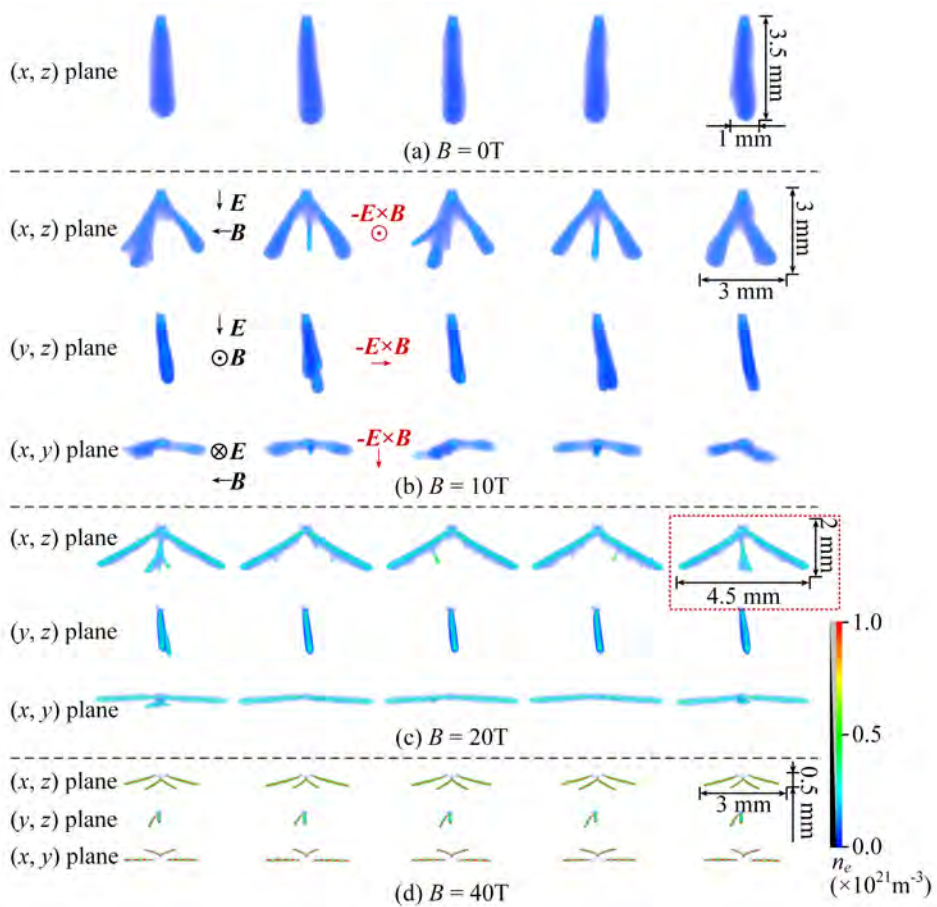


Figure 5.4: Simulations of positive streamers at  $t = 6$  ns in magnetic fields of 0, 10, 20 and 40 T that are perpendicular to a background electric field of 15 kV/cm. Electron densities are visualized using 3D volume rendering. Each row shows five runs in the same magnetic field to illustrate the stochasticity of the particle simulations. For  $B > 0$  several viewing angles are shown, with the plane that is viewed indicated on the left. The directions of  $\mathbf{E}$ ,  $\mathbf{B}$  and  $-\mathbf{E} \times \mathbf{B}$  are indicated in the  $B = 10$  T case, they are the same for the  $B = 20$  T and  $B = 40$  T cases. The simulation in the red dotted frame is shown in more detail in figure 5.5.

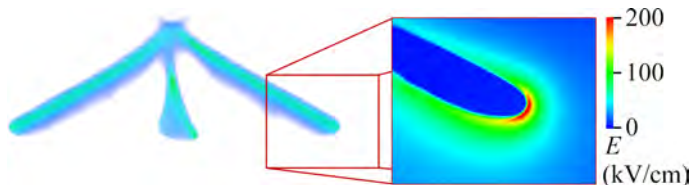


Figure 5.5: Left: Enlarged electron density in a magnetic field of  $B = 20$  T. Shown is the rightmost case from Fig. 5.4 viewed in the  $(x, z)$  plane (marked with a red dotted frame in that figure). Right: Further enlarged cross section of the electric field  $E$ .

## 5.2.2 Branching in a perpendicular field

With a perpendicular  $\mathbf{B}$ -field of 20 T to 40 T positive streamers typically split into two main channels, which both lie approximately in the plane spanned by  $\mathbf{E}$  and  $\mathbf{B}$ . The angle between the branches grows with the magnetic field, until the branches are almost parallel or antiparallel to  $\mathbf{B}$ . The two main channels are quite symmetric in the plane spanned by  $\mathbf{E}$  and  $\mathbf{B}$ , because changing  $\mathbf{B}$  into  $-\mathbf{B}$  only changes the chirality of the gyration about the magnetic field line; the electrons on the left branch therefore have chirality opposite to those on the right branch, but otherwise the same energy distributions, ionization rates etc. With a perpendicular  $\mathbf{B}$ -field of only 10 T, the branching appears to be more stochastic, with a smaller angle between the branches and sometimes a third branch. We remark that stochastic streamer branching is a common phenomenon in streamer discharges without a magnetic field, in which stochastic fluctuations can trigger a Laplacian instability, see e.g. [151, 152, 96]. The peculiar aspect of the branching observed here is that it is not (or hardly) stochastic, but that it is rather induced by the two preferred propagation directions.

While the direction of the primary streamers in higher magnetic fields is clearly determined by magnetic and electric fields (and possibly by the streamer radius), the shorter secondary branches that form at a later time propagate in an electric field modified by the primary streamers. Therefore they deviate from the direction of the primary streamers.

A perpendicular magnetic field can contribute to streamer branching in two ways. The first is related to the ionization rate. Without a magnetic

field, the ionization rate depends only on the electric field strength, which is highest in the forward direction. However, with a magnetic field, the ionization rate will also depend on the angle with the magnetic field, as shown in figure 5.2. Since the strongest reduction in the ionization rate will occur for the lowest electron energies, i.e., when the electric field is perpendicular to  $\mathbf{B}$ , the maximum of the ionization rate can then lie at some intermediate angle between the background field  $\mathbf{E}$  and the magnetic field  $\mathbf{B}$ .

The second effect is on the screening inside the streamer channel. Perpendicular to  $\mathbf{B}$ , electric screening is slowed down due to the lower drift velocity, see figure 5.2. Since electron screening parallel to  $\mathbf{B}$  is not affected (the parallel mobility can even increase, as shown in figure 5.2), there will be stronger field enhancement parallel to  $\mathbf{B}$ . Both the change in ionization rate and the change in drift velocity will deform the streamer head, as shown in Fig. 5.5, and contribute to branching in the  $(\mathbf{E}, \mathbf{B})$ -plane.

Unlike ‘normal’ streamer branching [96], branching in a strong magnetic field is a rather deterministic process. The angle at which branches grow depends on the ‘competition’ between the magnetic field, which favors growth parallel or anti-parallel to it, and electric field enhancement, which is strongest parallel to the background electric field. A stronger magnetic field therefore leads to a larger branching angle.

### 5.2.3 Effect of magnetic field on streamer radius

Figure 5.3 shows that a parallel  $\mathbf{B}$ -field leads to a smaller streamer radius, consistent with the findings of [35, 36]. The underlying mechanism is a reduction in the radial growth of the streamer, which is perpendicular to the  $\mathbf{B}$ -field, due to a lower ionization rate, see figure 5.2. Since the forward growth is not affected, as it is parallel to the  $\mathbf{B}$ -field, the result is a smaller radius and stronger electric field enhancement.

Figure 5.4 shows that a perpendicular  $\mathbf{B}$ -field also leads to a reduction in streamer radius. We think there are two main mechanisms that play a role here. The first is that after the streamers branch, the magnetic field is partially aligned with their growth velocity. This parallel component of the magnetic field will have a similar effect as in the case where the electric and magnetic field are initially parallel, i.e., it will reduce the streamer radius. The second mechanism is that the ionization rate around the streamers is

reduced, since there is also a magnetic field component perpendicular to the streamer velocity. This reduced ionization rate will probably play a similar role as a weaker background field (or a lower applied voltage) does in cases without a magnetic field, namely the formation of thinner channels.

Note that although the effect of a magnetic field on the streamer radius is similar for the parallel and perpendicular configurations, the effect on the streamer velocity is different: a parallel magnetic field leads to a higher velocity, see figure 5.3, whereas a perpendicular magnetic field leads to a lower velocity, see figure 5.4.

### 5.2.4 Bending in $-\mathbf{E} \times \mathbf{B}$ direction

With a perpendicular magnetic field of 10 T and 20 T, the discharge channels bend slightly towards the  $-\mathbf{E} \times \mathbf{B}$  direction, as shown in figure 5.4. At 10 T the bending angle is about  $9^\circ$  and at 20 T it is about  $7^\circ$ . This bending is due to the  $\mathbf{E} \times \mathbf{B}$  drift of electrons, which leads to a deviation in the opposite direction ( $-\mathbf{E} \times \mathbf{B}$ ) since positive streamers propagate in the opposite direction of the electron drift velocity.

In figure 5.2 the angle the electron drift velocity makes with respect to  $\mathbf{E}$  is shown. When  $\mathbf{E}$  and  $\mathbf{B}$  are perpendicular, this angle ranges from about  $18^\circ$  (10 T, 150 kV/cm) to  $70^\circ$  (40 T, 15 kV/cm), due to the  $\mathbf{E} \times \mathbf{B}$  drift. These angles are considerably larger than the positive streamers' bending angle of up to about  $10^\circ$ , especially when comparing against the transport data in a lower background field of 15 kV/cm. We think there are several reasons for this. First of all, it should be noted that although the background electric field is perpendicular to  $\mathbf{B}$  in the simulations, the enhanced electric field near the streamer head will generally not be perpendicular to  $\mathbf{B}$ . Furthermore, streamers grow more parallel to  $\mathbf{B}$  as the magnetic field strength is increased, which reduces the magnitude of the  $\mathbf{E} \times \mathbf{B}$  drift and thus also the bending angle. This could explain why the observed bending is a bit smaller at 20 T than at 10 T, and why no clear bending can be observed at 40 T. A second reason is that the bending probably originates from the deformation of the streamer head, where the increased electron drift velocity increases electric field enhancement in the  $-\mathbf{E} \times \mathbf{B}$  direction. The high electric field at the streamer head will result in a smaller bending angle, as illustrated by figure 5.2. A third reason is that streamer growth depends on both the electron drift and the impact

ionization rate (which depends on the electron energy distribution). There is only an  $\mathbf{E} \times \mathbf{B}$  effect on the electron drift, in contrast to the branching mechanism discussed in section 5.2.2, where both the electron drift and the ionization rate depended on the angle with the magnetic field.

Finally, we remark that a side branch in the  $\mathbf{E} \times \mathbf{B}$  direction is visible in all cases at 40 T, which is probably caused by the effect the  $\mathbf{E} \times \mathbf{B}$  drift has on the initial seed.

### 5.2.5 Comparison with experimental work

As mentioned in the introduction, the effect of a strong magnetic field on positive and negative streamers in nitrogen has been experimentally studied in [32]. The discharges were observed in a plane perpendicular to  $\mathbf{B}$ , which means that only path deviations perpendicular to  $\mathbf{B}$  could be observed, and thus not the branching phenomenon found here in the  $\mathbf{E}, \mathbf{B}$ -plane. Negative streamers were found to clearly bend in the  $\mathbf{E} \times \mathbf{B}$  direction, and a rather small deviation of positive streamers in the  $-\mathbf{E} \times \mathbf{B}$  was observed. We remark that after switching the voltage polarity, the  $\mathbf{E} \times \mathbf{B}$  direction also flips, which means that in the experimental figures positive and negative streamers deviate in the same visual direction.

Earlier work used the Lichtenberg technique to study the effect of a magnetic field on surface discharges, with the magnetic field perpendicular to the surface. In [33], only negative discharges were observed, which showed a clear bending in the  $\mathbf{E} \times \mathbf{B}$  direction. In [34], both polarities were considered, and it was found that negative streamers had a significantly larger deflection angle than positive ones. As in [32], streamers with both polarities bended in the same visual direction, which means that negative streamers deviated in the  $\mathbf{E} \times \mathbf{B}$  and positive ones in the  $-\mathbf{E} \times \mathbf{B}$  direction, consistent with our findings.

## 5.3 Conclusions

We have simulated the propagation of positive streamers in atmospheric air in external magnetic fields ranging from 0 to 40 T using a 3D PIC-MCC model including photoionization. For magnetic fields perpendicular to the background electric field, streamers deflect towards the  $+\mathbf{B}$  and

$-B$  direction resulting in a branching into two main channels. The angle between these branches increases with the magnetic field strength, and at 40 T they propagate almost parallel to the magnetic field, and thus almost perpendicular to the background electric field. We think there are two mechanisms that deform the streamer head and thereby contribute to this branching: the dependence of the ionization rate on the angle between the  $E$  and  $B$ , and a reduction in electron drift velocity perpendicular to  $B$ . In agreement with earlier experimental work [33, 34, 32], we observe that positive streamer slightly bend towards the  $-E \times B$  direction, due to the  $E \times B$  drift of electrons. We also show that a perpendicular magnetic field reduces the streamer radius, a phenomenon that was earlier observed in axisymmetric simulations with a parallel magnetic field [35, 36]. However, a difference between the parallel and perpendicular cases is that the streamer velocity increases with a parallel magnetic field whereas it decreases with a perpendicular magnetic field.

Finally, we remind the reader that our results can be scaled to different pressures and corresponding field strengths. For example, our simulations 10 T at 1 bar should approximately correspond to 1 T at 0.1 bar at length and time scales a factor ten larger [9].

## **Chapter 6**

# **Conclusions and outlook**

In this chapter, we present a summary of the findings in this thesis and potential directions for future research.

## 6.1 Summary of findings

In this thesis, our primary focus was on positive streamers in atmospheric air. Our main findings are listed below.

### Fluid models vs. particle models

In chapter 2, a PIC-MCC (particle-in-cell, Monte Carlo collision) model and a drift-diffusion-reaction fluid model using the same AMR framework were quantitatively compared for positive streamer discharges. The simulations were performed in air at 1 bar and 300 K, in background fields ranging from 15 to 20 kV/cm. Both axisymmetric and fully three-dimensional geometries were considered and agreed well. Good agreement between the particle and the fluid simulations was also found for streamer properties such as maximal electric field, radius, and velocity. In section 2.3.3, the numerical convergence in both models was also studied, by varying the mesh refinement criterion. Convergence errors in streamer velocity were less than 2% in both models when compared with a standard refinement criterion.

### 2D Cartesian simulations vs. 2D axisymmetric simulations

In chapter 3, we compared 2D Cartesian and 2D axisymmetric simulations of positive streamers in air at 1 bar and 300 K using a fluid model. When using a same electrode geometry, the inception voltage in 2D Cartesian simulations was twice as in 2D axisymmetric simulations due to weaker electric field enhancement. When both types of models are compared at a similar ratio of applied voltage over the inception voltage, velocities and streamer radii became similar. However, the maximal electric field and degree of ionization in the 2D Cartesian case were significantly lower. Additionally, 2D Cartesian fluid models are not suitable for studying streamer branching, as branching only occurs with added noise and the resulting branches are much thinner than in real discharges in air.

### The selection of transport data for fluid models

Fluid simulations are sensitive to the type of input data that is used. A fluid model with flux transport coefficients, whether computed by Monte Carlo



method or using BOLSIG+ with the temporal growth option, lead to good agreement with particle models. There are major discrepancies between the models when bulk coefficients are used, or when data is computed using BOLSIG+ with the spatial growth option. These results can be found in section 2.3.2.

### **Source of stochasticity in streamer modeling**

In section 2.3.4, the number of super-particles (super-electrons) per cell  $N_{ppc}$  and the photoionization coefficient  $\xi$  were varied to investigate the source of stochasticity in streamer modeling. With stochastic photoionization, fluid simulations exhibited similar fluctuations as particle simulations when using the same value of  $\xi$ .  $N_{ppc}$  did not significantly impact these fluctuations, so it was concluded that discrete photoionization was the primary source of stochastic fluctuations. In chapter 4, photoionization was also confirmed to be the main mechanism responsible for streamer branching in air.

### **Streamer branching**

The effect of photoionization on positive streamer branching was studied using 3D fluid simulations with stochastic photoionization in chapter 4. We found good quantitative agreement in streamer branching behavior between our simulations and dedicated experiments, and therefore concluded that photoionization was the main mechanism governing the observed streamer branching. Changing the photoionization coefficient  $\xi$  from its standard value led to significant differences in the resulting streamer morphology. These simulations can therefore be used as a sensitive test for Zheleznyak's photoionization model.

### **Streamer behavior in a strong external magnetic field**

In chapter 5, the propagation of positive streamers in air in a strong external magnetic field of up to 40 T was simulated using a particle model. We considered magnetic fields aligned either parallel or perpendicular to the applied electric field. For parallel magnetic fields, the radii of positive streamers decreased with the magnetic field strength, and the velocity and

the maximal electron density of the streamer channels increased. For perpendicular magnetic fields, positive streamers tended to branch quite symmetrically into two main thin channels. The angle between these branches increased with the magnetic field strength. The dependence of the ionization rate on the angle between the  $\mathbf{E}$  and  $\mathbf{B}$ , along with the reduction in electron drift velocity perpendicular to  $\mathbf{B}$  were the two mechanisms that were found to cause this branching. We also observed that positive streamers slightly bend towards the  $-\mathbf{E} \times \mathbf{B}$  direction, due to the  $\mathbf{E} \times \mathbf{B}$  drift of electrons, in agreement with earlier related experimental work.

## 6.2 Outlook

- **A more extensive comparison between particle models and fluid models**

In chapter 2, we simulated positive streamer discharges in air in a limited range of background electric fields. A more extensive comparison could be performed, considering for example both positive and negative discharges, different gas compositions, and streamers interacting with solid surfaces. It would also be interesting to compare these models in very high fields, in which runaway electrons can be generated, as well as in low fields, in which gradients can become steeper.

- **Branching mechanisms in other gases should be investigated**

Simulations of streamer branching should be extended to a wider range of applied voltages, gas pressures and gas compositions. Depending on such conditions, different mechanisms may affect streamer branching behavior. For example, streamers with complex branching have been observed in  $\text{CO}_2$ , in which there is no effective photoionization process.

- **Simulations of negative streamers in strong external magnetic fields**

In Chapter 5, only positive streamers in strong external magnetic fields were simulated with our particle model. A further investigation

with negative streamers is required to test our conclusion about the polarity dependence of the  $\mathbf{E} \times \mathbf{B}$  bending.

- **Machine learning could improve streamer discharge modeling**

Machine learning (ML) can help increase model accuracy and efficiency. In streamer simulations, some input data related to chemical reactions or different gases remain uncertain, which can influence the simulation results. By feeding experimental data into machine learning models, the relationships between various governing parameters of streamers can be learned, which could lead to more accurate and efficient simulations. A model for branching streamers with complex branching structures can possibly be built using machine learning methods. Such models can focus on streamer properties such as velocity, radius and branching behavior, without considering the microscopic motion and collisions of electrons.

- **A graphical user interface for Afivo simulations**

Our Afivo code is written in FORTRAN and controlled by configuration files with long lists of input parameters. A graphical user interface (GUI) could provide a visual interface that simplifies complex operations and empowers users with a seamless, interactive environment. This modernization not only facilitates ease of use for our team members but also ensures that others can effectively utilize and improve our code.



## **Appendix A**

# **Computational cost**



In chapter 2, typical computing times for the results in section 2.3.1 were a few minutes (2D fluid model), 8h (3D fluid model), and 2-3h (2D particle model). These computations ran on an Intel(R) Core(TM) i9-9900K eight-core processor, using OpenMP parallelization. The 3D particle simulations were performed on Cartesius, the Dutch national supercomputer. A single thin node with a Intel Xeon E5-2690 v3 (Haswell) 24-core processor and 64 GB of RAM was used. Computations ran for up to five days, with up to 600 million particles.

The maximum number of grid cells used for the simulations presented in section 2.3.1 were:  $4.2 \times 10^4$  (2D fluid),  $1.4 \times 10^8$  (3D fluid),  $5.1 \times 10^4$  (2D particle),  $8.3 \times 10^7$  (3D particle). For the numerical convergence tests presented in section 2.3.3, the maximum number of grid cells at  $t = 9$  ns were  $2.4 \times 10^5$ ,  $8.5 \times 10^4$ ,  $3.8 \times 10^4$ ,  $3.3 \times 10^4$  (2D fluid,  $c_0 = 0.2, 0.4, 0.8, 1.0$  respectively) and  $2.0 \times 10^5$ ,  $8.2 \times 10^4$ ,  $4.2 \times 10^4$ ,  $3.5 \times 10^4$  (2D particle,  $c_0 = 0.2, 0.4, 0.8, 1.0$  respectively).

Typical computing times for a single run in chapter 4 under the conditions of the main text were 12 to 36 hours. These computations ran on Snellius, the Dutch national supercomputer, using 32 cores (AMD Rome 7H12) and 64 GB of RAM.

The maximum number of grid cells used for the simulations presented in the main text were  $0.5 \times 10^7$  for single streamers and  $1.9 \times 10^7$  for branching streamers. The minimal grid size in simulations was  $12 \mu\text{m}$ .





## **Appendix B**

# **Simulation set-up for branching streamers in air**



## B.1 Photoionization and initial electron density

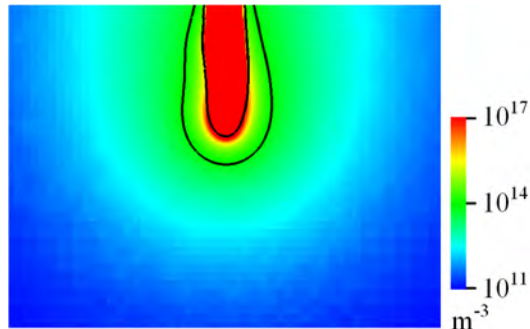


Figure B.1: Cross section through a simulation at 15 kV, showing the electron density around a non-branched streamer in the middle of the discharge gap. The black contour lines demarcate the area in which the electric field is above breakdown.

The electron density around a streamer head is illustrated in figure B.1, which shows a cross section through a simulation at 15 kV. Although photoionization was here found to be the main mechanism behind streamer branching, it can be seen that it produces a relatively smooth electron density around the streamer head. The region where the electric field is above breakdown is indicated in the figure. The electron density at the outer boundary of this region is about  $10^{14} \text{ m}^{-3}$ . It is therefore not possible to identify particular photoionization events (or the resulting avalanches) with branching events. Instead, fluctuations in the electron density ahead of the discharge deform the streamer head shape, and these deformations can lead to branching. They also cause the non-straight growth of non-branched streamer channels, see for example figure B.4.

Note that the electron density produced by photoionization is several orders of magnitude higher than the background electron density of  $10^{11} \text{ m}^{-3}$  that was used in the simulations as an initial condition. This background ionization therefore has no significant effect on our simulation results. This is illustrated in figure B.2, in which it is replaced by a localized Gaussian seed with a peak density of  $10^{13} \text{ m}^{-3}$ . This seed provides the first electrons near the electrode to ensure a discharge can start, but it has no significant

effect on the later discharge evolution.

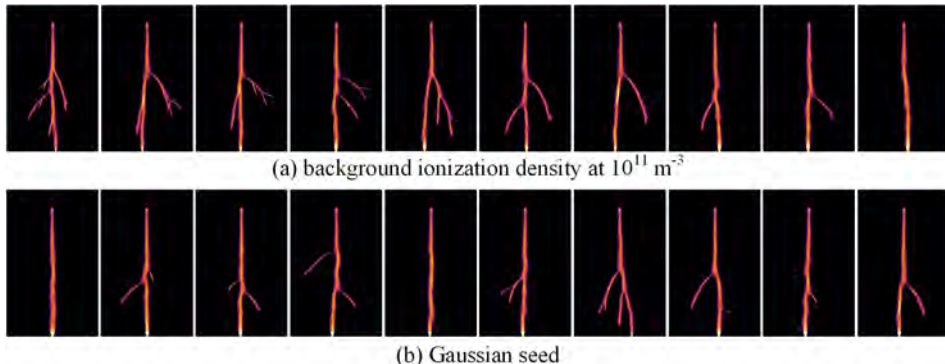


Figure B.2: 10 runs of streamers initiated from a Gaussian seed at 15 kV. Here the initial electron and ion densities are given by a Gaussian distribution  $n_i(\mathbf{r}) = n_e(\mathbf{r}) = 10^{13} \text{ m}^{-3} \exp[-(\mathbf{r} - \mathbf{r}_0)^2/(2 \text{ mm})^2]$ , where  $r_0$  is the location of the tip of the electrode.

## B.2 Ionization density due to previous pulses

The experiments use voltage pulses of  $1 \mu\text{s}$  duration at a repetition rate of 20 Hz, so there are 50 ms between the pulses. During this time electrons attach to oxygen, forming negative ions, and positive and negative ions recombine. If effects due ion diffusion are ignored, the ion density  $n$  at the start of a next pulse can be estimated as [131, 89, 26]:

$$n(t) = (k_{\text{rec}} t)^{-1}, \quad (\text{B.1})$$

where  $k_{\text{rec}}$  is the effective ion recombination rate, which typically lies between  $10^{-12} \text{ m}^3\text{s}^{-1}$  and  $10^{-13} \text{ m}^3\text{s}^{-1}$  [26]. This gives an estimated ionization density  $n(50 \text{ ms})$  between  $2 \times 10^{13} \text{ m}^{-3}$  and  $2 \times 10^{14} \text{ m}^{-3}$ . These densities are comparable to the electron density produced by photoionization, see figure B.1. If the main negative ions would for example be  $\text{O}_2^-$  or  $\text{O}^-$ , then they could have a significant effect on the next pulse due to electron detachment.

However, previous work on discharge inception [153] has indicated that remaining negative ions do not easily give up electrons through detachment. This is consistent with the fact that inception often occurred with a significant delay in our experiments. A possible explanation could be that the main stable negative ion is  $O_3^-$  [26, 154], from which electrons hardly detach. We therefore expect background ionization from previous pulses to not significantly affect the branching behavior observed here. For more recent results on the effect of ion conversion and of electron attachment and detachment processes on the electron density in repetitive discharges, we refer to [155, 156, 157].

### B.3 Pulse rise time

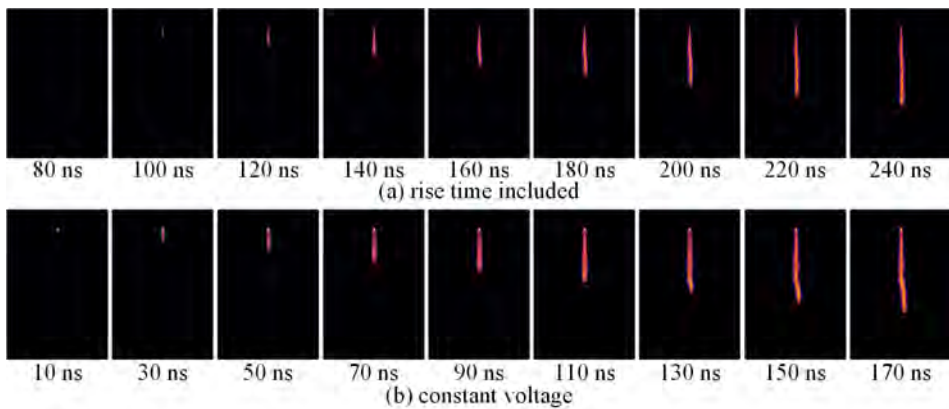


Figure B.3: Time evolution in simulations at 15 kV. For the top row a rise time of 105 ns was used, for the bottom row the voltage was applied instantaneously.

In the experiments, a rise rate of 0.14 kV/ns was used for the different applied voltages, which leads to rise times of about 105 ns (at 15 kV), 119 ns (at 17 kV) and 133 ns (at 19 kV). As discussed in the main text, inception typically occurred when the voltage had already reached its maximum, which is why in the simulations the rise time was not taken into account. We now briefly test how the inclusion of a finite rise time affects the simulation

results.

Figure B.3 shows examples of streamer evolution with and without a rise time at 15 kV. Note that streamer inception occurs around 100 ns, when the applied voltage is already about 15 kV, so that the main effect is simply a delay in streamer inception. We observed similar inception delays of about 100 ns at voltages of 17 kV and 19 kV. The reason the rise time has no significant effect on the later propagation is that these voltages are all rather close to the inception voltage. If we would apply a significantly higher voltage the streamer would already propagate a significant distance while the voltage was rising, leading to a stronger dependence on the rise time [158].

## B.4 Time evolution

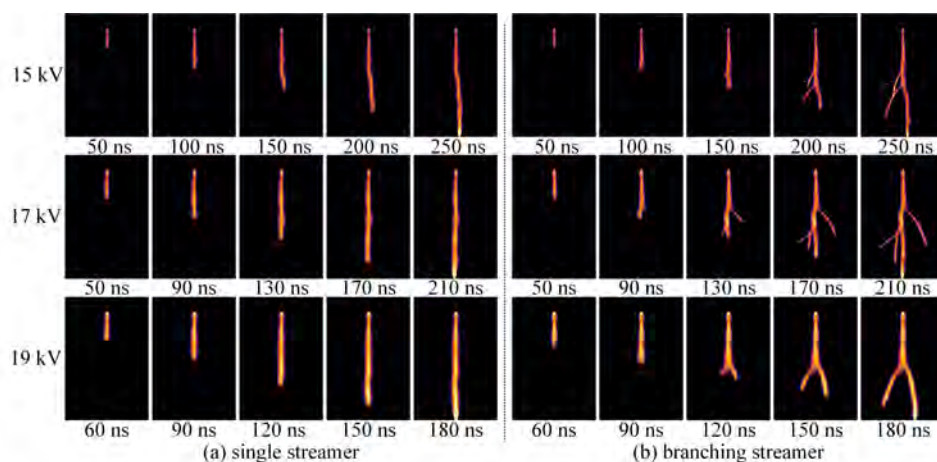


Figure B.4: Examples of time evolution in simulations under applied voltage of 15 kV, 17 kV and 19 kV. Shown is the integrated light emission, with cases without branching on the left and cases with branching on the right.

Figure B.4 illustrates the time evolution in simulations at different applied voltages. At each voltage, both single and branching streamers bridge the gap around the same time, so branching does not significantly affect

the streamer velocity, as also discussed in the main text.

## B.5 Radii before and after branching

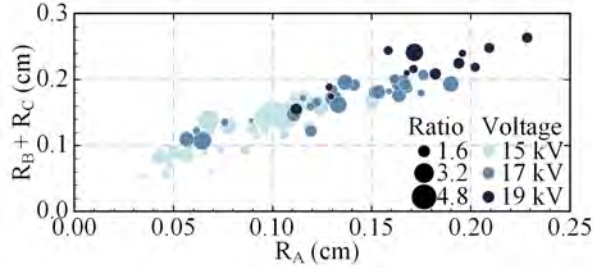


Figure B.5: Streamer radii 20 ns before ( $R_A$ ) and 20 ns after ( $R_B$ ,  $R_C$ ) branching in simulations. The sizes of the circles represent the ratio  $R_B/R_C$ , with  $R_B \geq R_C$ .

In the simulations, we have measured streamer radii before and after branching. Figure B.5 shows the sum of the radii after branching ( $R_B + R_C$ ) versus the parent radius  $R_A$ . The results suggest a relation  $R_A = k \times (R_B + R_C)$ , with  $k \approx 1.3$ , but they are also consistent with the relation  $R_A^2 = R_B^2 + R_C^2$  observed before in [125, 127].





# Bibliography

- [1] S. Pancheshnyi, M. Nudnova, and A. Starikovskii. Development of a cathode-directed streamer discharge in air at different pressures: Experiment and comparison with direct numerical simulation. *Physical Review E*, 71(1):016407, 2005.
- [2] T. M. P. Briels, E. M. van Veldhuizen, and U. Ebert. Positive streamers in air and nitrogen of varying density: Experiments on similarity laws. *Journal of Physics D: Applied Physics*, 41(23):234008, 2008.
- [3] S. Nijdam, F. M. J. H. van de Wetering, R. Blanc, E. M. van Veldhuizen, and U. Ebert. Probing photo-ionization: Experiments on positive streamers in pure gases and mixtures. *Journal of Physics D: Applied Physics*, 43(14):145204, 2010.
- [4] G. A. Dawson. Temporal growth of suppressed corona streamers in atmospheric air. *Journal of Applied Physics*, 36(11):3391–3395, 1965.
- [5] N. L. Allen and A. Ghaffar. The conditions required for the propagation of a cathode-directed positive streamer in air. *Journal of Physics D: Applied Physics*, 28(2):331, 1995.
- [6] P. Tardiveau, E. Marode, and A. Agneray. Tracking an individual streamer branch among others in a pulsed induced discharge. *Journal of Physics D: Applied Physics*, 35(21):2823, 2002.
- [7] G. J. J. Winands, Z. Liu, A. J. M. Pemen, E. J. M. Van Heesch, and K. Yan. Analysis of streamer properties in air as function of pulse and reactor parameters by iccd photography. *Journal of Physics D: Applied Physics*, 41(23):234001, 2008.

- [8] X. Meng, H. Mei, C. Chen, L. Wang, Z. Guan, and J. Zhou. Characteristics of streamer propagation along the insulation surface: Influence of dielectric material. *IEEE Transactions on Dielectrics and Electrical Insulation*, 22(2):1193–1203, 2015.
- [9] S. Nijdam, J. Teunissen, and U. Ebert. The physics of streamer discharge phenomena. *Plasma Sources Science and Technology*, 29(10):103001, 2020.
- [10] A. Luque and U. Ebert. Emergence of sprite streamers from screening-ionization waves in the lower ionosphere. *Nature Geoscience*, 2(11):757–760, 2009.
- [11] A. Luque and F. J. Gordillo-Vázquez. Mesospheric electric breakdown and delayed sprite ignition caused by electron detachment. *Nature Geoscience*, 5(1):22–25, 2012.
- [12] N. Liu, J. R. Dwyer, H. C. Stenbaek-Nielsen, and M. G. McHarg. Sprite streamer initiation from natural mesospheric structures. *Nature Communications*, 6(1):7540, 2015.
- [13] G. Sathiamoorthy, S. Kalyana, W. C. Finney, R. J. Clark, and B. R. Locke. Chemical reaction kinetics and reactor modeling of NO<sub>x</sub> removal in a pulsed streamer corona discharge reactor. *Industrial & Engineering Chemistry Research*, 38(5):1844–1855, 1999.
- [14] R. Ono and T. Oda. Dynamics of ozone and oh radicals generated by pulsed corona discharge in humid-air flow reactor measured by laser spectroscopy. *Journal of Applied Physics*, 93(10):5876–5882, 2003.
- [15] A. Malagón-Romero and A. Luque. Spontaneous emergence of space stems ahead of negative leaders in lightning and long sparks. *Geophysical Research Letters*, 46(7):4029–4038, 2019.
- [16] Earthsky. <https://earthsky.org/>.
- [17] H. Kim. Nonthermal plasma processing for air-pollution control: A historical review, current issues, and future prospects. *Plasma Processes and Polymers*, 1(2):91–110, 2004.

- [18] P. J. Bruggeman, M. J. Kushner, B. R. Locke, J. G. E. Gardeniers, W. G. Graham, D. B. Graves, R. C. H. M. Hofman-Caris, D. Maric, J. P. Reid, E. Ceriani, D. Fernandez Rivas, J. E. Foster, S. C. Garrick, Y. Gorbanev, S. Hamaguchi, F. Iza, H. Jablonowski, E. Klimova, J. Kolb, F. Krcma, P. Lukes, Z. Machala, I. Marinov, D. Mariotti, S. Mededovic Thagard, D. Minakata, E. C. Neyts, J. Pawlat, Z. L.j. Petrovic, R. Pflieger, S. Reuter, D. C. Schram, S. Schröter, M. Shiraiwa, B. Tarabová, P. A. Tsai, J. R. R. Verlet, T. von Woedtke, K. R. Wilson, K. Yasui, and G. Zvereva. Plasma-liquid interactions: A review and roadmap. *Plasma Sources Science and Technology*, 25(5):053002, 2016.
- [19] L. Bárdos and H. Baránková. Cold atmospheric plasma: Sources, processes, and applications. *Thin Solid Films*, 518(23):6705–6713, 2010.
- [20] M. Keidar, A. Shashurin, O. Volotskova, Ann S. M., P. Srinivasan, A. Sandler, and B. Trink. Cold atmospheric plasma in cancer therapy. *Physics of Plasmas*, 20(5):057101, 2013.
- [21] S. M. Starikovskaia. Plasma-assisted ignition and combustion: Nanosecond discharges and development of kinetic mechanisms. *Journal of Physics D: Applied Physics*, 47(35):353001, 2014.
- [22] Y. Itikawa. Cross sections for electron collisions with oxygen molecules. *Journal of Physical and Chemical Reference Data*, 38(1):1–20, 2009.
- [23] Y. Itikawa. Cross sections for electron collisions with nitrogen molecules. *Journal of Physical and Chemical Reference Data*, 35(1):31–53, 2006.
- [24] L. M. Chanin, A. V. Phelps, and M. A. Biondi. Measurements of the attachment of low-energy electrons to oxygen molecules. *Physical Review*, 128(1):219, 1962.
- [25] J. L. Pack and A. V. Phelps. Electron attachment and detachment. i. pure  $O_2$  at low energy. *The Journal of Chemical Physics*, 44(5):1870–1883, 1966.

- [26] I. A. Kossyi, A. Y. Kostinsky, A. A. Matveyev, and V. P. Silakov. Kinetic scheme of the non-equilibrium discharge in nitrogen-oxygen mixtures. *Plasma Sources Science and Technology*, 1(3):207–220, 1992.
- [27] J. Teunissen. *3D Simulations and Analysis of Pulsed Discharges*. PhD thesis, Technische Universiteit Eindhoven, 2015.
- [28] M. B. Zhelezniak, A. K. Mnatsakanian, and S. V. Sizykh. Photoionization of nitrogen and oxygen mixtures by radiation from a gas discharge. *High Temperature Science*, 20(3):357–362, 1982.
- [29] U. Ebert, S. Nijdam, C. Li, A. Luque, T. Briels, and E. van Veldhuizen. Review of recent results on streamer discharges and discussion of their relevance for sprites and lightning. *Journal of Geophysical Research: Space Physics*, 115(A7), 2010.
- [30] S. Dujko, R. D. White, Z. Lj. Petrović, and R. E. Robson. Benchmark calculations of nonconservative charged-particle swarms in DC electric and magnetic fields crossed at arbitrary angles. *Physical Review E*, 81(4):046403, 2010.
- [31] R. Janalizadeh, Z. Pervez, and V. P. Pasko. Efficient modeling of electron kinetics under influence of externally applied electric field in magnetized weakly ionized plasma. *Plasma Sources Science and Technology*, 32(7):075004, 2023.
- [32] F. Manders, P. C. M. Christianen, and J. C. Maan. Propagation of a streamer discharge in a magnetic field. *Journal of Physics D: Applied Physics*, 41(23):234006, 2008.
- [33] P. Uhlig, J. C. Maan, and P. Wyder. Spatial evolution of filamentary surface discharges in high magnetic fields. *Physical Review Letters*, 63(18):1968, 1989.
- [34] M. Hara, J. Suehiro, and T. Wakiyama. Deflection of streamer channels in high magnetic field. *IEEE Transactions on Electrical Insulation*, 27(6):1179–1185, 1992.

- [35] A. Y. Starikovskiy, N. L. Aleksandrov, and M. N. Shneider. Streamer self-focusing in an external longitudinal magnetic field. *Physical Review E*, 103(6):063201, 2021.
- [36] R. Janalizadeh and V. P. Pasko. Preliminary modeling of magnetized sprite treamers on Jupiter following Juno’s observations of possible transient luminous events. *Journal of Geophysical Research: Space Physics*, 128(2), 2023.
- [37] J. Teunissen and U. Ebert. 3D PIC-MCC simulations of discharge inception around a sharp anode in nitrogen/oxygen mixtures. *Plasma Sources Science and Technology*, 25(4):044005, 2016.
- [38] K. Nanbu. Probability theory of electron-molecule, ion-molecule, molecule-molecule, and coulomb collisions for particle modeling of materials processing plasmas and cases. *IEEE Transactions on Plasma Science*, 28(3):971–990, 2000.
- [39] A. Luque and U. Ebert. Density models for streamer discharges: Beyond cylindrical symmetry and homogeneous media. *Journal of Computational Physics*, 231(3):904–918, 2012.
- [40] J. Teunissen and U. Ebert. Simulating streamer discharges in 3D with the parallel adaptive afivo framework. *Journal of Physics D: Applied Physics*, 50(47):474001, 2017.
- [41] J. Teunissen and U. Ebert. Afivo: A framework for quadtree/octree AMR with shared-memory parallelization and geometric multigrid methods. *Computer Physics Communications*, 233:156–166, 2018.
- [42] S. Pancheshnyi. Photoionization produced by low-current discharges in O<sub>2</sub>, air, N<sub>2</sub> and CO<sub>2</sub>. *Plasma Sources Science and Technology*, 24(1):015023, 2014.
- [43] A. Bourdon, V. P. Pasko, N. Liu, S. Célestin, P. Ségur, and E. Marode. Efficient models for photoionization produced by non-thermal gas discharges in air based on radiative transfer and the helmholtz equations. *Plasma Sources Science and Technology*, 16(3):656, 2007.

- [44] A. Luque, U. Ebert, C. Montijn, and W. Hundsdorfer. Photoionization in negative streamers: Fast computations and two propagation modes. *Applied Physics Letters*, 90(8):081501, 2007.
- [45] B. Bagheri, J. Teunissen, U. Ebert, M. M. Becker, S. Chen, O. Ducasse, Ol. Eichwald, D. Loffhagen, A. Luque, D. Mihailova, et al. Comparison of six simulation codes for positive streamers in air. *Plasma Sources Science and Technology*, 27(9):095002, 2018.
- [46] O. Chanrion and T. Neubert. A PIC-MCC code for simulation of streamer propagation in air. *Journal of Computational Physics*, 227(15):7222–7245, 2008.
- [47] Biagi database ( $N_2$ ). [www.lxcat.net](http://www.lxcat.net), retrieved on September 23, 2023.
- [48] G. J. M. Hagelaar and L. C. Pitchford. Solving the boltzmann equation to obtain electron transport coefficients and rate coefficients for fluid models. *Plasma Sources Science and Technology*, 14(4):722, 2005.
- [49] Bolsig+ solver, 2019. [www.lxcat.net](http://www.lxcat.net), ver. 11/2019.
- [50] R. D. White, R. E. Robson, B. Schmidt, and M. A. Morrison. Is the classical two-term approximation of electron kinetic theory satisfactory for swarms and plasmas? *Journal of Physics D: Applied Physics*, 36(24):3125, 2003.
- [51] A. Banković, S. Dujko, R. D. White, S. J. Buckman, and Z. L. Petrović. On approximations involved in the theory of positron transport in gases in electric and magnetic fields. *The European Physical Journal D*, 66(7):1–10, 2012.
- [52] S. F. Biagi. Monte carlo simulation of electron drift and diffusion in counting gases under the influence of electric and magnetic fields. *Nuclear Instruments and Methods in Physics Research Section A: Accelerators, Spectrometers, Detectors and Associated Equipment*, 421(1-2):234–240, 1999.

- [53] M. Rabie and C. M. Franck. Methes: A monte carlo collision code for the simulation of electron transport in low temperature plasmas. *Computer Physics Communications*, 203:268–277, 2016.
- [54] Z. L. Petrović, S. Dujko, D. Marić, G. Malović, Ž. Nikitović, O. Šašić, J. Jovanović, V. Stojanović, and M. Radmilović-Rađenović. Measurement and interpretation of swarm parameters and their application in plasma modelling. *Journal of Physics D: Applied Physics*, 42(19):194002, 2009.
- [55] S. Dujko, A. H. Markosyan, R. D. White, and U. Ebert. High-order fluid model for streamer discharges: I. Derivation of model and transport data. *Journal of Physics D: Applied Physics*, 46(47):475202, 2013.
- [56] Z. Wang, A. Sun, and J. Teunissen. A comparison of particle and fluid models for positive streamer discharges in air. *Plasma Sources Science and Technology*, 31(1):015012, 2022.
- [57] V. P. Pasko, J. Qin, and S. Celestin. Toward better understanding of sprite streamers: Initiation, morphology, and polarity asymmetry. *Surveys in Geophysics*, 34(6):797–830, 2013.
- [58] S. Kanazawa, H. Kawano, S. Watanabe, T. Furuki, S. Akamine, R. Ichiki, T. Ohkubo, M. Kocik, and J. Mizeraczyk. Observation of OH radicals produced by pulsed discharges on the surface of a liquid. *Plasma Sources Science and Technology*, 20(3):034010, 2011.
- [59] D. V. Rose, D. R. Welch, R. E. Clark, C. Thoma, W. R. Zimmerman, N. Bruner, P. K. Rambo, and B. W. Atherton. Towards a fully kinetic 3D electromagnetic particle-in-cell model of streamer formation and dynamics in high-pressure electronegative gases. *Physics of Plasmas*, 18(9):093501, 2011.
- [60] V. Kolobov and R. Arslanbekov. Electrostatic PIC with adaptive Cartesian mesh. *Journal of Physics: Conference Series*, 719:012020, 2016.

- [61] D. Levko, M. Pachuilo, and L. L. Raja. Particle-in-cell modeling of streamer branching in CO<sub>2</sub> gas. *Journal of Physics D: Applied Physics*, 50(35):354004, 2017.
- [62] J. Stephens, M. Abide, A. Fierro, and A. Neuber. Practical considerations for modeling streamer discharges in air with radiation transport. *Plasma Sources Science and Technology*, 27(7):075007, 2018.
- [63] N. Y. Babaeva, D. V. Tereshonok, and G. V. Naidis. Fluid and hybrid modeling of nanosecond surface discharges: Effect of polarity and secondary electrons emission. *Plasma Sources Science and Technology*, 25(4):044008, 2016.
- [64] J. M. Plewa, O. Eichwald, O. Ducasse, P. Dessante, C. Jacobs, N. Renon, and M. Yousfi. 3D streamers simulation in a pin to plane configuration using massively parallel computing. *Journal of Physics D: Applied Physics*, 51(9):095206, 2018.
- [65] B. Bagheri and J. Teunissen. The effect of the stochasticity of photoionization on 3D streamer simulations. *Plasma Sources Science and Technology*, 28(4):045013, 2019.
- [66] R. Marskar. An adaptive Cartesian embedded boundary approach for fluid simulations of two- and three-dimensional low temperature plasma filaments in complex geometries. *Journal of Computational Physics*, 388:624–654, 2019.
- [67] A. Y. Starikovskiy and N. L. Aleksandrov. How pulse polarity and photoionization control streamer discharge development in long air gaps. *Plasma Sources Science and Technology*, 29(7):075004, 2020.
- [68] R. Ono and A. Komuro. Generation of the single-filament pulsed positive streamer discharge in atmospheric-pressure air and its comparison with two-dimensional simulation. *Journal of Physics D: Applied Physics*, 53(3):035202, 2020.
- [69] N. A. Garland, D. G. Cocks, G. J. Boyle, S. Dujko, and R. D. White. Unified fluid model analysis and benchmark study for electron transport in gas and liquid analogs. *Plasma Sources Science and Technology*, 26(7):075003, 2017.



- [70] U. Kortshagen, C. Busch, and L. D. Tsendin. On simplifying approaches to the solution of the Boltzmann equation in spatially inhomogeneous plasmas. *Plasma Sources Science and Technology*, 5(1):1–17, 1996.
- [71] D. Trunec, Z. Bonaventura, and D. Nečas. Solution of time-dependent Boltzmann equation for electrons in non-thermal plasma. *Journal of Physics D: Applied Physics*, 39(12):2544–2552, 2006.
- [72] P. J. Drallos, V. P. Nagorny, and W. Williamson. A kinetic study of the local field approximation in simulations of AC plasma display panels. *Plasma Sources Science and Technology*, 4(4):576–590, 1995.
- [73] G. K. Grubert, M. M. Becker, and D. Loffhagen. Why the local-mean-energy approximation should be used in hydrodynamic plasma descriptions instead of the local-field approximation. *Physical Review E*, 80(3):036405, 2009.
- [74] R. E. Robson, R. D. White, and Z. L. Petrović. Colloquium: Physically based fluid modeling of collisionally dominated low-temperature plasmas. *Reviews of Modern Physics*, 77(4):1303, 2005.
- [75] C. Li, J. Teunissen, M. Nool, W. Hundsdorfer, and U. Ebert. A comparison of 3D particle, fluid and hybrid simulations for negative streamers. *Plasma Sources Science and Technology*, 21(5):055019, 2012.
- [76] A. H. Markosyan, J. Teunissen, S. Dujko, and U. Ebert. Comparing plasma fluid models of different order for 1D streamer ionization fronts. *Plasma Sources Science and Technology*, 24(6):065002, 2015.
- [77] H. Kim, F. Iza, S. Yang, M. Radmilović-Radjenović, and J. Lee. Particle and fluid simulations of low-temperature plasma discharges: Benchmarks and kinetic effects. *Journal of Physics D: Applied Physics*, 38(19):R283, 2005.
- [78] S. H. Lee, F. Iza, and J. K. Lee. Particle-in-cell Monte Carlo and fluid simulations of argon-oxygen plasma: Comparisons with experiments and validations. *Physics of Plasmas*, 13(5):057102, 2006.

- [79] Y. Hong, M. Yoon, F. Iza, G. Kim, and J. Lee. Comparison of fluid and particle-in-cell simulations on atmospheric pressure helium microdischarges. *Journal of Physics D: Applied Physics*, 41(24):245208, 2008.
- [80] M. M. Becker, H. Kählert, A. Sun, M. Bonitz, and D. Loffhagen. Advanced fluid modeling and PIC/MCC simulations of low-pressure ccrf discharges. *Plasma Sources Science and Technology*, 26(4):044001, 2017.
- [81] K. Koura. Null-collision technique in the direct-simulation Monte Carlo method. *Physics of Fluids*, 29(11):3509, 1986.
- [82] R. W. Hockney and J. W. Eastwood. *Computer Simulation Using Particles*. IOP Publishing Ltd., Bristol, England, 1988.
- [83] J. Teunissen and U. Ebert. Controlling the weights of simulation particles: Adaptive particle management using k-d trees. *Journal of Computational Physics*, 259:318–330, 2014.
- [84] S. J. Araki and R. E. Wirz. Cell-centered particle weighting algorithm for PIC simulations in a non-uniform 2D axisymmetric mesh. *Journal of Computational Physics*, 272:218–226, 2014.
- [85] A. V. Phelps and L. C. Pitchford. Anisotropic scattering of electrons by  $N_2$  and its effect on electron transport. *Physical Review A*, 31(5):2932, 1985.
- [86] L. C. Pitchford and A. V. Phelps. Comparative calculations of electron-swarm properties in  $N_2$  at moderate  $E/N$  values. *Physical Review A*, 25(1):540–554, 1982.
- [87] B. Koren. *A Robust Upwind Discretization Method for Advection, Diffusion and Source Terms*. Braunschweig/Wiesbaden: Vieweg, 1993.
- [88] X. Li, S. Dijcks, S. Nijdam, A. Sun, U. Ebert, and J. Teunissen. Comparing simulations and experiments of positive streamers in air: Steps toward model validation. *Plasma Sources Science and Technology*, 30(9):095002, 2021.

- [89] G. Wormeester, S. Pancheshnyi, A. Luque, S. Nijdam, and U. Ebert. Probing photo-ionization: Simulations of positive streamers in varying  $N_2$ :  $O_2$ -mixtures. *Journal of Physics D: Applied Physics*, 43(50):505201, 2010.
- [90] R. Marskar. 3D fluid modeling of positive streamer discharges in air with stochastic photoionization. *Plasma Sources Science and Technology*, 29(5):055007, 2020.
- [91] A. Fridman, A. Chirokov, and A. Gutsol. Non-thermal atmospheric pressure discharges. *Journal of Physics D: Applied Physics*, 38(2):R1, 2005.
- [92] P. J. Bruggeman, F. Iza, and R. Brandenburg. Foundations of atmospheric pressure non-equilibrium plasmas. *Plasma Sources Science and Technology*, 26(12):123002, 2017.
- [93] D. Wang and T. Namihira. Nanosecond pulsed streamer discharges: II. Physics, discharge characterization and plasma processing. *Plasma Sources Science and Technology*, 29(2):023001, 2020.
- [94] S. A. Cummer, N. Jaugey, J. Li, W. A. Lyons, T. E. Nelson, and E. A. Gerken. Submillisecond imaging of sprite development and structure. *Geophysical Research Letters*, 33(4), 2006.
- [95] M. G. McHarg, H. C. Stenbaek-Nielsen, and T. Kammae. Observations of streamer formation in sprites. *Geophysical Research Letters*, 34(6), 2007.
- [96] Z. Wang, S. Dijcks, Y. Guo, M. Van Der Leegte, A. Sun, U. Ebert, S. Nijdam, and J. Teunissen. Quantitative modeling of streamer discharge branching in air. *Plasma Sources Science and Technology*, 32(8):085007, 2023.
- [97] A. Sobota, A. Lebouvier, N. J. Kramer, E. M. Van Veldhuizen, W. W. Stoffels, F. Manders, and M. Haverlag. Speed of streamers in argon over a flat surface of a dielectric. *Journal of Physics D: Applied Physics*, 42(1):015211, 2009.

- [98] S. A. Stepanyan, A. Y. Starikovskiy, N. A. Popov, and S. M. Starikovskaia. A nanosecond surface dielectric barrier discharge in air at high pressures and different polarities of applied pulses: Transition to filamentary mode. *Plasma Sources Science and Technology*, 23(4):045003, 2014.
- [99] C. Ding, A. Jean, N. A. Popov, and S. M. Starikovskaia. Fine structure of streamer-to-filament transition in high-pressure nanosecond surface dielectric barrier discharge. *Plasma Sources Science and Technology*, 31(4):045013, 2022.
- [100] V. R. Soloviev and V. M. Krivtsov. Surface barrier discharge modelling for aerodynamic applications. *Journal of Physics D: Applied Physics*, 42(12):125208, 2009.
- [101] V. R. Soloviev and V. M. Krivtsov. Mechanism of streamer stopping in a surface dielectric barrier discharge. *Plasma Physics Reports*, 40:65–77, 2014.
- [102] H. K. Meyer, F. Mauseth, R. Marskar, A. Pedersen, and A. Blaszczyk. Streamer and surface charge dynamics in non-uniform air gaps with a dielectric barrier. *IEEE Transactions on Dielectrics and Electrical Insulation*, 26(4):1163–1171, 2019.
- [103] H. K. H. Meyer, R. Marskar, H. Gjerdal, and F. Mauseth. Streamer propagation along a profiled dielectric surface. *Plasma Sources Science and Technology*, 29(11):115015, 2020.
- [104] X. Li, A. Sun, G. Zhang, and J. Teunissen. A computational study of positive streamers interacting with dielectrics. *Plasma Sources Science and Technology*, 29(6):065004, 2020.
- [105] X. Li, A. Sun, and J. Teunissen. A computational study of negative surface discharges: Characteristics of surface streamers and surface charges. *IEEE Transactions on Dielectrics and Electrical Insulation*, 27(4):1178–1186, 2020.
- [106] J. Kruszelnicki, R. Ma, and M. J. Kushner. Propagation of atmospheric pressure plasmas through interconnected pores in dielectric materials. *Journal of Applied Physics*, 129(14), 2021.

- [107] N. Y. Babaeva, G. V. Naidis, and M. J. Kushner. Interaction of positive streamers in air with bubbles floating on liquid surfaces: Conductive and dielectric bubbles. *Plasma Sources Science and Technology*, 27(1):015016, 2018.
- [108] J. Teunissen and F. Schiavello. Geometric multigrid method for solving poisson’s equation on octree grids with irregular boundaries. *Computer Physics Communications*, 286:108665, 2023.
- [109] Phelps database (N<sub>2</sub>,O<sub>2</sub>). [www.lxcat.net](http://www.lxcat.net), retrieved on March 30, 2021.
- [110] S. A. Lawton and A. V. Phelps. Excitation of the  $b^1\Sigma_g^+$  state of O<sub>2</sub> by low energy electrons. *The Journal of Chemical Physics*, 69(3):1055–1068, 1978.
- [111] S. V. Pancheshnyi, S. V. Sobakin, S. M. Starikovskaya, and A. Y. Starikovskii. Discharge dynamics and the production of active particles in a cathode-directed streamer. *Plasma Physics Reports*, 26(12):1054–1065, 2000.
- [112] G. V. Naidis. Positive and negative streamers in air: Velocity-diameter relation. *Physical Review E*, 79(5), 2009.
- [113] U. Ebert, W. van Saarloos, and C. Caroli. Streamer propagation as a pattern formation problem: Planar fronts. *Physical Review Letters*, 77(20):4178–4181, 1996.
- [114] N. Y. Babaeva and G. V. Naidis. Two-dimensional modelling of positive streamer dynamics in non-uniform electric fields in air. *Journal of Physics D: Applied Physics*, 29(9):2423–2431, 1996.
- [115] G. V. Naidis. Modelling of plasma chemical processes in pulsed corona discharges. *Journal of Physics D: Applied Physics*, 30(8):1214–1218, 1997.
- [116] X. Li, B. Guo, A. Sun, U. Ebert, and J. Teunissen. A computational study of steady and stagnating positive streamers in N<sub>2</sub>- O<sub>2</sub> mixtures. *Plasma Sources Science and Technology*, 31:065011, 2022.

- [117] D. Bouwman, H. Francisco, and U. Ebert. Estimating the properties of single positive air streamers from measurable parameters. *Plasma Sources Science and Technology*, 32(7):075015, 2023.
- [118] Z. Xiong and M. J. Kushner. Branching and path-deviation of positive streamers resulting from statistical photon transport. *Plasma Sources Science and Technology*, 23(6):065041, 2014.
- [119] U. Ebert, F. Brau, G. Derks, W. Hundsdorfer, C. Kao, C. Li, A. Luque, B. Meulenbroek, S. Nijdam, V. Ratushnaya, et al. Multiple scales in streamer discharges, with an emphasis on moving boundary approximations. *Nonlinearity*, 24(1):C1–C26, 2010.
- [120] W. Rison, P. R. Krehbiel, M. G. Stock, H. E. Edens, X. Shao, R. J. Thomas, M. A. Stanley, and Y. Zhang. Observations of narrow bipolar events reveal how lightning is initiated in thunderstorms. *Nature Communications*, 7(1):10721, 2016.
- [121] C. Sterpka, J. Dwyer, N. Liu, B. M. Hare, O. Scholten, S. Buitink, S. ter Veen, and A. Nelles. The spontaneous nature of lightning initiation revealed. *Geophysical Research Letters*, 48(23), 2021.
- [122] N. Liu and V. P. Pasko. Effects of photoionization on propagation and branching of positive and negative streamers in sprites. *Journal of Geophysical Research: Space Physics*, 109(A4), 2004.
- [123] L. Niemeyer, L. Pietronero, and H. Wiesmann. Fractal dimension of dielectric breakdown. *Physical Review Letters*, 52(12):1033–1036, 1984.
- [124] A. Luque and U. Ebert. Growing discharge trees with self-consistent charge transport: The collective dynamics of streamers. *New Journal of Physics*, 16(1):013039, 2014.
- [125] S. Nijdam, J. S. Moerman, T. M. P. Briels, E. M. van Veldhuizen, and U. Ebert. Stereo-photography of streamers in air. *Applied Physics Letters*, 92:101502, 2008.

- [126] L. C. J. Heijmans, S. Nijdam, E. M. van Veldhuizen, and U. Ebert. Streamers in air splitting into three branches. *Europhysics Letters*, 103(2):25002, 2013.
- [127] S. Chen, F. Wang, Q. Sun, and R. Zeng. Branching characteristics of positive streamers in nitrogen-oxygen gas mixtures. *IEEE Transactions on Dielectrics and Electrical Insulation*, 25(3):1128–1134, 2018.
- [128] J. Stephens, A. Fierro, S. Beeson, G. Laity, D. Trienekens, R. P. Joshi, J. Dickens, and A. Neuber. Photoionization capable, extreme and vacuum ultraviolet emission in developing low temperature plasmas in air. *Plasma Sources Science and Technology*, 25(2):025024, 2016.
- [129] S. Nijdam, G. Wormeester, E. M. van Veldhuizen, and U. Ebert. Probing background ionization: Positive streamers with varying pulse repetition rate and with a radioactive admixture. *Journal of Physics D: Applied Physics*, 44(45):455201, 2011.
- [130] E. Takahashi, S. Kato, A. Sasaki, Y. Kishimoto, and H. Furutani. Controlling branching in streamer discharge by laser background ionization. *Journal of Physics D: Applied Physics*, 44(7):075204, 2011.
- [131] S. Pancheshnyi. Role of electronegative gas admixtures in streamer start, propagation and branching phenomena. *Plasma Sources Science and Technology*, 14(4):645–653, 2005.
- [132] M. Arrayás, U. Ebert, and W. Hundsdorfer. Spontaneous branching of anode-directed streamers between planar electrodes. *Physical Review Letters*, 88(17):174502, 2002.
- [133] A. Luque and U. Ebert. Electron density fluctuations accelerate the branching of positive streamer discharges in air. *Physical Review E*, 84(4), 2011.
- [134] S. Dijcks, M. van der Leege, and S. Nijdam. Imaging and reconstruction of positive streamer discharge tree structures. *Plasma Sources Science and Technology*, 32(4):045004, 2023.

- [135] M. B. Zheleznyak, A. K. Mnatsakanian, and S. V. Sizykh. Photoionization of nitrogen and oxygen mixtures by radiation from a gas discharge. *Teplofizika Vysokikh Temperatur*, 20:423–428, 1982.
- [136] V. P. Pasko. Theoretical modeling of sprites and jets sprites, elves and intense lightning discharges (nato science series ii: Mathematics, physics and chemistry vol 225) ed m füllekrug et al, 2006.
- [137] M. Keidar, A. Shashurin, O. Volotskova, M. Ann Stepp, P. Srinivasan, A. Sandler, and B. Trink. Cold atmospheric plasma in cancer therapy. *Physics of Plasmas*, 20(5):057101, 2013.
- [138] G. J. M. Hagelaar. Modelling electron transport in magnetized low-temperature discharge plasmas. *Plasma Sources Science and Technology*, 16(1):S57–S66, 2007.
- [139] K. F. Ness. Multi-term solution of the boltzmann equation for electron swarms in crossed electric and magnetic fields. *Journal of Physics D: Applied Physics*, 27(9):1848, 1994.
- [140] V. P. Pasko. Red sprite discharges in the atmosphere at high altitude: The molecular physics and the similarity with laboratory discharges. *Plasma Sources Science and Technology*, 16(1):S13, 2007.
- [141] V. P. Pasko, U. S. Inan, T. F. Bell, and Y. N. Taranenko. Sprites produced by quasi-electrostatic heating and ionization in the lower ionosphere. *Journal of Geophysical Research: Space Physics*, 102(A3):4529–4561, March 1997.
- [142] J. E. P. Connerney, S. Timmins, R. J. Oliverson, J. R. Espley, J. L. Joergensen, S. Kotsiaros, P. S. Joergensen, J. M. G. Merayo, M. Hecceg, J. Bloxham, K. M. Moore, A. Mura, A. Moirano, S. J. Bolton, and S. M. Levin. A new model of jupiter’s magnetic field at the completion of juno’s prime mission. *Journal of Geophysical Research: Planets*, 127(2), 2022.
- [143] J. Bloxham, K. M. Moore, L. Kulowski, H. Cao, R. K. Yadav, D. J. Stevenson, J. E. P. Connerney, and S. J. Bolton. Differential rotation



- in Jupiter's interior revealed by simultaneous inversion for the magnetic field and zonal flux velocity. *Journal of Geophysical Research: Planets*, 127(5):e2021JE007138, 2022.
- [144] I. Kolmašová, O. Santolík, M. Imai, W. S. Kurth, G. B. Hospodarsky, J. E. P. Connerney, S. J. Bolton, and R. Lán. Lightning at jupiter pulsates with a similar rhythm as in-cloud lightning at earth. *Nature Communications*, 14(1), 2023.
- [145] R. S. Giles, T. K. Greathouse, B. Bonfond, G. R. Gladstone, J. A. Kammer, V. Hue, D. C. Grodent, J. Gérard, M. H. Versteeg, M. H. Wong, et al. Possible transient luminous events observed in jupiter's upper atmosphere. *Journal of Geophysical Research: Planets*, 125(11):e2020JE006659, 2020.
- [146] Olivier Chanrion and Torsten Neubert. A PIC-MCC code for simulation of streamer propagation in air. *Journal of Computational Physics*, 227(15):7222–7245, 2008.
- [147] Charles K. Birdsall and A. Bruce Langdon. *Plasma Physics via Computer Simulation*. Series in Plasma Physics. Taylor & Francis, New York, NY London, 2004.
- [148] Jannis Teunissen and Francesca Schiavello. Geometric multigrid method for solving Poisson's equation on octree grids with irregular boundaries. *Computer Physics Communications*, 286:108665, May 2023.
- [149] Reza Janalizadeh, Zaid Pervez, and Victor P Pasko. Efficient modeling of electron kinetics under influence of externally applied electric field in magnetized weakly ionized plasma. *Plasma Sources Science and Technology*, 32(7):075004, July 2023.
- [150] Z Lj Petrović, S Dujko, D Marić, G Malović, ž Nikitović, O Šašić, J Jovanović, V Stojanović, and M Radmilović-Radenović. Measurement and interpretation of swarm parameters and their application in plasma modelling. *Journal of Physics D: Applied Physics*, 42(19):194002, October 2009.

- [151] Ningyu Liu and Victor P. Pasko. Effects of photoionization on propagation and branching of positive and negative streamers in sprites. *Journal of Geophysical Research: Space Physics*, 109(A4):2003JA010064, April 2004.
- [152] A. Luque and U. Ebert. Electron density fluctuations accelerate the branching of positive streamer discharges in air. *Physical Review E*, 84(4):046411, October 2011.
- [153] S. Mirpour, A. Martinez, J. Teunissen, U. Ebert, and S. Nijdam. Distribution of inception times in repetitive pulsed discharges in synthetic air. *Plasma Sources Science and Technology*, 29(11):115010, 2020.
- [154] S. Pancheshnyi. Effective ionization rate in nitrogen-oxygen mixtures. *Journal of Physics D: Applied Physics*, 46(15):155201, 2013.
- [155] H. Francisco, B. Bagheri, and U. Ebert. Electrically isolated propagating streamer heads formed by strong electron attachment. *Plasma Sources Science and Technology*, 30(2):025006, 2021.
- [156] B. Guo and J. Teunissen. A computational study on the energy efficiency of species production by single-pulse streamers in air. *Plasma Sources Science and Technology*, 32(2):025001, 2023.
- [157] H. Malla, A. Martinez, U. Ebert, and J. Teunissen. Double-pulse streamer simulations for varying interpulse times in air. *Plasma Sources Science and Technology*, 32(9):095006, 2023.
- [158] A. Komuro, T. Ryu, A. Yoshino, T. Namihira, D. Wang, and R. Ono. Streamer propagation in atmospheric-pressure air: Effect of the pulse voltage rise rate from 0.1 to 100 kV Ns<sup>-1</sup> and streamer inception voltage. *Journal of Physics D: Applied Physics*, 54(36):364004, 2021.

# Acknowledgement

My PhD journey has been a challenging yet remarkably meaningful odyssey. Every hurdle, every breakthrough, has contributed to the rich mosaic of experiences that define my path today. Through perseverance and dedication, I have not only gained a wealth of knowledge but also discovered profound personal growth. This chapter of my life has been nothing short of an adventure, filled with valuable lessons, cherished memories, and an unwavering determination to forge ahead.

I would first like to express my deepest gratitude to my supervisors: Ute Ebert, Anbang Sun, and Jannis Teunissen. Your invaluable guidance and endless encouragement have been the cornerstone of my PhD journey. I owe a special debt of gratitude to Prof. Sun for recognizing my potential and giving me the opportunity to study abroad, thus realizing my childhood dream. Prof. Ebert and Dr. Teunissen have consistently valued my opinions and supported my every decision. Beyond the achievements in this thesis, they also taught me a crucial life experience: live your life for you, not to please expectations.

I am immensely grateful to the people I work with in the Netherlands, particularly Bastiaan Braams, Sander Nijdam, Hani Francisco, Hemaditya Malla, Baohong Guo, Xiaoran Li and Yihao Guo. Their insightful discussions, constructive feedback, and willingness to lend a helping hand made the beginning of my study abroad much smoother, especially during the pandemic. I also want to express my thanks to my group-mates in China - Haolin Li, Hanwei Li, Xuchu Yuan, Han Yan, Zeyu Li, Yulin Guo, and Xingyu Chen - my PhD would not have started and finished so smoothly without your help.

Special thanks are reserved for my best friends, who I consider as fam-

ilies in the Netherlands: Yang Liu and Tianyi Zhang. I still remember our first year together in Science Park, as well as our summer trip to the Alps. These memories are so precious that I will carry them with me forever. To Yuying Zhang, Qian Zhang, Xinhong Yang, Wenzhu Zhang, and Xi Chen: thank you for all the late-night talks and endless support in my life. I feel very lucky that our friendship has not dimmed despite the distance.

To my parents, who placed my education as the highest priority and taught me the invaluable lesson of never giving up: I can never be prouder of how our living standard improved in the last thirty years. I feel blessed to be your child, and I will carry your teachings with me always.

To Ruochen Guo, my beloved husband, my life partner and the sunshine beside my pillow: thank you for loving me on my bad days, for always listening to me, and for treating me better than I treat myself.

Lastly, to my precious son Shuzhan, who arrived in the final year of my PhD: you brought a new level of chaos but also joy to my life. You helped me understand the meaning of unconditional love in another way around. Your presence has filled every moment with warmth and happiness, fulfilling every aspiration I hold for this journey called life.

In the end, sincere gratitude is extended to all the reviewers who offered guidance and valuable suggestions during the paper review and defense.

# Curriculum Vitae

Zhen Wang was born on the 27<sup>th</sup> of April 1994 in Qingdao, China. After receiving her bachelor's degree in Electrical Engineering and Automation in 2016 at Shandong University, she stayed and pursued her master's degree in the same field for another 3 years. In 2019, she decided to continue doing research and enrolled at Xi'an Jiaotong University. After one year of study, she joined a double doctoral degree program between Eindhoven University of Technology, Department of Applied Physics, and Xi'an Jiaotong University, School of Electrical Engineering. For this project, she worked in the Multiscale Dynamics group at the CWI (Centrum Wiskunde & Informatica) from December 2020 to October 2023. For the rest of her PhD, she worked at Xi'an Jiaotong University, supervised by Anbang Sun.

## List of publications

1. Z. Wang, A. Sun, and J. Teunissen. A comparison of particle and fluid models for positive streamer discharges in air. *Plasma Sources Science and Technology*, 31(1):015012, 2022
2. Z. Wang, S. Dijcks, Y. Guo, M. Van Der Leegte, A. Sun, U. Ebert, S. Nijdam, and J. Teunissen. Quantitative modeling of streamer discharge branching in air. *Plasma Sources Science and Technology*, 32(8):085007, 2023
3. Z. Wang, A. Sun, S. Dujko, J. Teunissen, and U. Ebert. 3D Simulations of positive streamers in air in a strong external magnetic field. [arXiv:2305.00842 [physics.plasm-ph], May 2023]

4. Z. Wang, A. Sun, J. Teunissen. A model comparison of 2D Cartesian and 2D axisymmetric models for positive streamer discharges in air. [in preparation]